Ivane Javakhishvili Tbilisi State University

Faculty of Exact and Natural Sciences

Department of Physics

Tamar Zakareishvili

Study of the ATLAS Hadronic Calorimeter Response and J/ψ and $\psi(2S)$ Mesons Production Cross Section Measurement in pp Collisions at $\sqrt{s}$ = 13 TeV

The thesis work is performed to obtain a PhD academic degree in Physics

Scientific supervisors:

Dr. Tamar Djobava

High Energy Physics Institute of Tbilisi State University

Prof. Vakhtang Kartvelishvili

Lancaster University

Tbilisi

2022

ივ. ჯავახიშვილის სახელობის თბილისის სახელმწიფო უნივერსიტეტი

ზუსტ და საბუნებისმეტყველო მეცნიერებათა ფაკულტეტი

ფიზიკის დეპარტამენტი

თამარ ზაქარეიშვილი

ATLAS ექსპერიმენტის ადრონული კალორიმეტრის გამოძახილის შესწავლა და J/ψ და $\psi(2S)$ მეზონების დაბადების კვეთის გაზომვა პროტონ-პროტონული დაჯახებისას 13 ტევი მასათა ცენტრის ენერგიაზე

ფიზიკის დოქტორის აკადემიური ხარისხის

მოსაპოვებლად წარმოდგენილი დისერტაცია

სამეცნიერო ხელმძღვანელები:

თამარ ჯობავა

ფიზ-მათ. მეცნ. დოქტორი

თსუ მაღალი ენერგიების ფიზიკის ინსტიტუტი

ვახტანგ ქართველიშვილი

პროფესორი, ლანკასტერის უნივერსიტეტი

თბილისი

2022

This work is dedicated to my parents.
With your help I opened up my mind and heart to life and universe exploration.

ეს შრომა ეძღვნება ჩემს მშობლებს.
თქვენი დახმარებით გავუხსენი ცხოვრებას და სამყაროს შემეცნებას
გონების და გულის კარები.

Acknowledgements

The journey of my PhD has been an adventure! Remembering the day I started and thinking about reaching the finish line is definitely an emotional experience. I have grown in so many fields in my life during these years and I will forever be grateful for that to the people who have contributed to it.

First of all I want to mention that this work and this journey would have never started if not Irakli Minashvili, who has been the inspiration behind my goals, from the very beginning, and who later provided opportunities to pursue my goals, thank you for that!

I want to say big thank you to my supervisor Tamar Djobava, who has taught me many things, not just about physics, but about life too. I will carry all those precious things with me, for the rest of my life, thank you for that Tamar!

I want to say big thank you to my other supervisor Vato Kartvelishvili, who has been a huge support throughout this journey, thank you Vato, you have taught me how to enjoy the work I do and also to enjoy the mistakes I make!

I want to express my gratitude to all my friends who have been in my life throughout my journey, who have shown me a beautiful world that we live in. Mariam, your presence in my life is like having a second sun, thank you! Gogit, Bulis, Grigol, Mariam, Nika, Salome, Muku, Luka, Gvantsi, Khati, Tamta, Lali I am so lucky to have met you through physics! Ketusha you have been my family from the very beginning and my dear family - mother, father and sister has been the true beginning of it all, thank you for believing in me, always!

And finally I want to thank Fernando, I can not express how much you have helped me and how much I appreciate it all, thank you!

So many people have contributed to this journey, some I may not even realize have done so, some who I have not even met in my life, and some, who have made history but are not present in our lives any more. People make big imprints on us, and I am happy to carry with me the sweetest ones and I am happy to let go of the less pleasant ones.

Life is truly fascinating and I wish that we never lose perception and receptivity to it's beauty.

Works presented in this thesis were supported by: SRNSFG through the grant projects DI/20/6-200/14, FR17_184, DI_18-293; ISTC grant project G-2098; "Regional Doctoral Program in Theoretical and Experimental Particle Physics" scholarship of the SRNSFG Project 04/48 and Ref. 93 562 VolkswagenStiftung foundations.

Abstract

In this thesis are included the results obtained within ATLAS experiment physics program.

The first part is devoted to study of the ATLAS hadronic calorimeter response. The Large Hadron Collider (LHC) Phase–II upgrade aims to increase the accelerator instantaneous luminosity by a factor of 5-10. Due to the expected higher radiation levels, aging of the current electronics and the need to provide the capability of coping with longer latencies of up to $35\mu s$ by the trigger system at such high pile-up levels, a new readout system of the ATLAS Tile Calorimeter (TileCal) is needed. A prototype of the new Phase-II upgrade electronics, called ATLAS TileCal Demonstrator module has been tested using the particle beams from the Super Proton Synchrotron (SPS) accelerator at CERN. Data were collected in 2015–2018 and 2021–2022 with beams of muons, electrons and hadrons at various incident energies and impact angles. The muon data allow to study the dependence of the response on the incident point and angle through entire volume of the detector. The electron data are used to determine the linearity of the electromagnetic energy measurement. The hadron data allows to study the energy response and resolution of the detector and also to tune the modelling of the calorimeter response to pions and kaons with the purpose of improving the reconstruction of the energy of jets.

Using the test beam data, new electronics noise threshold was evaluated and afterwards layer response uniformity was studied using the muon data. The data recorded by Demonstrator show a layer response uniformity within 1%. An offset of max 1.4% is observed for Data/MC. Energy response uniformity is observed cell by cell within uncertainties.

Three spare modules of the ATLAS Tile Calorimeter were exposed to hadron beams. The energy response and resolution of the detector to positive pions and kaons and protons with energy in the range 16 to 30 GeV were measured. The results obtained using experimental and simulated data agree within the uncertainties.

In the second part of this thesis is described the study of the heavy quarkonium (J/ψ and ψ(2S)) production, using the ATLAS detector data. Studies involving heavy quarkonia provide a unique insight into the nature of Quantum Chromodynamics (QCD) near the boundary of

perturbative and non-perturbative regimes. However, despite the long history, the investigation of quarkonium production in hadronic collisions still presents significant challenges to both theory and experiment.

In high energy hadronic collisions, charmonium states can be produced either from the short-lived QCD sources (referred to as 'prompt' production), or from long-lived sources such as decays of beauty hadrons (referred to as 'non-prompt' production). These can be separated experimentally by measuring the distance between the production and decay vertices of the quarkonium state. Effects of feeddown from higher charmonium states contributes to production of J/ψ mesons, whereas no significant contribution occurs for the $\psi(2S)$ meson. While the theoretical calculations within the framework of perturbative QCD have been reasonably successful in describing the non-prompt contributions, a satisfactory understanding of the prompt production mechanisms is still to be achieved.

It is hence increasingly important to broaden the scope of comparison between theory and experiment by providing a broader variety of experimental information on quarkonium production in a wider kinematic range.

Double-differential production cross-section of J/ψ and $\psi(2S)$ charmonium states through their decays to dimuons in pp collisions at $\sqrt{s} = 13$ TeV was measured, using the data collected by the ATLAS detector at the LHC during Run 2. For each of the two states, the cross-sections are measured separately for prompt and non-prompt production mechanisms. The non-prompt fractions for each state are also measured, as well as the production ratios of $\psi(2S)$ to J/ψ. In case of J/ψ, the results cover the rapidity range $|y| < 2$ and the transverse momentum range between 8 GeV and 360 GeV. In case of $\psi(2S)$ the rapidity range is the same, but the transverse momentum range is between 8 GeV and 140 GeV. In both cases, the transverse momentum range goes well beyond the values reached so far, which may help discriminate various theoretical models.

The results show similar p_{T}-dependence for prompt and non-prompt differential cross sections. In low p_{T} region non-prompt fraction shows steep increase and in high p_{T} region the fraction is close to constant for both J/ψ and $\psi(2S)$. The results for non-prompt production are compared with the predictions of the theoretical model (FONLL) with default set of parameters. These predictions are consistent with the present measurement at the low end of the p_{T} range, but exceed the experimental values at large transverse momenta.

ანოტაცია

ამ ნაშრომში წარმოდგენილია ATLAS ექსპერიმენტის ფიზიკური პროგრამის ფარგლებში შესრულებული კვლევების შედეგები.

პირველ ნაწილში აღწერილია ATLAS ადრონული თაილ კალორიმეტრის გამოძახილის კვლევა და მისი შედეგები. დიდი ადრონული კოლაიდერის განახლების II ფაზისათვის იგეგმება ნათების 5-10 რიგით გაზრდა. ახალი წამკითხველი სისტემა - ელექტრონიკა არის საჭირო ATLAS ადრონული კალორიმეტრისათვის, რათა გაუძლოს მოსალოდნელ მაღალ რადიაციის დონეს და გაზრდილი ინფორმაციის რაოდენობას. ATLAS-ის ფაზა-2 განახლებისათვის შექმნილი ელექტრონიკის პროტოტიპი, სახელად დემონსტრატორი, გამოცდილი იქნა CERN-ის სუპერ პროტონული სინქროტრონიდან მიღებული ნაწილაკების ნაკადებით 2015–2018 წწ და 2021–2022 წწ-ში, ტესტური დასხივებისას, მიუონების, ელექტრონების და ადრონების ნაკადებით, რომლებიც მოდულს ეცემოდა სხვადასხვა დამცემი კუთხით. მიუონების მონაცემები საშუალებას იძლევა გამოკვლეული იქნას დეტექტორის გამოძახილი მისი მთლიანი მოცულობიდან. ელექტრონების მონაცემების მეშვეობით შესაძლებელია დეტექტორის გამოძახილის წრფივობის შესწავლა. ხოლო ადრონების მონაცემების გამოყენებით დეტექტორის გამოძახილის და გარჩევისუნარიანობის შეფასება და ATLAS-ის მოდელირების პარამეტრების გაუმჯობესება არის შესაძლებელი.

ტესტური დასხივებებისას ჩაწერილი მონაცემების მეშვეობით შეფასდა ახალი ელექტრონიკის ხმაური. დემონსტრატორის მიერ ჩაწერილი მიუონების მონაცემების ანალიზმა აჩვენა, რომ სატესტო მოდულის შრეების გამოძახილი ერთგვაროვანია 1%-ის ფარგლებში. ექსპერიმენტული და სიმულირებული მონაცემების შედეგებს შორის მაქსიმალური სხვაობა 1.4%-ის ტოლია. ენერგიის გამოძახილის ერთგვაროვნება იქნა დამზერილი უჯრედებს შორის, ცდომილების ფარგლებში. ასევე მიუონების მონაცემების გამოყენებით გადამოწმდა არსებული კალიბრაციის პროცედურა ადრონულ კალორიმეტრში. მიღებული შედეგები თანხვედრაშია ადრე ჩატარებულ კვლევებთან.

ასევე ATLAS თაილ კალორიმეტრის სამი მოდულის ადრონების ნაკადით დასხივების შედეგად გაიზომა დეტექტორის ენერგიის გამოძახილი და გარჩევისუნარიანობა დადებითი პიონების, კაონების და პროტონების მიმართ, 16-დან 30 გევი ენერგიის შუალედში. მიღებული ექსპერიმენტული შედეგები

შედარებული იქნა სიმულირებულ მონაცემების შედეგებს და თანადობაშია ცდომილების ფარგლებში.

ამ ნაშრომის მეორე ნაწილი შეეხება მძიმე კვარკონიუმის, J/ψ-ის და $\psi(2S)$-ის წარმოქმნის შესწავლას, ATLAS დეტექტორის მონაცემების გამოყენებით. კვარკონიუმის (მათ შორის ჩარმონიუმის) წარმოქმნის გამოკვლევა გვეხმარება უკეთ შევისწავლოთ კვანტური ქრომოდინამიკის ბუნება შეშფოთების და არა-შეშფითების რეჟიმების გარდამავალ არეში. ასევე მიუხედავად დიდი ისტორიისა, დღემდე კვარკონიუმის ადრონულ შეჯახებებში წარმოშობა წარმოადგენს გამოწვევას, როგორც თეორიისათვის, ასევე ექსპერიმენტისათვის.

მაღალ ენერგიებზე ადრონული შეჯახებებისას, ჩარმონიუმი შეიძლება წარმოქმნას პირდაპირი (პირველადი შეჯახებისას წარმოქმნილი) და არა-პირდაპირი (B ადრონის დაშლის შედეგად წარმოქმნილი) პროცესით. მათი განცალკევება ექსპერიმენტულად შესაძლებელია კვარკონიუმის წარმოქმნის და დაშლის წვეროს შორის მანძილის გაზომვით. კვანტური ქრომოდინამიკის ფარგლებში თეორიული გამოთვლები არა-პირდაპირი წარმოქმნის მექანიზმს კარგად აღწერს, თუმცა პირდაპირი წარმოქმნის მექანიზმის დამაკმაყოფილებელი ახსნა ჯერ კიდევ მოსაძებნია.

მნიშვნელოვანია კვარკონიუმის წარმოქმნის თეორიის წინასწარმეტყველებებისა და სხვადასხვა ექსპერიმენტზე მიღებული შედეგების შედარება კინემატიკის ფართო არეში.

გაზომილ იქნა J/ψ და $\psi(2S)$ მეზონების დაბადების დიფერენციალური კვეთა, საპირისპირო მუხტის მიუონებად დაშლის მოდაში, $\sqrt{s} = 13$ ტევი მასათა ცენტრის ენერგიაზე, როგორც პირდაპირი, ასევე არა-პირდაპირი დაბადების პროცესისათვის. გაზომილი იქნა არა-პირდაპირი ჩარმონიუმის დაბადების წილი J/ψ-სა და $\psi(2S)$-სათვის და ასევე $\psi(2S)$ ნაწილაკის წარმოქმნის კვეთის ფარდობა J/ψ ნაწილაკის წარმოქმნის კვეთასთან. გაზომვები J/ψ მეზონისათვის ჩატარებულია 8-დან 360 გევამდე განივი იმპულსის ინტერვალში, ხოლო $\psi(2S)$ მეზონისათვის 8-დან 140 გევამდე ინტერვალში, ანალიზში დაფარულია -2-დან $+2$-მდე სისწრაფის ინტერვალი. ორივე მეზონისათვის, განივი იმპულსის ინტერვალი ბევრად აღემატება ადრე ჩატარებული გაზომვების ინტერვალს და ამიტომ შესაძლებელია გამოსადეგი იყოს სხვადასხვა თეორიული მოდელის ერთმანეთისაგან გასარჩევად.

პირდაპირი და არა-პირდაპირი J/ψ და მეზონების დაბადების კვეთის p_{T}-ზე დამოკიდებულება ერთმანეთის მსგავსია. არა-პირდაპირი პროცესის წილი სწრაფად

იზრდება დაბალი განივი იმპულსის არეში და თითქმის მუდმივი ხდება მაღალი განივი იმპულსის არეში.

არა-პირდაპირი დაბადების პროცესის შესაბამისი შედეგების შედარებით თეორიული მოდელის (FONLL) წინასწარმეტყველებებთან, შეიძლება ითქვას რომ დაბალი p_{T}-ს არეში ეს წინასწარმეტყველებები თანხვედრაშია ექსპერიმენტზე გაზომილ (ამ ნაშრომში წარმოდგენილ) შედეგებთან, ხოლო მაღალი p_{T}-ს არეში ექსპერიმენტულ შედეგებზე მეტია.

Contents

Chapter 1

Theoretical overview

1.1 Quarkonium physics

Since the discovery of the J/ψ in 1974, heavy quarkonium has been on the focus of much experimental and theoretical attention. Heavy quarkonium is a bound state consisting of a heavy quark (Q) and its anti-quark ($\bar{Q}$). Depending on the flavor of the quark pair, there are charmonium and bottomonium. The production of a heavy quarkonium involves three different momentum scales: the heavy quark mass m_Q, which governs the perturbative creation of the heavy quark pair ($Q\bar{Q}$); the heavy quark momentum $m_Q v$ in the quarkonium rest frame; and the typical heavy quark kinetic energy $m_Q v^2$, which governs the nonperturbative hadronization of the $Q\bar{Q}$ to physical quarkonium. Here v is the typical heavy quark velocity in the quarkonium rest frame ($v^2 \approx 0.3$ for charmonium and $v^2 \approx 0.1$ for bottomonium). Due to the non-relativistic nature of the bound state, heavy quarkonium production at high energy collisions is a very important process to test our understanding of QCD (Chen, Ma, & Zhang, 2021).

The quarkonium states are characterized according to the quark–antiquark system's total spin - S, the orbital angular momentum - L, and the system's total angular momentum - J ($\vec{J} = \vec{L} + \vec{S}$). The charge conjugation symmetry - C, is given by $C = (-1)^{L+S}$, and the parity - P, of the quark–antiquark system is given by $P = (-1)^{L+1}$. Parity and charge conjugation are both conserved quantities in the strong and electromagnetic decays of the quarkonium states. The spectroscopic notation $n^{2S+1}L_J$ is often used to denote the quarkonium states, where n is the principal quantum number. In Figure 1.1 the spectrum of $c\bar{c}$ states is shown.

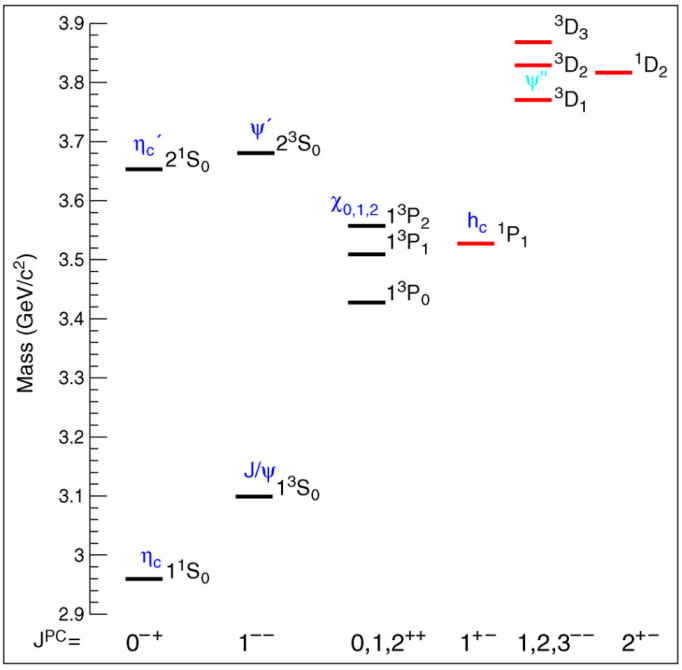

Figure 1.1: The mass spectrum of charmonium states with various quantum numbers of J^{PC} (Bettoni & Calabrese, 2005).

1.2 Heavy quarkonium production mechanism

Heavy quarkonium production is usually separated into two steps: (1) the production of a $Q\bar{Q}$ pair with definite spin and color state in a hard collision, which could be calculated perturbatively; and (2) hadronization of the $Q\bar{Q}$ pair into a physical heavy quarkonium at a momentum scale much less than the heavy quark mass m_Q, which is in principle nonperturbative. Different treatments of the nonperturbative transition from a $Q\bar{Q}$ pair to the physical quarkonium lead to different theoretical models. In the following, we briefly describe some of the most widely-used ones: the color evaporation model (CEM), the color singlet model (CSM) and the non-relativistic QCD (NRQCD) factorization theory.

The Color Evaporation Model (CEM) (Einhorn & Ellis, 1975; Barger, Keung, & Phillips, 1980) is a relatively simple model, in which there is no correlation of color and angular momentum quantum numbers between the initial $Q\bar{Q}$ state and the final quarkonium state. It is assumed that soft gluon emission during the binding process alters the quantum numbers to arrive at the appropriate final state.

The Color Singlet Model (CSM) (Fritzsch, 1977; Chang, 1980) takes the opposite approach, assuming that each quarkonium state can only be produced by a $Q\bar{Q}$ pair in the same color and

angular momentum state as that quarkonium. Therefore, a J/ψ meson, for example, can only be derived from a $c\bar{c}$ pair created in a 1^3S_1 color-singlet state.

The third and more "sophisticated" theoretical approach to quarkonium production is known as the Nonrelativistic QCD (NRQCD) factorization formalism (Bodwin, Braaten, & Lepage, 1995a). Sometimes the phrase "Color Octet Model" (COM) is encountered when color-octet mechanisms are considered. However, the COM lacks the formal organization of energy scales that NRQCD provides. NRQCD is an effective field theory, which treats quarkonium as an approximately nonrelativistic system. NRQCD makes systematic corrections to this approximation using an expansion series in v the velocity of the heavy quark in the quarkonium rest frame.When applied to production, this implies that $Q\bar{Q}$ pairs produced with one set of quantum numbers can evolve into a quarkonium state with different quantum numbers, by emitting soft gluons.

Quarkonium production was originally described in CSM model. This approach had the benefit that all non-perturbative aspects could be absorbed into the wave function of the quarkonium state. This model enjoyed some success before CDF (Collider Detector at Fermilab) measured an excess of direct J/ψ production (Abe et al., 1992) more than an order of magnitude greater than that predicted by the CSM (see Figure 1.2).

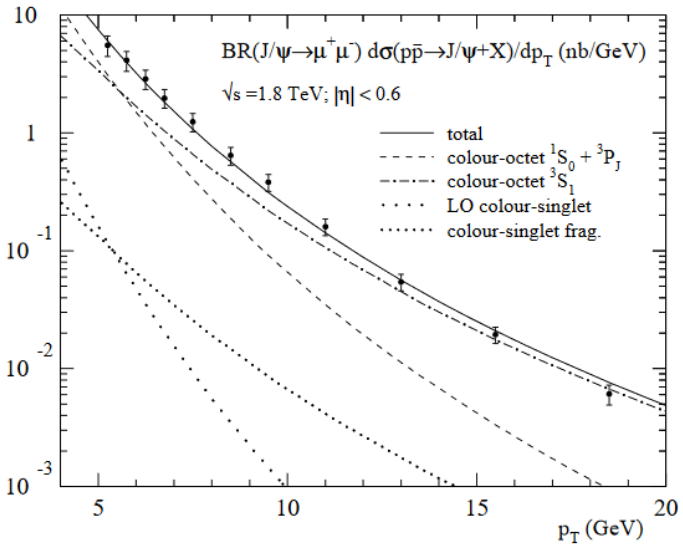

Figure 1.2: Differential cross-section of J/ψ production at CDF with theoretical predictions for color-singlet and color-octet model production (Krämer, 2001).

The Color Octet Model (COM) (Cho & Leibovich, 1996) was proposed as a solution to the theory prediction mismatching. COM provides a solution to the infrared divergences that were

present in the production cross-sections of P-wave states in CSM, by incorporating the description of the problematical soft gluon emission into the nonperturbative color-octet parameter.

Chapter 2

ATLAS experiment

2.1 CERN

After the second World War, a handful of scientists encouraged by the increasing number of international organizations, proposed the creation of a european laboratory for nuclear physics allowing them to share the cost of the facilities. A provisional body was founded in 1952 under the name in french Conseil Europeen pour la Recherche Nucleaire or CERN. The acronym was kept after the foundation of the current European Organization for Nuclear Research, the 29th of September of 1954, in the Swiss canton of Geneva, across the French-Swiss border. CERN is run by 23 European Member States, but many non-European countries are also involved in different ways. Scientists come from around the world to use CERN's facilities.

2.2 Large Hadron Collider - LHC

The Large Hadron Collider (LHC) - the world's largest and most powerful particle accelerator, is the latest addition to CERN's accelerator complex (Figure 2.1). Two accelerated particle beams collide heads on with each other, with no energy wasted from the recoil of a stationary target. The LHC was built in the tunnel where the Large Electron Positron collider (LEP) operated from 1989 to the end of 2000. This tunnel has a circumference of 27 km and crosses the border of Switzerland and France. Before being injected with an energy of 450 GeV into the LHC's 27 km ring, protons are accelerated and formed in beams in four increasingly large machines.

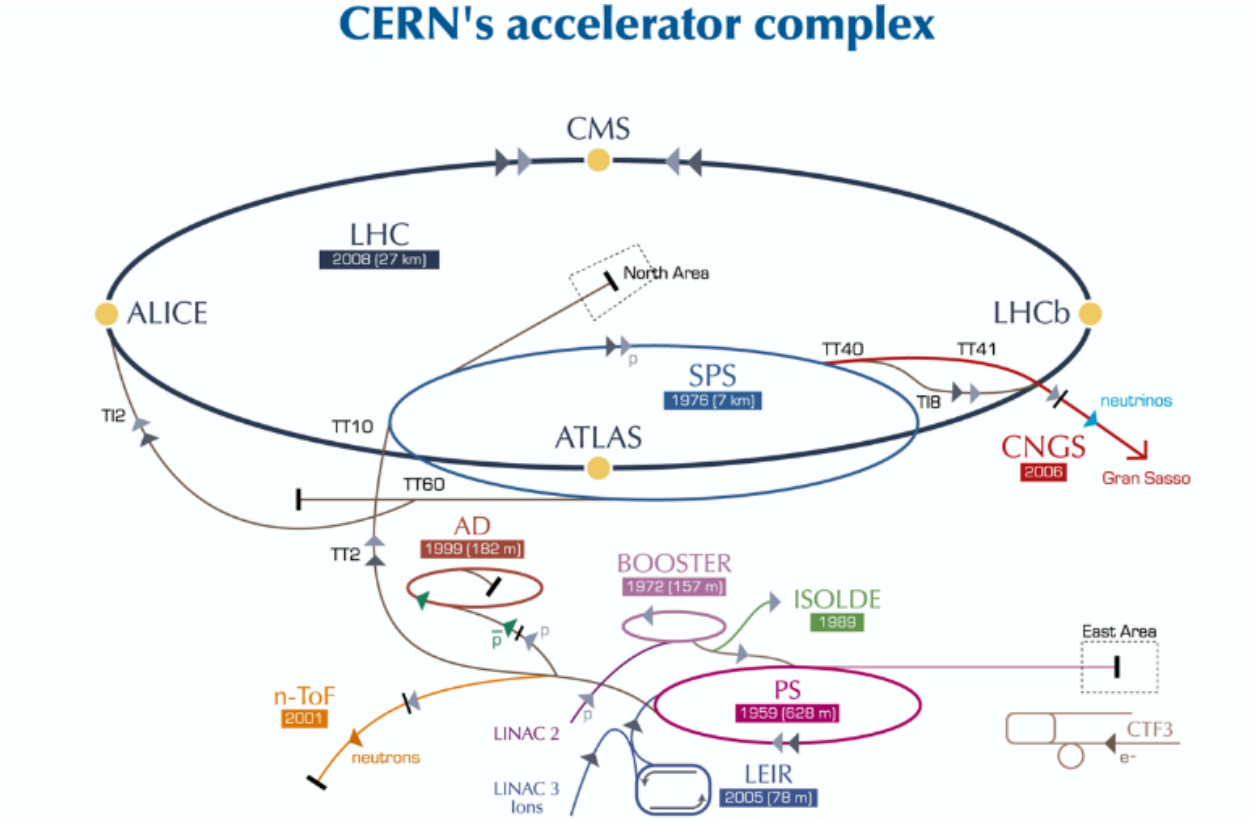

Figure 2.1: Operational CERN accelerators.

The beams are then accelerated in the ring until their energy is increased by a factor of 15, to 7000 GeV. When that energy is reached, the proton beams collide in the center of the experiments. The LHC collides beams of protons at a center of mass energy of 13 TeV and a design luminosity of 10^{34} cm^{-2} s^{-1}. In order to achieve this energy, the beams of particles travel at close to the speed of light in opposite directions in separate beam pipes kept at ultrahigh vacuum. They are guided around the accelerator ring by a strong magnetic field, achieved using superconducting electromagnets. These are built from coils of Nb-Ti that operate in a superconducting state, efficiently conducting electricity without resistance or loss of energy. This requires to cool down the magnets to about 2 K (-271°) with superfluid helium at 1.9 K and allows an operational field of 8.4 Tesla. In total, 1232 dipole magnets of 14.2 m length are used to bend the beams, and 392 quadrupole magnets, each 5 to 7 m long, to focus the beams.

The LHC's research run took place from March 2010 to early 2013 at an energy of 3.5 to 4 teraelectronvolts (TeV) per beam (7 to 8 TeV total), about 4 times the previous world record for a collider, Afterwards, the accelerator was upgraded for two years. It was restarted in early 2015 for its second research run, reaching 6.5 TeV per beam (13 TeV total, the current world

record).

2.3 ATLAS experiment

The ATLAS experiment (ATLAS Collaboration, 2008) at the CERN Large Hadron Collider (LHC) is designed to exploit fully the exciting opportunities for fundamental discoveries at the next high-energy frontier (Figure 2.2).

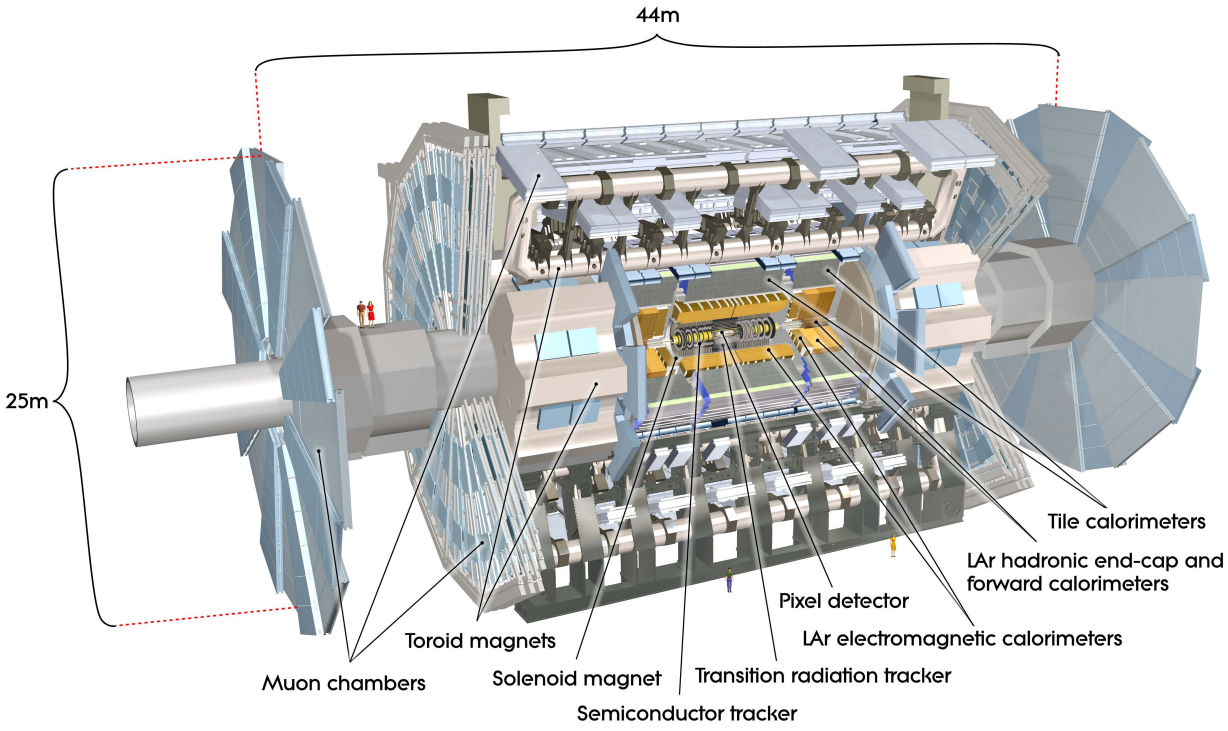

Figure 2.2: ATLAS detector.

ATLAS is about 45 meters long, more than 25 meters high and has an overall weight of approximately 7000 tonnes. It is divided into sub-detectors as show in Figure 1.3. The Inner Detector represents the inner most part of ATLAS, surrounded by a solenoid magnet, the Calorimeters, the Muon system and a very large air-core toroid magnet. It is designed to work at high luminosity ($10^{34}\text{cm}^{-2}\text{s}^{-1}$) with a bunch crossing every 25 ns. The Inner Detector is designed to reconstruct tracks and decay vertices in any event with high efficiency. Using additional information from the calorimeter and muon systems, the inner detector also contributes to electron, photon, and muon identification, and supplies extra signatures for short-lived particle decay vertices. The Muon Spectrometer is an extremely large tracking system, consisting of three parts: (1) a magnetic field provided by three toroidal magnets, (2) a set of 1200 chambers

measuring with high spatial precision the tracks of the outgoing muons, (3) a set of triggering chambers with accurate time-resolution. The extent of this sub-detector starts at a radius of 4.25 m close to the calorimeters out to the full radius of the detector (11 m). Its tremendous size is required to accurately measure the momentum of muons, which first go through all the other elements of the detector before reaching the muon spectrometer. The ATLAS detector uses two large superconducting magnet systems to bend charged particles so that their momenta can be measured. This bending is due to the Lorentz force, which is proportional to velocity. Since all particles produced in the LHC's proton collisions are traveling at very close to the speed of light, the force on particles of different momenta is equal. (In the theory of relativity, momentum is not linear proportional to velocity at such speeds.) Thus high-momentum particles curve very little, while low-momentum particles curve significantly; the amount of curvature can be quantified and the particle momentum can be determined from this value. Electromagnetic and hadronic calorimeters are indispensable components of a general-purpose hadron collider detector. Jointly they must provide accurate energy and position measurements of electrons, photons, isolated hadrons, jets, and transverse missing energy, as well as helping in particle identification and in muon momentum reconstruction. The electromagnetic (EM) and hadronic compartments of the ATLAS calorimeter system cover the pseudorapidity region $|\eta| < 4.9$. The EM compartments are liquid argon sampling calorimeters, while the detector media of the hadronic calorimeters differ according to the $|\eta|$ (pseudorapidity) region. The Tile Calorimeter (TileCal) is a sampling detector with scintillating plastic tiles as active material and iron as absorber, located in the region $|\eta| < 1.7$.

2.4 ATLAS Tile Calorimeter

The Tile calorimeter is a hadronic calorimeter in the central region of the ATLAS detector in the Large Hadron Collider experiment (Figure 2.3). TileCal is divided into three cylindrical sections, referred to as the long barrel (LB) and two extended barrels (EB). 6-meter-long central barrel (LB) is covering rapidity range $|\eta| < 1.0$ and two 3-meter-long extended barrel (EB) detectors covering $0.8 < |\eta| < 1.7$. Each of the three TileCal barrels is composed of 64 azimuthal segments, referred to as modules. The TileCal scintillator plates are placed perpendicular to the colliding beam axis, and are radially staggered in depth. The structure is periodic along the beam axis. The tiles are 3 mm thick and the ratio of iron to scintillator is 4.7 to 1, allowing for

a good sampling frequency and a compact calorimeter with and effective nuclear interaction length $\lambda = 20.7$cm. Two sides of the scintillating tiles are read out by wave-length shifting (WLS) fibers into two separate photomultipliers (PMTs). The PMT's and part of the front end electronics are located on the outer side of the modules (Figure 2.3). The central barrel modules are divided in up to 45 cells each, while the extended barrels modules are divided in 14 cells. Therefore, TileCal is comprised of more than 10000 readout channels.

The existing TileCal inside ATLAS is designed to operate at 13TeV center-of-mass (COM) energy and of luminosity $10^{34}\text{cm}^{-2}\text{s}^{-1}$. However, the LHC Phase–II Upgrade (High Luminosity LHC, HL-LHC) (Apollinari et al., 2017) aims to increase the LHC luminosity by a factor of 5–10 (5–10 $\times 10^{34}\text{cm}^{-2}\text{s}^{-1}$). The HL-LHC environment presents several challenges for TileCal. The current electronics is ageing and will be submitted to higher radiation levels, so new electronics are needed to guarantee reliability and reduce maintenance costs. To date, has been built a Demonstrator - a fully functional prototype of the new electronics system (Spoor & Mellado Garcia, 2015). The Demonstrator is a hybrid module equipped with the upgraded electronics that was installed into the ATLAS experiment for the evaluation of the new readout architecture for the ATLAS Phase-II Upgrade.

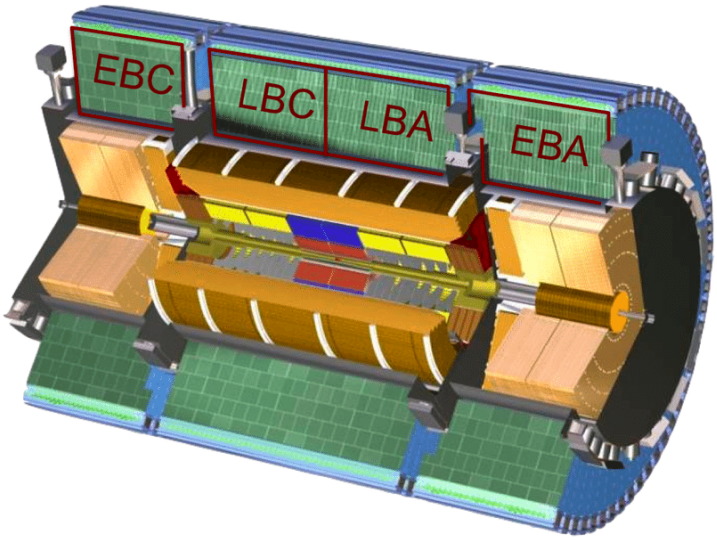

Figure 2.3: ATLAS Tile calorimeter.

The high-energy muons traverse the entire TileCal modules for any angle of incidence, thereby allowing a study of the production module response in great detail through their entire volume, which also gives us possiblivity to evaluate performance of the new electronics

designed for HL-LHC (A. Solodkov, 2017).

The defining role of hadron calorimetry is to measure the energies of jets. For this purpose, its performance for isolated hadrons is a necessary starting point and is the subject of this study.

Tile calorimeter is a sampling calorimeter which has iron as passive medium and plastic scintillator tile as an active medium (Figure 2.4). The iron plates are needed to stop the particle and scintillator tile produces the light which is further transmitted to the photomultiplier tube via wavelength-shifting fiber. In each module of the TileCal a three-dimensional cell structure is defined by grouping optical fibres connected to the same PMT. In general two PMTs read-out a cell and the signals are summed up to provide the cell response. In a PMT the light is converted to the electronic signal and it is processed by the 3-in-1 card (Front-End-Board), see Figure 2.5. 3-in-1 card is responsible for signal conditioning and amplification, provides three analog signals as outputs, two for the detector readout (high and low gain) and another for triggering purpose. The low and high gain signals are then digitized at 40 MHz by 10-bit Analog to Digital Converters (ADCs) in the Digitizer Boards. Digital signals of all calorimeter cells in a given module are merged and formatted into packages and sent via high speed optical links (Interface Board) that connects the on- and off- detector electronics. The on-detector electronics is located in the outermost part of the TileCal module, which is known as “drawer”. Long barrel consists of two drawers, referred to as “Super Drawer”, and extended barrel consist of one drawer.

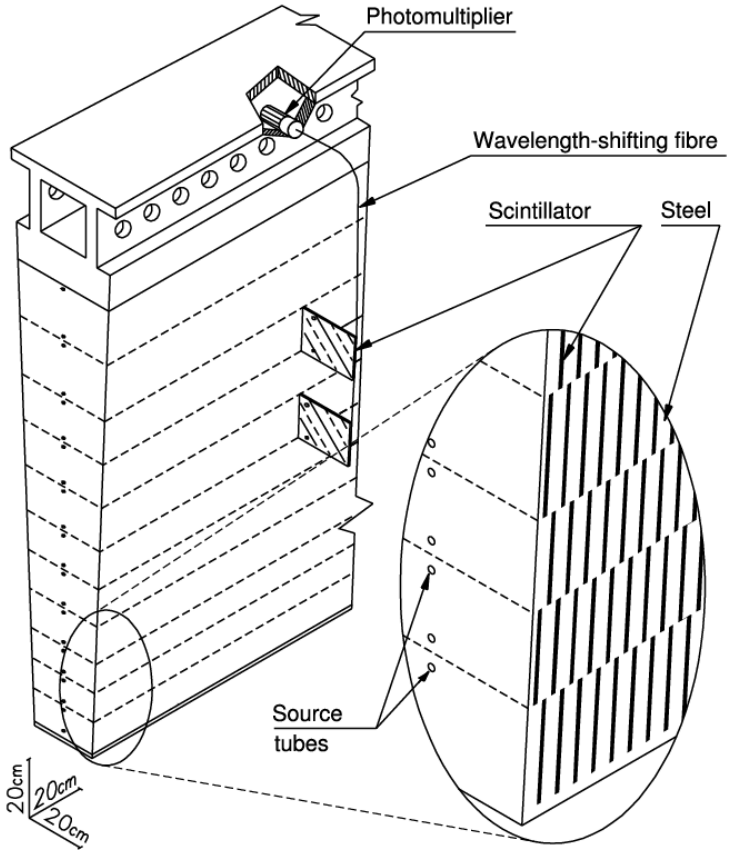

Figure 2.4: Mechanical structure of a TileCal module, showing the slots in the steel for scintillating tiles and the method of light collection by wavelength-shifting fibres to PMTs. The holes for radioactive source tubes that traverse the module perpendicularly to the iron plates and scintillating tiles are also shown.

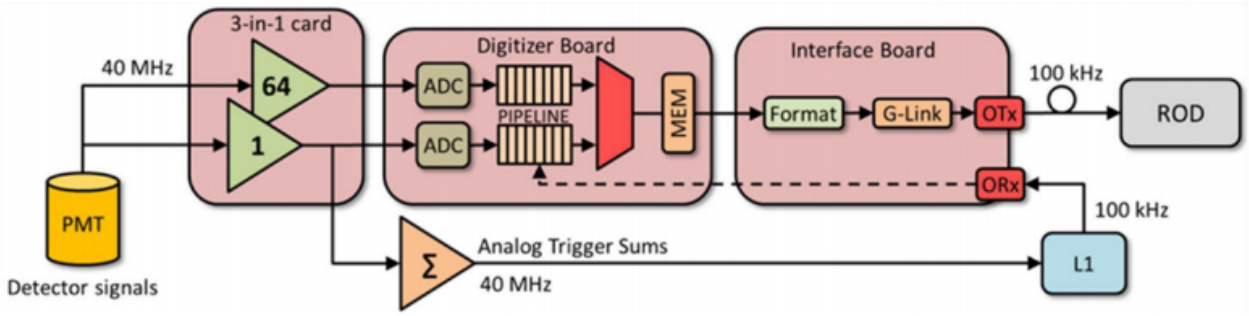

Figure 2.5: TileCal signal flow in the current system (Legacy SD).

In the back-end electronics, the main component is the Read-Out Driver (ROD) which performs signal preprocessing and gathers data coming from the front-end electronics at the maximum level 1 trigger rate of 100 KHz. The ROD sends these data to the Read-Out Buffers

(ROB) in the second level trigger.

TileCal has four different partitions Long Barrel (LB), Extended Barrel (EB) in A and C sides. Each of this partition is constructed with 64 modules, each of them has 48 channels connected at different layer (compartment) of the module.

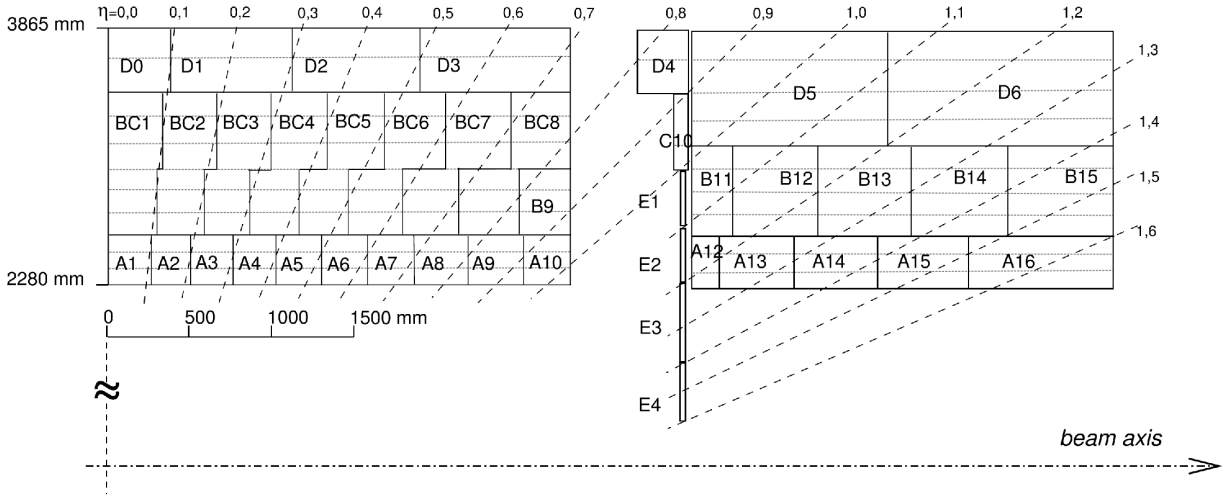

Figure 2.6: ATLAS Tile Calorimeter module geometry. Solid lines show the cell boundaries formed by grouping optical fibers from the tiles for read-out by separate photomultipliers. Horizontal dashed lines show tile-row structure of the modules.

A schematic diagram of Tile Calorimeter geometry is given in Figure 2.6. Each module of the LB and EB have 11 tile-rows. First three Tile-rows are inside A layer, from 4th-9th tile-rows are in BC layer and last two rows are in D layer.

2.5 Phase-II Upgrade

The LHC Phase–II Upgrade aims to increase the LHC luminosity by a factor of 5–10 (5–10 $\times 10^{34}\text{cm}^{-2}\text{s}^{-1}$). The HL-LHC environment presents several challenges for TileCal (O. Solovyanov, 2017). The current electronics is ageing and will be submitted to higher radiation levels, so new electronics are needed to guarantee reliability and reduce maintenance costs. The current analog trigger system will be replaced by a fully digital Level-1 trigger system. To date, has been built a Demonstrator - a fully functional prototype of the new system. The Demonstrator is a hybrid prototype associated to one TileCal module and is integrated into ATLAS for evaluation of the LHC Phase–II upgrade new electronics architecture. The Demonstrator electronics has a hybrid of analog and digital triggering, in order to make it compatible with the present analog trigger scheme.

Along with the development of new electronics a modification of the TileCal mechanics is being considered. In the new readout electronics current drawers are split into two "mini-drawers". This is compatible with the new electronics architecture. The new mechanics will improve the access to the on-detector electronics, making easier the maintenance and replacement of the mini-drawers.

The new readout electronics is composed of: Front-End Boards (FEB) that provide conditioning for the PMT signals as well amplification, digitization and calibration functionalities; new Main Boards (MB) providing digitization and control; and Daughter Boards (DB) which provide data processing and interface with the back-end electronics via optical links at up to 40 MHz rate with redundancy. The star power distribution along with local point-of-load voltage regulators in the new on-detector electronics reduces the voltage deviations and the noise coupling along the drawer. Another important change on the on-detector electronics architecture is the replacement of the current Interface Board by four Daughter Boards, improving the system robustness and decoupling the drawer electronics into four independent units.

The signal flow for the Phase–II system is shown in Figure 2.7. These signals are fully digitized and transmitted off-detector via high-bandwidth optical links to the Tile Preprocessor

(TilePPr) (F. Carrió and A. Valero, 2020). With this approach the maximal information is available for the trigger and the signals are much less vulnerable to electronic noise. The TilePPr sends reconstructed energy per cell to the Trigger and Data AcQuisition interface (TDAQi), which creates the trigger objects and sends them to the ATLAS trigger system. The TilePPr also receives and transmits slow control information to the drawer, and distributes the accelerator clock to the on-detector electronics for the synchronization with the rest of the ATLAS data acquisition system.

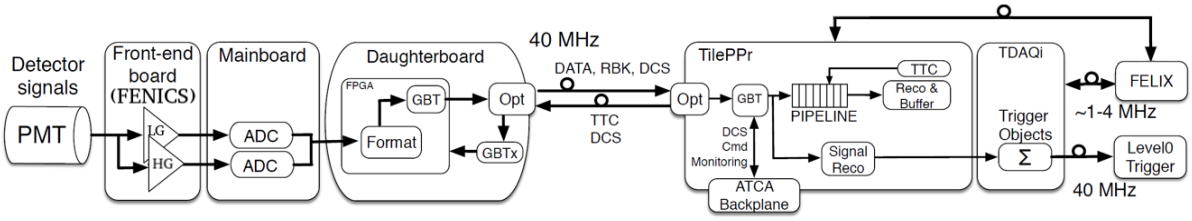

Figure 2.7: Signal flow in the Phase–II system.

The upgraded 3-in-1 FEBs has been mounted in the Demonstrator which provides the upgrade functionalities compared to previous electronics (Legacy SD), such as:

- Improved radiation tolerance, noise performance and linearity;
- Improved Signal to Noise Ratio (SNR).

As part of the R&D there were another two options in development, based on ASICs (An Application Specific Integrated Circuit):

- QIE (J. Hoff, 1999) - the "Charge Integrator and Encoder" ASIC (QIE) is a front-end board which includes a new version of the Charge (Q) Integrator and Encoder (QIE) chip and does not perform pulse shaping, minimizing pile up problems and allowing raw PMT pulses to be measured. For a more detailed description and status see ref. (G. Drake, 2015).
- FATALIC (N. Pillet, 2011) - the "All in One" front-end is based on the Front-end for Atlas TileCal Integrated Circuit (FATALIC) ASIC includes a multi-gain current conveyor (CC) with three different gains (1, 8, 64) which cover the full dynamic range of the PMT signal, followed by a shaper in order to improve the SNR. For a more detailed description and status see ref. (L. Royer, 2015).

2.6 Testbeam setup

In the North Area of CERN, particle beams are produced by a high-intensity primary 400 GeV protons, coming from Super Proton Synchrotron (SPS) accelerator, impinging on each of the three primary targets T2, T4 or T6 (Figure 2.8). Secondary particles are picked up by the beam lines H2, H4, H6, H8, P42, K12, M2, and are transported to the user areas. These beam lines are long (from about 500 to almost 1200 meters) and complex and contain a large number of elements of different natures, such as targets, magnets, collimators, dumps, absorbers, converters, detectors, vacuum pumps and access doors.

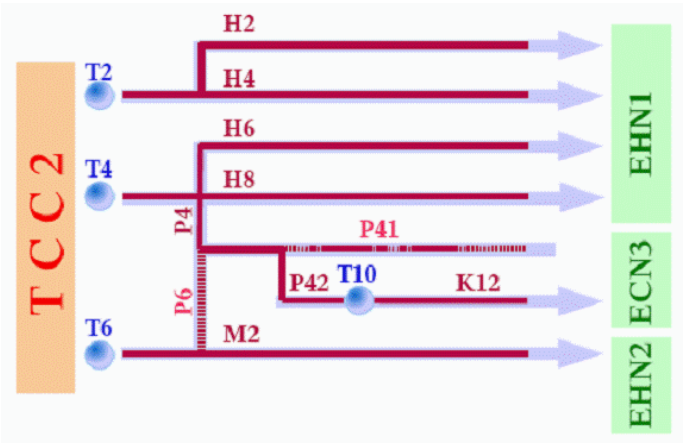

Figure 2.8: Synoptical diagram of the CERN North Area beam lines.

The hadron beam is produced using tertiary particle beams at the H8 line (Figure 2.8). Secondary beams are produced by targeting protons on a beryllium target (primary target). Using Secondary Targets located downstream, tertiary beams can be produced. To have mixed hadron enriched beams, the Secondary Target is made of copper. Additionally, a lead absorber is moved into the beam downstream of the target. It absorbs the electrons, while the hadrons mostly pass through it. For electron enriched beams, the Secondary Target is made by aluminum. It is immediately followed by lead. The lead absorber further downstream is moved out of the beam trajectory. A large spectrometer constructed of four Main Bend North Area dipole magnets is used for the momentum definition. Beam particles can have energies from 10 to 350 GeV. Beam intensity decreases dramatically at low energies.

Muons are produced by the decay of pions, therefore muon beams are produced by setting up a moderately high-intensity pion beam. The muons from their decay will partly reach the experiment. The remaining pions must be stopped, either in a beam dump or in a collimator.

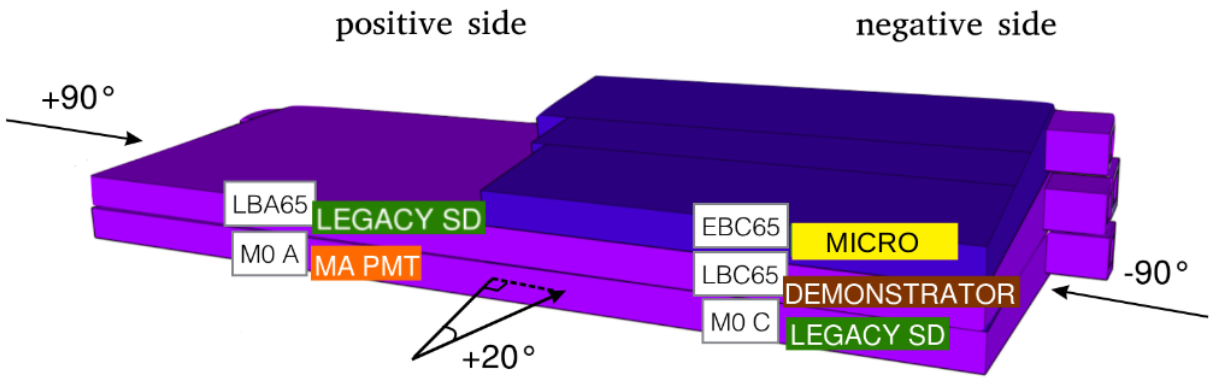

Figure 2.9: October - November 2018 testbeam setup

The Tile Calorimeter test beam (TB) setup in the H8 beam of the CERN SPS North Area, shown in Figure 2.9, consists of three spare ATLAS modules of TileCal, two long-barrels and one extended-barrel, stacked on a scanning table (see Figure 2.10) that is capable of placing modules at different position and angle with respect to the incoming beam particles. In the Figure 2.9 they are named M0A and M0C (module at the bottom), LBA65 and LBC65 (module in the middle) and EBC65 (module at the top). Some of the super-drawers were equipped with different upgraded front-end electronics systems proposed for the ATLAS LHC Phase-II operations (ATLAS Collaboration, 2017). The super-drawer of the long barrel LBC65 was equipped with the 3-in-1 front-end upgrade option, the so-called Demonstrator, which provides all the upgrade functionalities compared to previous electronics (Legacy SD). The super-drawers EBC65 and M0C were equipped with the electronics installed at the present in ATLAS (Legacy SD), and analog trigger outputs to keep backward compatibility with the current trigger system.

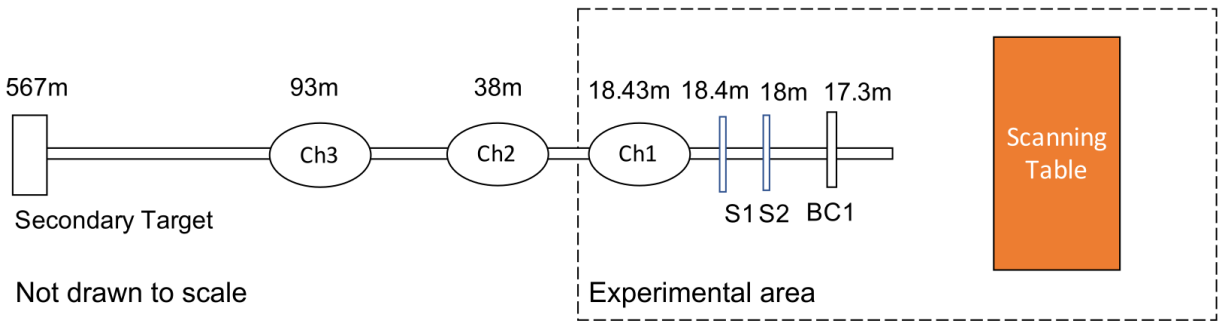

Figure 2.10: Schematic layout of the H8 beam line detectors.

Until the particle beam reaches testing modules of TileCal, it goes through the beam line detectors shown in Figure 2.10.

The transverse beam profile was monitored by the wire chamber BC1. Two scintillating counters, S1 and S2 with an active surface of 5×5 cm^2 (Di Girolamo et al., 2005), were used in coincidence to trigger the data acquisition (Physics Trigger) and to provide the trigger timing. These two detectors were also used to reject beam particles interacting upstream of the detector. The Cherenkov counters Ch1, Ch2 and Ch3 allowed identification of beam particles.

Data were collected with beams incident at the centre of the front face of each A-cell at $\theta = 14/20^\circ$ from the normal and incident on the ends of the module, referred to as $\pm 90^\circ$ incidence angle, on TB campaigns held during 2015–2018 and 2021–2022.

2.7 Tile Calorimeter readout

The Tile Calorimeter is required to measure particle energies in a dynamic range corresponding to 16 bits, extending from typical muon energy deposition of a few hundreds of MeV to the highest energetic jet of particles. A scheme with a double readout using two independent 10-bit ADCs was chosen to cover this range. The PMT pulse is shaped, then fanned-out and amplified in two separate branches with a nominal gain ratio of 64. The two output pulses, referred to as high gain and low gain, have a fixed width (FWHM) of about 50 ns and an amplitude that is proportional to the energy deposited in the cell. The two pulses are digitized simultaneously by two 10-bit ADCs at 40 Msps; the time series (samples) for each pulse is stored in the Data Management Unit that also performs some first processing. Each pulse is sampled seven times in physics mode, up to nine samples may be recorded for calibration purposes. The high gain ADC is normally used unless the time series contain measurements which saturate the ADC. In this case the low gain ADC readout is used. The samples are kept in digital pipelines on the detector, and if the event is accepted by the Level-1 Trigger system, are sent to the back-end electronics.

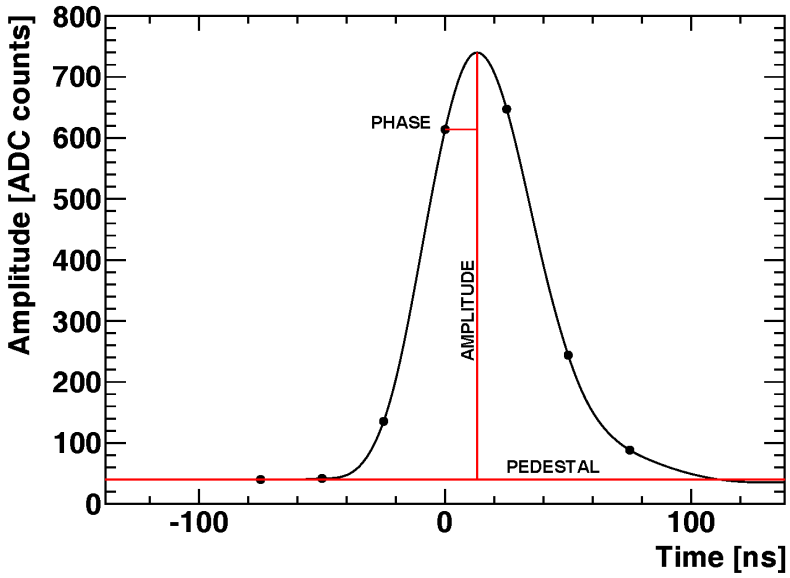

Figure 2.11: Normalized pulse shape of Physics data.

Figure 2.11 shows an analog signal pulse and the ADC measurement samples, and illustrates the main characteristics of the pulse: amplitude (energy), arrival phase (timing) and baseline level, or pedestal (noise). The LHC is a synchrotron, the phase of the calorimeter signals of interaction events is expected to be synchronized with the LHC clock and constant within very small fluctuations. The residual fluctuations are mainly due to the longitudinal spread of proton bunches. The ADC measurement phase can be adjusted to compensate for delays and particle time of flight.

Three different energy reconstruction methods have been developed and tested. The simplest and fastest of them, the Flat Filter (FF) method, has been used for the online event analysis. The more sophisticated Fit and Optimal Filtering (OF) methods profit from knowledge of the pulse shape and provide better resolution, especially in the energy region where noise plays an important role.

2.7.1 Fit Reconstruction Method

Fit method (Adragna et al., 2009) of signal reconstruction takes advantage of the knowledge of the pulse shape from the front-end electronics, which is proportional to the energy deposited by the particle in the Tile calorimeter cell. This pulse is digitized by 7 samples which are spaced by 25 ns as shown in Figure 2.11.

From the energy deposition in the scintillator tile we get the 7 samples S_{i}, where i = 1 to

7. The value of the sample can be expressed by,

$$S_{\mathrm{i}} = Ag(t_{\mathrm{i}} - t) + ped \tag{2.1}$$

Here A is the amplitude of the signal, t_{i} is the time where the sample i was obtained, the ped is the pedestal value, t is the time of the peak of the pulse and g is a normilised pulse shape.

In Fit method, we use a known pulse shape which reduces the background due to the electronic noise. The timing of the energy deposition can also be determined by this method and it depends on the fit parameter explained in Equation 2.1, amplitude, time and pedestal. To get the best fit result the following expression needs to be minimized:

$$\chi^2 = \sum_{i=1}^{n} \left(\frac{S_{\mathrm{i}} - [Ag(t_{\mathrm{i}}) - Atg^{'}(t_{\mathrm{i}}) + ped]}{\sigma_{\mathrm{i}}} \right)^2 \tag{2.2}$$

σ_{i} is the error (standard deviation) of the sample i.

2.7.2 Optimal Filtering Reconstruction Method

The other reconstruction method that is being used for the real collision data is the Optimal Filtering method (OF) (Adragna et al., 2009; G. Usai, 2010). Instead of fitting a known pulse shape, amplitude of a given pulse is calculated using the linear combination of the sample S_{i}. The coefficients of the linear combination are the OF weights. The method also reconstructs the time and allows to estimate the quality of the reconstruction:

$$A = \sum_{i=1}^{n} a_{\mathrm{i}} S_{\mathrm{i}} \tag{2.3}$$

$$A\tau = \sum_{i=1}^{n} b_{\mathrm{i}} S_{\mathrm{i}} \tag{2.4}$$

$$QF = \sum_{i=1}^{n} |S_{\mathrm{i}} - Ag_{\mathrm{i}}| \tag{2.5}$$

where N stands for the number of samples, A is the amplitude of the signal, τ represents the phase with respect to the expected sampling time (within the 5th sample). QF is the quality factor of the reconstruction. The parameters a_i, b_i are the OF weights for the amplitude and time reconstruction, respectively. The values g_i are the amplitudes of the normalized shape function for the i-th sample and the S_i are the digital samples. The weights are calculated to reconstruct the proper magnitudes while minimizing the noise, using the Lagrange multiplier

method. Both methods are iterative methods, i.e. multiple iterations are done to find correct position of the peak. But when value of maximum sample minus first sample (pedestal/ noise) $S_{\text{max}} - S_1$ is less than threshold value no iterations are done in both methods and phase equal to zero is assumed.

2.8 Calibration procedure in Tile Calorimeter

Signal calibration procedure in Tile Calorimeter (M. Marjanovic, 2019) is described by the equation:

$$E_{channel}[GeV] = A_{channel}[ADC] \cdot C_{ADC \to pC} \cdot C_{pC \to GeV} \cdot C_{Cs} \cdot C_{las} \cdot C_{\mu}, \tag{2.6}$$

where:

- $A_{channel}[ADC]$ is a signal amplitude obtained using the Optimal filter reconstruction method.
- $C_{ADC} \to$ pC - Charge injection system (CIS) : Charges in pico Coulomb of known values are injected into read-out electronics. The CIS constant gives the relation between the value of a charge and the signal amplitude.
- $1/C_{pC \to GeV}$ - Conversion factor (ElectroMagnetic - EM scale calibration constant) between the measured charge in pC and the energy of the incident electron.
- C_{Cs} - Cesium system (Cs): 137 Cs γ – source embedded in a capsule, moves with a constant speed inside the stainless steel tubes through all the calorimeter volume exciting all the scintillating tiles. It is the main tool to equalize the calorimeter cells responses.
- C_{las}- Laser system: Sends laser pulses of known intensities into the photocathodes of PMTs. It's aim is to monitor the response of PMTs and provide additional calibration factor.
- C_{μ} – Correction of the EM scale, due to the different sizes of the cells and the position of the Cs stainless steel tubes.

Chapter 3

Response of Demonstrator to muons

The interaction of muons with matter is well understood (A.K Olive, 2006). The dominant energy loss process is ionization and the energy loss is essentially proportional to the muon track path length. The high-energy muons available at the H8 beam line traverse the entire TileCal modules for any angle of incidence, thereby allowing a study of the production module response in great detail through their entire volume.

The most important application of muon data is the measurement of the response of cells as a function of radial depth, which allows setting the EM scale for all compartments. With electron beams EM scale was obtained in the first radial compartment (A layer) (Anderson et al., 2008), while for the other two compartments (BC and D layers) muon data is used to correct the EM scale. In addition, the response to muons at $\pm 90^{\circ}$ can be measured for each segment of a tile-row within a cell (tile-row segments and cells can be seen in Figure 2.6) (Adragna et al., 2009). The results of these studies are the main subject of this section.

3.1 Interaction of particle with matter

Charged particle loose energy when traversing through material in different processes (A.K Olive, 2006):

- The charged particle loose energy due to the inelastic collision with atomic electron, this

energy lose can be expressed by the Bethe-Bloch formula:

$$-\langle\frac{dE}{dX}\rangle = Kz^2\frac{Z}{A}\frac{1}{\beta^2}[\frac{1}{2}\ln\frac{2mc^2\beta_2\gamma^2T_{max}}{I^2} - \beta^2 - \frac{\delta(\beta\gamma)}{2}] \tag{3.1}$$

Where, z is charge of the incident particle, m is mass of the incident particle, Z is charge of the medium, A is atomic mass of the medium, I is mean excitation energy of the medium, δ is density correction, β is velocity and γ is Lorentz vector, T_{max} is maximum energy transfer in single collision.

- The charged particle may get deflected by the elastic scattering with the atomic nuclei. If the momentum of the particle is small enough then the multiple scattering becomes important.

- If the particle velocity inside the material is comparable with the speed of light in that material then the charged particle starts loosing energy through Cherencov radiation. The emission angle (θ_c) with respect to the particle direction is given by:

$$\cos\theta_c = \frac{1}{\beta n} \tag{3.2}$$

Where β is the velocity of the particle and n is the refractive index of the material the particle traversing through.

- Strongly interacting particles like protons, charged pions or charged kaons can interact with nuclei in the detector material by nuclear interactions. In case of inelastic interactions the particle will be absorbed inside the material.

- The lighter charged particle emits Bremsstrahlung photons in the electric field of a nucleus. The emission probability is inversely proportional to square of the charged particle mass. Above a critical energy, E_c, the energy lose due to bremsstrahlung supersedes the energy lose due inelastic collisions.

Muon is heavier than electron so the probability of the Bremsstrahlung emission is smaller than for the electron. A muon with the energy of 100 GeV or higher mostly looses energy of around 1-2 MeV/gm/cm^2 through ionization and δ electrons, so enough material is needed to stop a muon inside the calorimeter material. However, below 100 GeV the energy lose is mostly dominated by only ionization. The energy lose through ionization reaches minimum at $\beta = 0.96$. For the thin absorber (few meter of iron absorber) the energy distribution has a long

tail and also dE/dX (also reffered to as dE/dl) value differs from the value calculated from the above Equation 3.1, due to smaller number of atomic nuclei and large fluctuation in energy transfer during collision. Only for the thick absorber like 100 m iron will make the energy loss distribution Gaussian.

3.2 Muon response

It is known that the Bethe-Bloch formula describes the average energy loss of charged particles when travelling through matter, while the fluctuations of energy loss by ionization of a charged particle in a thin layer of matter was theoretically described by L. Landau (L. Landau, 1944). This description ends with a universal asymmetric probability density function. In fact, if a particle does not stop in the detector, the response varies around the distribution's peak, with a high probability of high signals. Because of this tail, the average value is greater than most probable value of the distribution. The fluctuation around the maximum of this distribution becomes greater as the detector material becomes thinner (S. Meroli, D. Passeria, L. Servolia, 2011).

The Landau fluctuation is caused primarily by the rare but measurable occurrence of knock-on electrons, which gain enough energy from the interaction to become ionizing particles themselves. Because the direction of the knock-on electron is typically perpendicular to the direction of the incoming particle, it causes irregular charge clouds and degrades spatial resolution.

Muon response has been studied determining the ratio between the energy deposited in a calorimeter cell (dE) and the track path-length in the cell (dX, or sometimes referred to as dl). The experimental and the simulated distributions of this quantity for cell A-8 are shown in Figure 3.1. The curve in the figure is a fit of Landau functions, convoluted with Gaussians, to the data. Despite the qualitative agreement, the fits show some instabilities and give very low χ^2 probabilities. This indicates that this analytical form does not describe the distributions over the whole range and thus may yield to biases in evaluating parameters such as the peak value, which depends on the material thickness. For this reason a truncated mean, $\langle dE/dl \rangle_t$, was used to define the muon response. For each TileCal cell it was computed by truncating a fraction (F=2.5%) of entries in the upper side of the dE/dl distributions. The truncated mean was preferred to the full one because it is less affected by rare energy-loss processes, such as

bremsstrahlung or energetic δ-rays that can cause large fluctuations on the mean. It is noteworthy that the truncated mean exhibits a slight non-linear scaling with the path length dl .

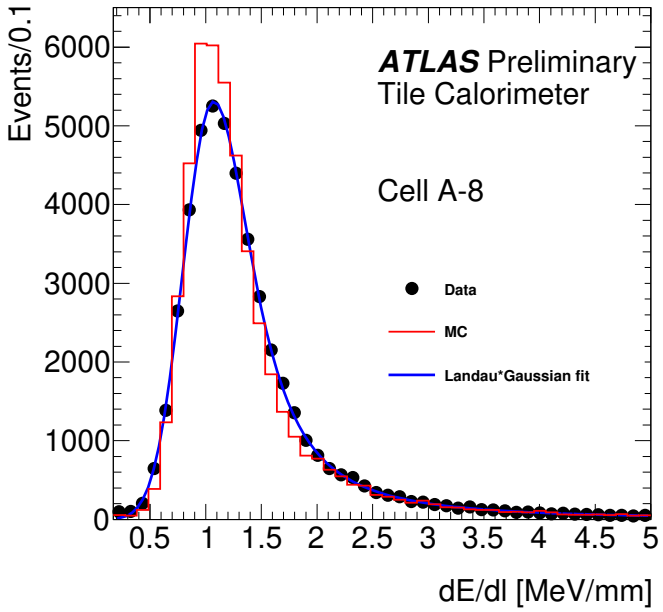

Figure 3.1: Distribution of the quantity dE/dl for the cell A8 obtained using experimental (full points) and simulated muons (solid lines) at 90° hitting in the middle of A layer. The curve shows fit of Landau function, convoluted with Gaussians, to the data.

3.3 Response of individual PMTs in A Layer to 90° muon beam

The following work is the analysis of Demonstrator data. The first step is reconstruction of the signal in ADC counts. The linearity of the ADC's is determined using the Charge Injection System (CIS).

It is important to distinguish between real muon signal and electronics' noise events, that may be caused by false triggering. OF and Fit reconstruction methods give identical results for good signals (in ADC counts) above noise threshold (Figure 3.2 and 3.3).

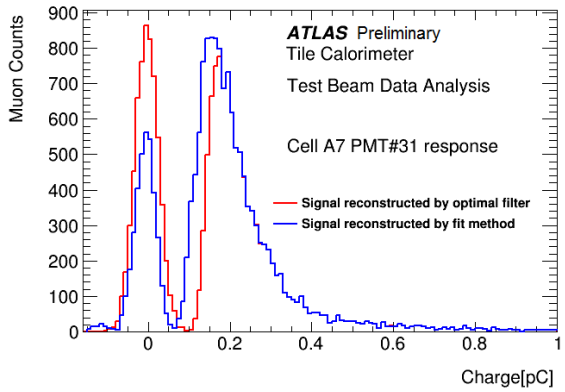

Figure 3.2: Amplitude reconstructed using optimal filtering method (red distribution) and fit method (blue distribution) (cell A7 PMT# 31).

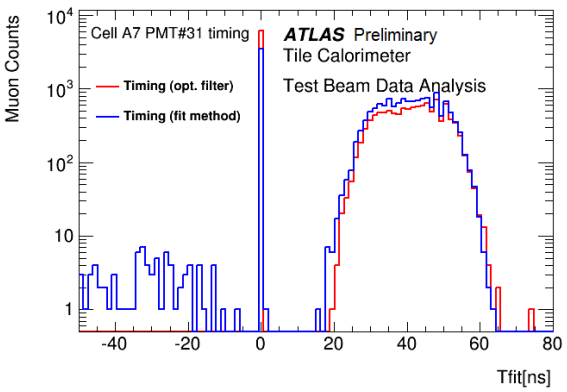

Figure 3.3: Timing reconstructed using optimal filtering method (red distribution) and fit method (blue distribution) (cell A7 PMT# 31).

Behavior for small signals in Figure 3.2 is different because different noise thresholds are used:

- 5 ADC counts in OF
- 3.2 ADC counts in Fit method

Peak at zero in Figures 3.2 and 3.3 represents events reconstructed without iterations. To keep signal events, following cuts have been used:

- Time cut I - reconstructed time should not be equal to 0, this cut effectively selects events which have some signal above noise threshold.
- Time cut II - to remove noise from fake signals, the correct time interval (50 ns time window, Figure 3.3) was selected, so that reconstructed time was compatible with triggering time.

3.3.1 Optimization of the noise threshold

To separate low muon signal from noise, optimization of the noise threshold is needed. Initial threshold values of 5 ADC counts (in OF) and 3.2 ADC counts (In Fit method) were found to be non-optimal. Smaller noise in new electronics allowed to keep smaller muon signals

for analysis. Instead of single threshold value for all the channels, different values of noise thresholds - proportional to electronics noise RMS in a given channel, were studied:

$$\text{threshold} = C \times \text{sampleRMS, where C=2,3,4;}$$

The implementation of the different noise thresholds for different channels is possible in OF method, for this reason this reconstruction method was selected for the analysis.

3.3.2 Evaluation of electronics noise

Electronics noise RMS for each channel was evaluated using amplitude of the first sample (which never contains signal - pedestal). RMS value obtained from first sample distribution indicates what could be the noise variation (Figure 3.4).

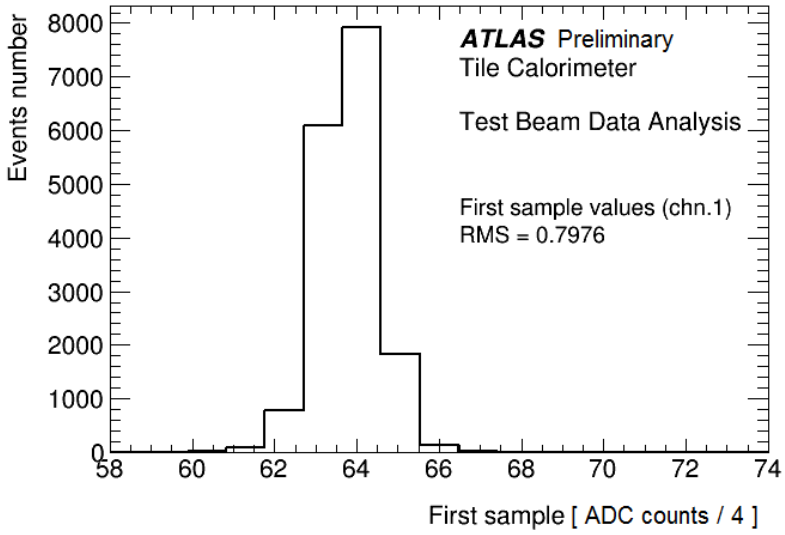

Figure 3.4: First sample distribution for channel 1.

Noise was about 0.75 counts for most of the channels.

In this part of the analysis true 12-bit ADC readout of new system was truncated to 10 bits range, to be compatible with 10-bit readout in legacy system (i.e. actual signal in ADC counts is 4 times bigger).

After selecting reconstruction method and applying cuts on time for each event (section 3.3), several thresholds were considered for noise evaluation:

$$C \times \text{sampleRMS, where C=2,3,4;}$$

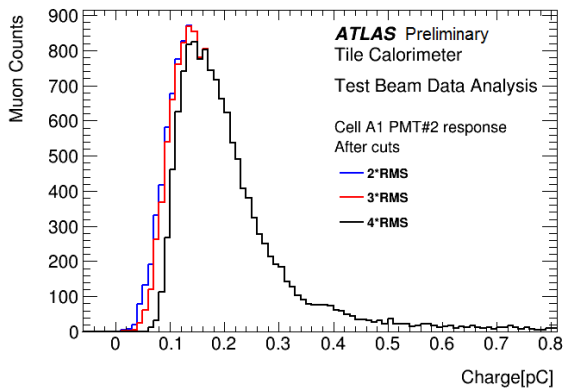

Figure 3.5: Cell A1 PMT# 2 response (blue distribution - 2×sampleRMS, red distribution - 3×sampleRMS, black distribution - 4×sampleRMS).

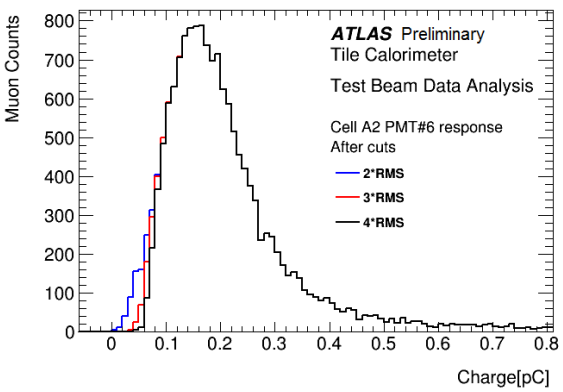

Figure 3.6: Cell A2 PMT# 6 response (blue distribution - 2×sampleRMS, red distribution - 3×sampleRMS, black distribution - 4×sampleRMS).

As a noise threshold 3×sampleRMS was selected. Distribution behavior in low signal range is more like Landau distribution in this case (Figures 3.5- 3.6).

After choosing a threshold for reconstruction method, cell signal was evaluated (Figures 3.7 and 3.8). To obtain a cell response, corresponding two PMTs' signals were summed up (time cuts applied).

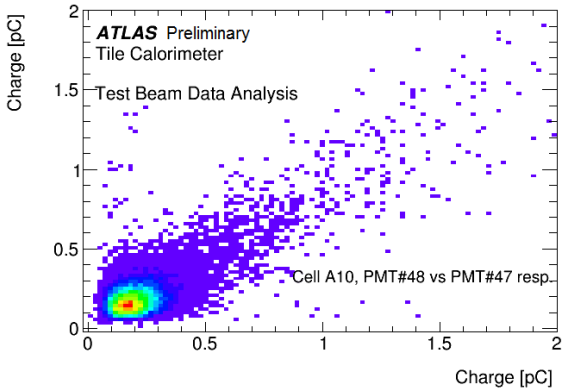

Figure 3.7: A10 cell PMT# 48 vs PMT# 47 signal response.

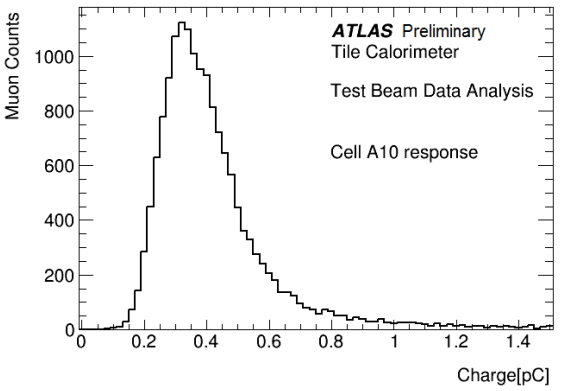

Figure 3.8: A10 cell signal response.

3.3.3 Muon response per unit length for A layer

It is important to evaluate muon energy loss per unit of length in LBC65 barrel. Because muon weakly interacts with material, it deposits energy proportional to the traversed path length.

For this purposes dE/dX (energy loss per unit of length) value is calculated for each cell of A layer, with expectations that the measured signal on unit of length will be close in value, in each cell.

During the Test Beams, electronics' gain was increased by factor of 5, which amplified low muon signal, and helped to separate noise from signal with the total energy cut, that removes false trigger events. OF method was chosen as a reconstruction method and as a noise threshold was set value close to $3\times$noise RMS (2 ADC counts).

June, 2017 Test Beam data of 165 GeV muons hitting Demonstrator at +90°, were analyzed to calculate muon signal (in ADC counts) in each cell, which is the sum of the reconstructed energy in each PMT.

To select the signal, following cuts were applied (signal cuts):

- Cut on Total Energy: $500 < E_{tot} < 2500$ ADC counts (Fig. 3.9);
- Cut on Beam Chambers: collimated beam spot was selected (area of 4 cm^2).

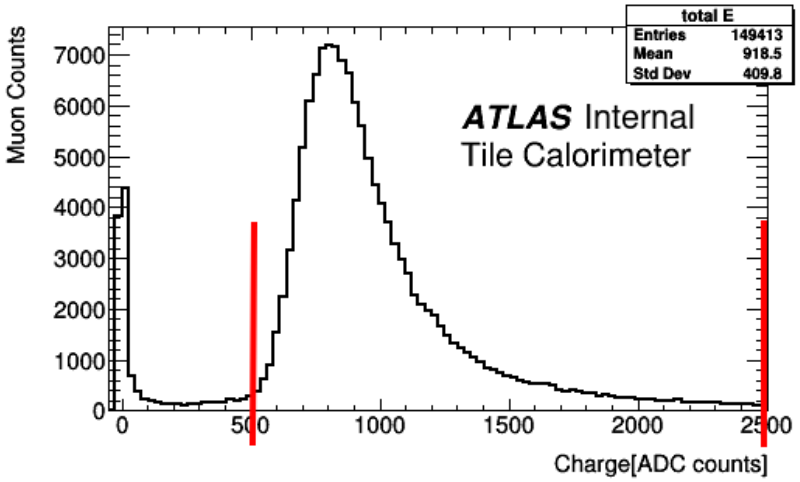

Figure 3.9: A layer's total Energy distribution. Noise threshold - $3\times$RMS (TB June, 2017).

After applying cuts mentioned above, noise peak around zero diminishes (Fig. 3.10 - red distribution).

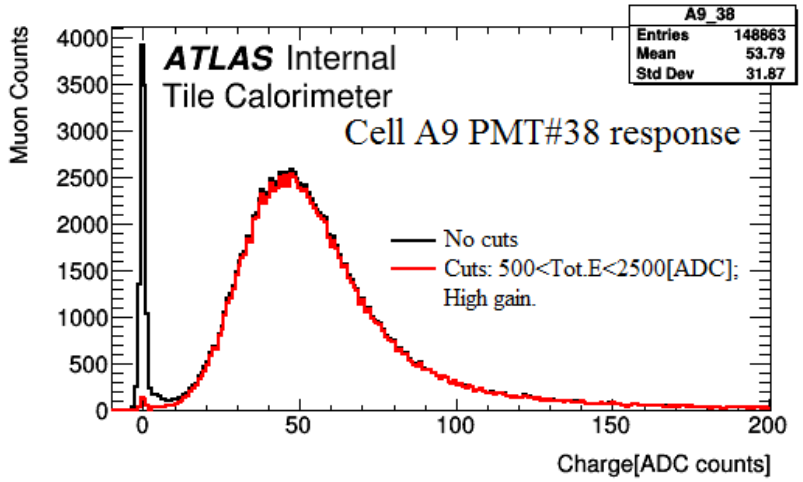

Figure 3.10: Cell A9 PMT# 38 response. With black distribution is shown muon response without signal selection cuts and with red distribution - muon response after applying signal cuts (TB June, 2017).

To calculate dE/dX for each cell, as dE value was used truncated mean (97.5%) value of the distribution, and as dX value was used corresponding cell length.

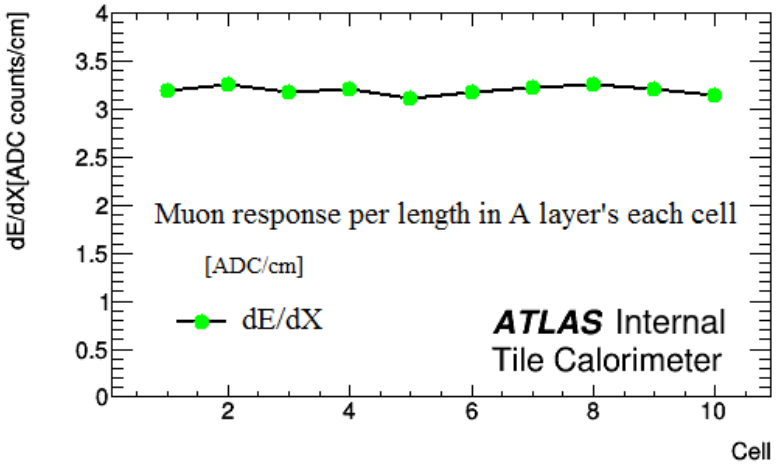

Figure 3.11: dE/dX [ADC/cm] distribution obtained for A layer (every tile-row data, June, 2017), errors on the figure are statistical only and are very small in value.

From Fig. 3.11 we can see that distribution is flat, with the spread of 1.6%. As a result of this approach expected muon behavior was obtained.

Afterwards, signal obtained in ADC counts was converted to GeV, by applying corresponding calibration coefficients described in section 2.8

3.4 Data and Monte Carlo Comparison

Monte Carlo simulation is used to check the new electronics prototype - Demonstrator signal reliability and it's calibration procedure. Also by comparing Data to MC it can be assessed if data is treated correctly to select muon signal.

The experimental results obtained using muon beams, with energies in the range 160-300 GeV, were compared to the predictions of the Geant4-based ATLAS simulation program (Agostinelli et al., 2003). The responses of the beam counters and Cherenkov counters were not included in the event simulation. The TB detector material and geometry were fully described (see Ref. (Allison et al., 2006)). The measured electronics noise in the different calorimeter cells and the effects of photo-statistic (70 photo electron per GeV) in the PMT signals, are included in the MC simulation.

Results shown below (Figure 3.12) are obtained using data that were taken with 160 GeV muon beams incident at -90° in the middle of each of the 11 tile-rows of the Demonstrator module. The events were selected requiring a total energy reconstructed in the module in the window of $700 < E_{tot} < 15000$ MeV and by selecting collimated beam spot (area of 4 cm^2). The ratio between the experimental and simulated truncated means was defined for each calorimeter cell. Figure 3.12 shows the ratios as a function of the cell number of the three layers. In the figures, the horizontal lines correspond to the mean values of the determinations for each layer.

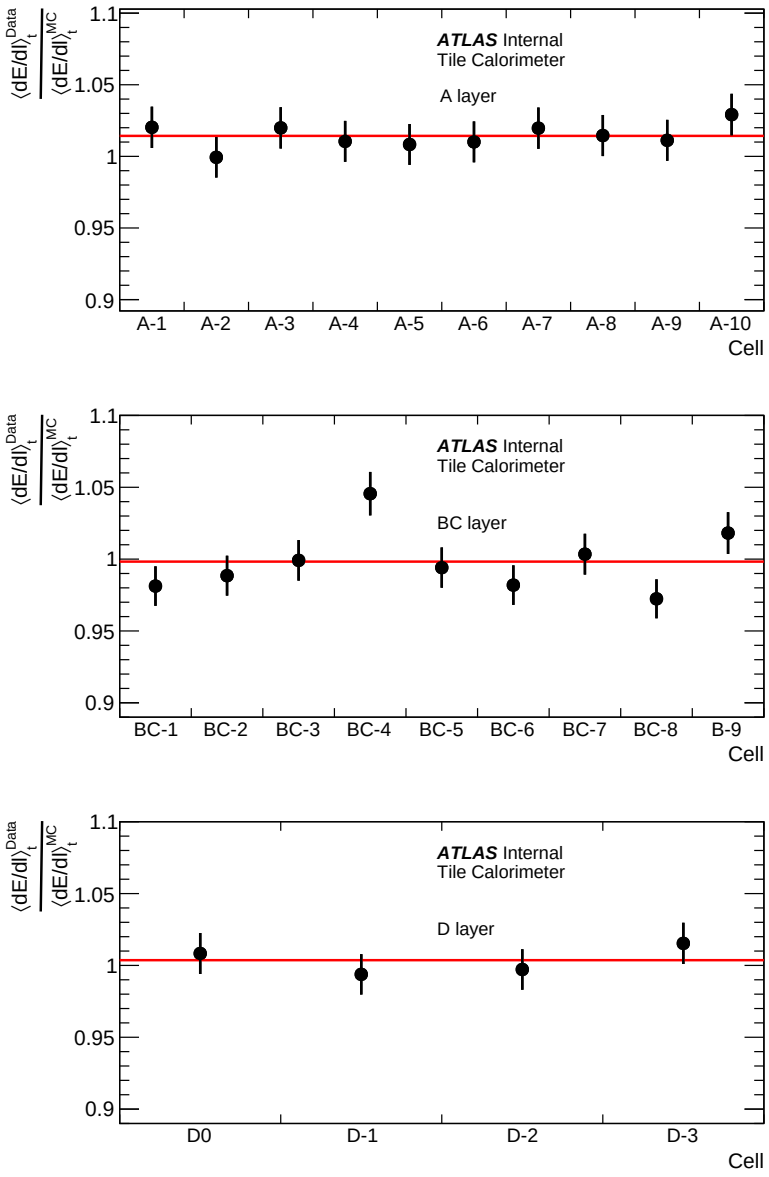

Figure 3.12: Ratios of the truncated means of the distributions of the energy deposited in the layer cells per unit of path length obtained using $-90°$ experimental and simulated muon data as a function of the cell number. The horizontal lines correspond to the mean values of the determinations. 2018 May TB data, 160 GeV muon data.

Layer	Mean	Uncertainty
A	1.014	0.005
BC	0.998	0.005
D	1.004	0.007

Table 3.1: Determinations of the layer responses. For each layer the mean value and corresponding errors are reported.

The errors on the plot include systematical and statistical errors. Systematical error assigned to truncated mean of Landau distribution was calculated using simulation, where muon beam was hitting the testing module at $-90°$. Simulated data was divided into several subsets, with event numbers similar to data recorded at Test Beams. Error on the mean of sub-set truncated mean values was 1%, which later was assigned as a systematical error to calculated truncated mean values.

The data show a layer response uniformity within 1% (see Table 3.1). An offset of max 1.4% is observed for Data/MC for A layer, 0.2% for BC layer and 0.4% for D layer. Energy response uniformity is observed cell by cell within uncertainties. Some small fluctuations are visible in BC layer, which could be due to the settings used in Test Beams that weren't fully taken into account by calibration procedures.

3.5 Detector calibration procedure

Muons entering the calorimeter modules at $\pm 90°$ along the centers of the tiles are used to study the uniformity of the individual cell response and also to test, whether the EM scale is preserved in the second and third calorimeter compartments, where most of the cells can not be reached by the electron beams. According to previous studies the EM scale was found to be 1.05 pC/GeV, with uncertainty equal to 2.4% (Abdallah et al., 2013).

The cesium system (Blanchot et al., 2020) is used as the primary tool to equalize the gain of all calorimeter cells. During cesium calibration a radioactive ^{137}Cs source passes through all TileCal cells, through holes in every scintillating tile and absorber plate. The holes for cesium calibration tubes are located 13 mm from the outer radius edge (distance from pp collision point) of the trapezoidal-shaped tiles (independently of the tile size), on its symmetry axis, as shown in Figure 2.4. the response of each tile-row segment has been corrected by the corresponding

normalized Cs source result.

Additional correction factors are needed to the Cs source calibration - C_μ correction factors, to preserve the EM scale in all calorimeter compartments (Anderson et al., 2008).

The difference between the calorimeter response to particles and to Cs source originates in the non-uniformity of the individual tile response across its surface. The pipes carrying the Cs source run through holes in the tiles near their outer edges. A dedicated measurement shows that more than 90% of light produced when the Cs source traverses the tile is collected from a circle around the hole. After the cells response is equalized with Cs calibration, the muon response depends on the tile-row number. This feature is partially corrected by applying correction factors in individual radial compartments.

To study energy response uniformity of Tile Calorimeter module each tile-row was irradiated by muon beam in the center (see Figure 3.13) and energy response on unit of length was evaluated fom each tile-row.

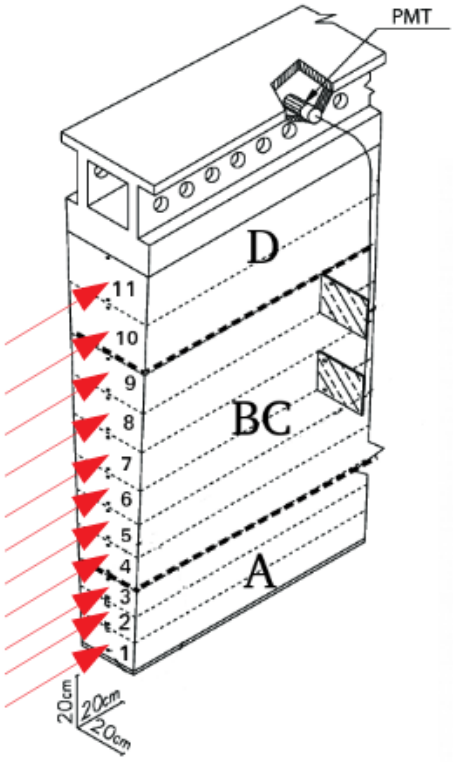

Figure 3.13: Schematic view of LB module irradiation using -90°muons incident on individual tile-row's center. Red arrows show beam direction.

As mentioned before, the TileCal response to high energy muons follows a Landau type distribution with characteristically long tails at high energies (see Figure 3.1). The energy is

obtained as the sum of the reconstructed energy in each PMT of a cell. The mean value of the measured muon energy loss spectrum, truncated at 95%, was adopted as a cell response. The reason for choosing this truncation point is that around 5% of muon beam was contaminated with hadrons.

Used cuts to purify muon beam were:

- Beam Chamber cuts: collimated beam spot selected (area of 4 cm^2)
- Total Energy cut ($<\sim$16 GeV): rejecting other particles in the beam.
- At least in one PMT high signal ($>\sim$ 0.06 GeV): to reject false trigger muons.

Detailed measurements of the response of tiles to collimated Sr β-source have shown, that there is a systematic decrease of the tile signal collection with position of the source along the tile radius of 1 %/cm to 2 %/cm from the outer edge to the inner edge of the trapezoidal tiles (Errede et al., 2008). Cs scans excite tiles near the outer radius holes, which have their center always placed 13.5 mm from the tile edge, while particles from $\theta = -90^{\circ}$ beams enter the center of tiles. As an example, in tiles of tile-row 11 (included in the third compartment), the distance between the tile center and the Cs hole is 80 mm, while in tiles of tile-row 1 (belonging to the first compartment), this value is only 35 mm. This distance difference and the 1 %/cm to 2 %/cm signal decrease in the radial direction of the tile causes an under-calibration of tile-row 11 (in D layer) with respect to tile-row 1 (in A layer) of 4-8%. Similar considerations are valid for other tile sizes with under-calibration increasing with the tile size, i.e. for tiles located at larger radius (further from the pp collision point).

After Cs equalization is performed, the correction for the layer response (C_{μ}) is obtained using the 300 GeV muons hitting at -90° in the middle of the cells tile-rows (see Figure 3.14). The observed variation of the muon signal with tile-rows is well understood. The initial equalization of the PMT signals from different cells is based on the response of every tile-row to the ^{137}Cs source signal and on the assumption that it characterizes the response of the scintillators to EM showers. However, as mentioned above, the response of tiles is not uniform across their surface.

The correction in the radial compartment A is set to one, in order to preserve the EM scale as determined with electrons at 20°. The correction factors for the second and third radial compartment are the ratios of the mean responses of the tile-rows of the first compartment to the mean muon responses of the tile-rows of second and third compartments, respectively.

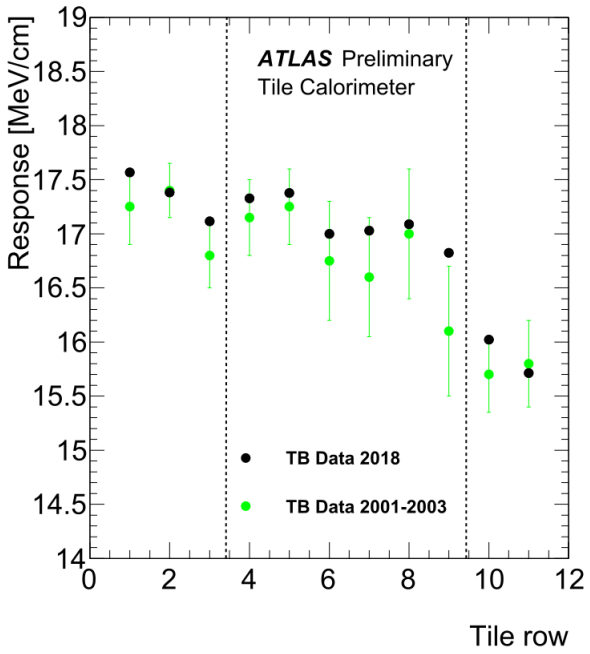

Figure 3.14: The signal of LBC65 module per unit path length produced by -90°muons incident on individual tile-row's center. Green points represent TB 2001–2003 results, black points represent TB 2018 results. For TB 2001–2003 the error bars represent RMS spread over several analyzed modules, whereas for TB 2018 only one module was analyzed. ^{137}Cs source calibration applied for both cases.

The weights (the factor C_μ) in the second and third radial compartments, as mentioned above, are evaluated as the inverse ratio of the mean muon responses in the respective tile-rows to the mean responses of the three A-layer tile-rows, see Table 3.2. In the table are reported results obtained from TBs held in 2001–2003, where 8 modules' results are combined, and results obtained from TB held in 2018, where only one module's (Demonstrator's) results are shown, they are in agreement within uncertainties.

Layer	C_μ - TB 2001–2003	C_μ - TB 2018
A	1.000	1.000
BC	1.025 ± 0.002	1.014 ± 0.008
D	1.088 ± 0.005	1.094 ± 0.010

Table 3.2: The Determination of C_μ

3.5.1 Justification of the method

The remaining question is whether or not the light response from the center of the tile is an accurate representation of its surface and how this response depends on the tile size. The ratio R of the central region average response over the full region average response of the tile is tile size independent, according to the past analysis, which was estimated using a Sr source scanning (S. Errede et al., 2009).

The tile-rows have trapezoidal shapes. In TileCal there are 11 types of tiles. Their dimensions are reported in Table 3.3. In the Long Barrel the tiles S1-S3 belong to layer A, the tiles S4 to S9 to layer BC and tiles S10 and S11 to D. In the EB the situation is the following: tiles from S1 to S3 belong to layer A, tiles from S4 to S7 to layer B and from S8 to S11 to layer D.

Tile	Altitude [mm]	Max side [mm]	Min side [mm]	Radius$_{min}[mm]$	Radius$_{max}[mm]$
S1	97	228.7	219.1	2301.5	2398.5
S2	97	238.5	229	2401.5	2498.5
S3	97	248.3	238.8	2501.5	2598.5
S4	127	261.1	248.6	2601.5	2728.5
S5	127	273.9	261.4	2731.5	2858.5
S6	127	286.7	274.2	2861.5	2988.5
S7	147	301.4	286.9	2991.5	3138.5
S8	147	316.1	301.7	3141.5	3288.5
S9	147	330.9	316.4	3291.5	3438.5
S10	187	349.5	331.1	3441.5	3628.5
S11	187	368.2	349.8	3631.5	3818.5

Table 3.3: Tile dimensions.

In this analysis the scanning was performed using -90°muons. At test beams, surface of three type of tiles were scanned using muon beams by irradiating different tile-rows (see Figure 3.15):

- Tile-row 2 - with 165 GeV muon beam
- Tile-row 6 - with 300 GeV muon beam
- Tile-row 10 - with 300 GeV muon beam

Impact point was calculated using the two Beam Chambers of the beam line.

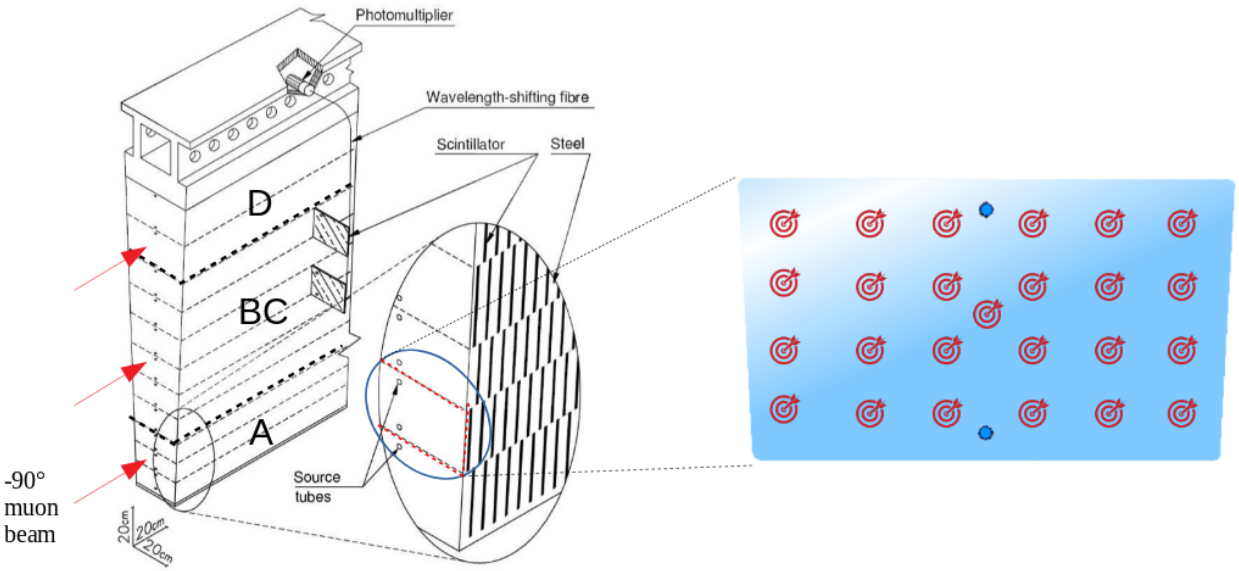

Figure 3.15: During TB 2018 scanning runs were taken for tile-row 2, tile-row 6 and tile-row 10. Red circles represent beam spot center hitting points, beam spot itself is around $4cm^2$ (not drawn to scale).

R - is defined as the ratio of central region (4 cm x 4 cm) average response to whole tile surface average response:

$$R = \frac{\langle S_c \rangle}{\langle S_f \rangle} \tag{3.3}$$

Where S_c corresponds to central region (4 cm x 4 cm) response, and S_f corresponds to full tile surface response (excluding 2mm around the edges).

Tile-row №	R
2	1.034 ± 0.005
6	1.045 ± 0.011
10	1.038 ± 0.002

Table 3.4: R values for irradiated tile-rows.

in Figure 3.16 is shown irradiated tile-rows' surface response. Central region average response is $\sim 3.9\%$ bigger than the total tile surface average response for tile-rows studied. It is tile size independent within uncertainties, see Table 3.4. The R ratio is > 1 due to the fact that tile has a trapezoidal shape and it's response is not uniform across the surface.

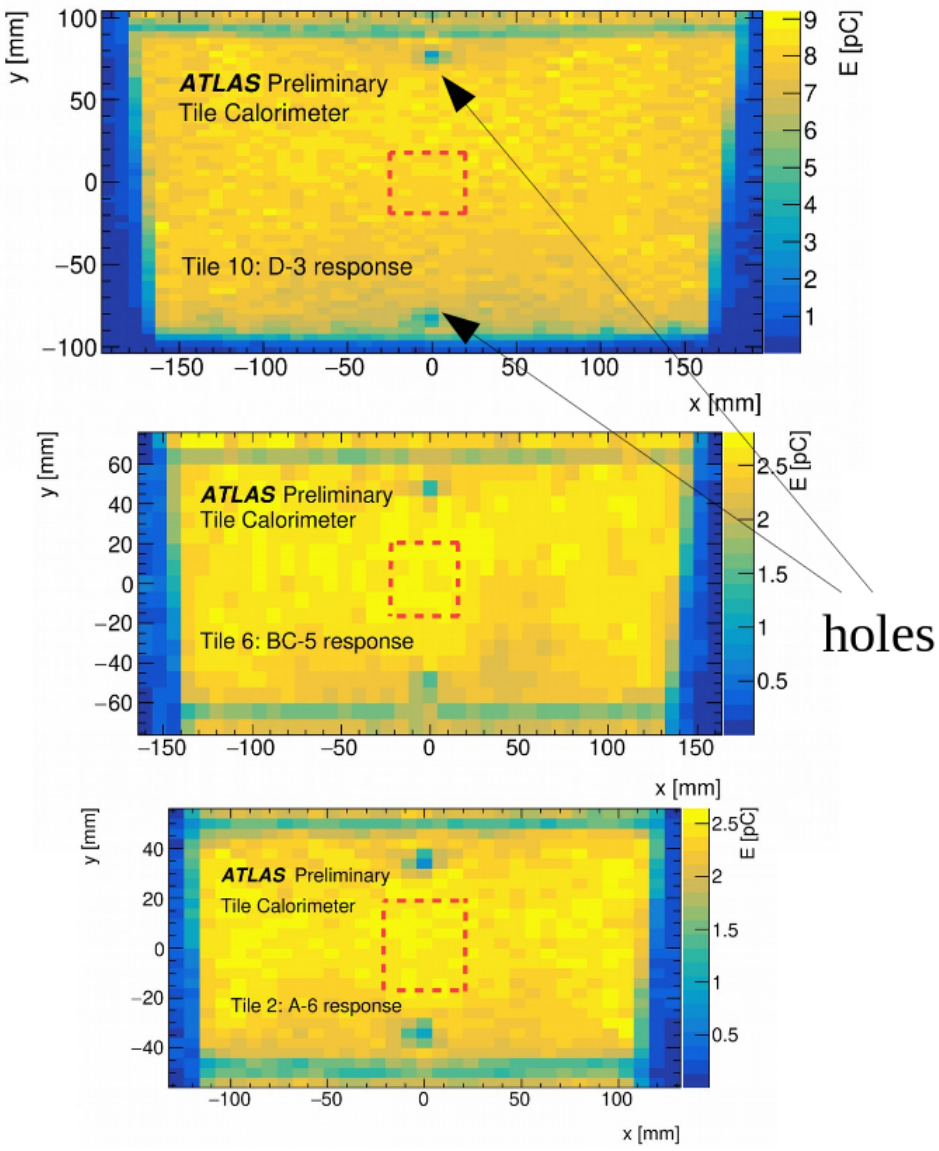

Figure 3.16: From top to the bottom: energy response for tile-row 10, tile-row 6 and tile-row 2.

3.6 Study of the scintillating tile response using a ^{90}Sr source

The motivations of this study is to check if the average Sr source response at the center region of a tile is equal to the one of the full tile and compare it to the results obtained using muon data at the TileCal test beams.

A picture of the setup used for the measurements is shown in Figure 3.17, where one can see the scintillating tile to be measured (1); the radioactive source ^{90}Sr (the maximum energy

spectrum is 546 keV and the half lifetime 28.8 years) (2); the scanning mechanism (the steps are 1 mm in the x and y coordinates of the plane defined by the tile) (3); the WLS green fibers (4); the Hamamatsu R7877 photomultiplier (PMT) used for the measurements (5); reference tile for calibrating response of different scans (6).

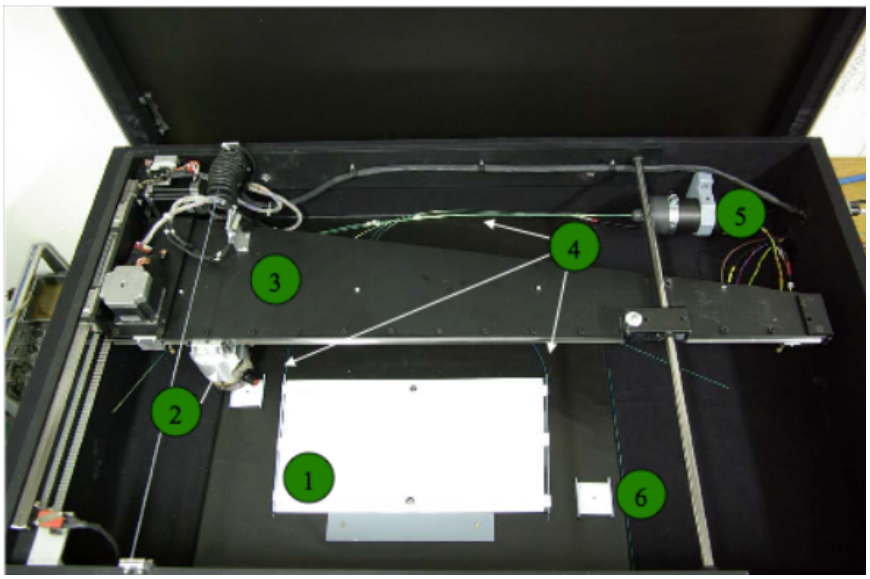

Figure 3.17: The setup used for measurements.

3.6.1 The response of the tile surface

As already mentioned, the tile-row is read by two PMTs, though in this setup tile is read by one PMT. Figure 3.18 shows an example of the response as a function of the position of the source in the plane (x, y). For each point of a tile, the two PMTs response can be obtained adding to the measured signal the one obtained at the point P' = (x', y'). The coordinates P' are obtained from P applying a parity transformation with respect to the plane x = 257 passing by the tile center.

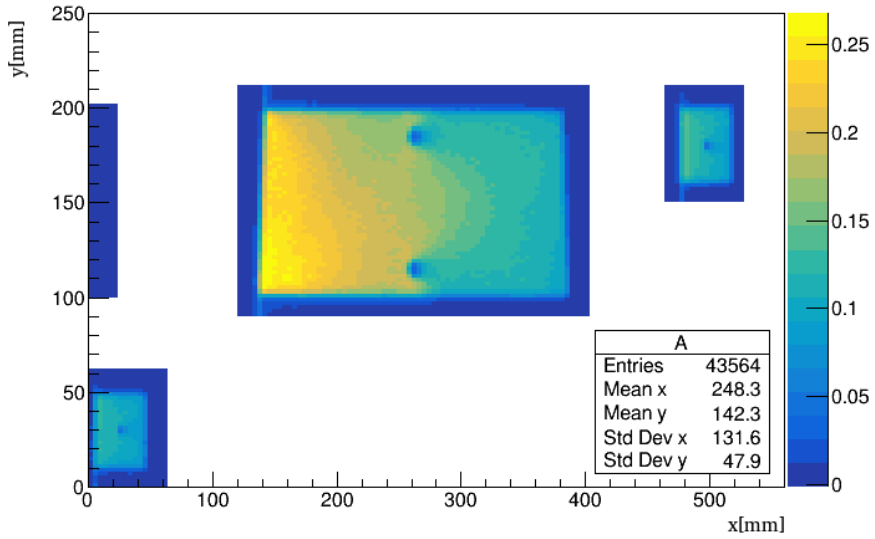

Figure 3.18: Scatter plot of the measured signals as a function of the position of the Sr source in the (x, y) plane.

3.6.2 The ratio of the tile response on the central region over the one in the full tile surface

In the calibration procedure the layer inter calibration was obtained using responses measurement of muons hitting the calorimeter at the center of a tile at $90°$. Results based on previous Sr measurements show that the ratios R of the average responses obtained in the central and in the full tile regions are equal for all tile sizes. This result has been tested using the new Sr measurements and the results are discussed below.

In current measurements, the considered central region has a surface of $4cm \times 4cm$. Only signals obtained, when the source was positioned on the top of the tile, were considered and the ratios of the signal averages in the central and full regions (not excluding 2mm around the edges) were determined

$$R = \frac{\langle S_c \rangle}{\langle S_f \rangle}. \tag{3.4}$$

3.6.3 Results of different Sr data sets

The scintillator tiles, used in Tile Calorimeter were produced in several batches, and two different materials were used, PSM-115 and BASF-165H polystyrene materials. The scintillators were sorted, according to the light yeild to provide uniformity of the cell. In the testing mod-

ule's A cells PSM and BASF tiles had to be combined, whereas for BC and D cells BASF tiles were used.

Three samples of each tile size was scanned, both PSM and BASF polystyrene material. R ratio is calculated and reported in Table 3.5, and shown in Figure 3.19.

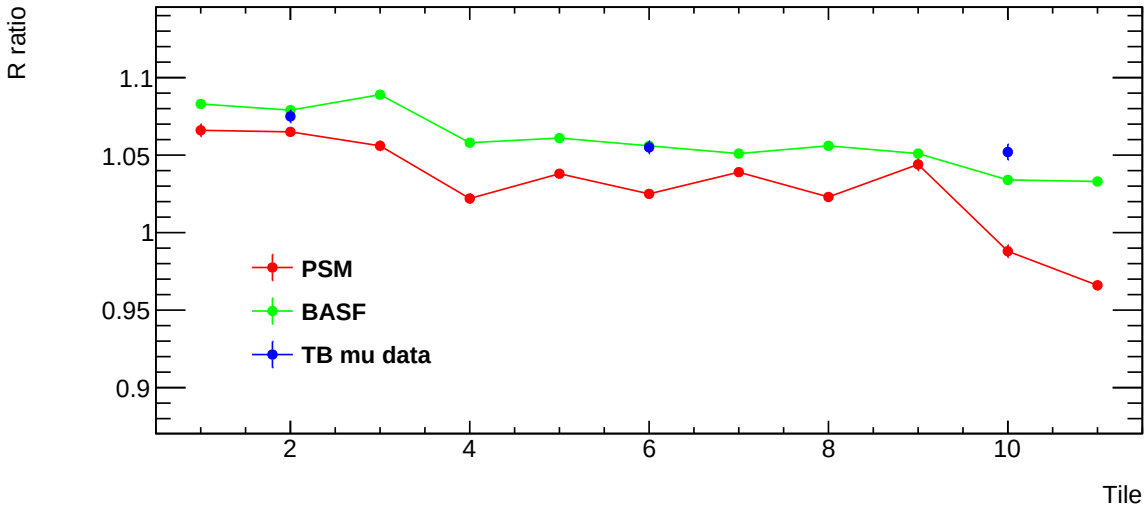

Figure 3.19: R values vs Tile size, obtained by muon data analysis (blue points) and obtained by Sr data analysis for PSM (red points) and BASF (green point) polystyrene materials.

Tile size	PSM	BASF	muon data
1	1.066 ± 0.004	1.083 ± 0.002	-
2	1.065 ± 0.002	1.080 ± 0.003	1.075 ± 0.004
3	1.056 ± 0.003	1.089 ± 0.002	-
4	1.022 ± 0.003	1.058 ± 0.002	-
5	1.038 ± 0.001	1.061 ± 0.001	-
6	1.025 ± 0.001	1.056 ± 0.001	1.055 ± 0.004
7	1.039 ± 0.001	1.051 ± 0.001	-
8	1.023 ± 0.001	1.056 ± 0.001	-
9	1.044 ± 0.004	1.051 ± 0.001	-
10	0.988 ± 0.004	1.034 ± 0.001	1.052 ± 0.005
11	0.966 ± 0.003	1.033 ± 0.002	-

Table 3.5: R values. For muon data full tile-rows (2, 6, 10) responses were analysed.

For both PSM and BASF material we see that R ratio is decreasing with increasing of the tile size. It must be noted that within different batch production of tile calorimeter scintillators, there is a difference in R ratio, that is few percent. Also within the same batch R ratios may differ from sample to sample. In this case only three samples of each tile were analysed. Muon data results are compatible with Sr data within uncertainties by taking into account different batch effect on R ratio.

Difference between results reported in Table 3.4 and Table 3.5 are caused by different selection criterias. In the first case, as a full region response (S_f) was taken full tile surface response, but excluding 2 mm around the edges, whereas in the second case as a full region response (S_f) was taken full tile surface response, without excluding the edges, which is very sensitive part of the scintillating tile and signal decrease gradient is large in those regions.

3.7 Summary

The LHC Phase–II Upgrade aims to increase the LHC luminosity by a factor of 5-10 ($5 - 10 \times 10^{34} cm^{-2} s^{-1}$). The current electronics is ageing and will be submitted to higher radiation levels, so new electronics are needed to guarantee reliability and reduce maintenance costs. To date, has been built a Demonstrator - a fully functional prototype of the new system. The Demonstrator is a hybrid module equipped with the upgraded electronics that was installed into the ATLAS experiment for the evaluation of the new readout architecture for the ATLAS Phase-II Upgrade.

The interaction of muons with matter is well understood. The high-energy muons traverse the entire TileCal modules for any angle of incidence, thereby allowing a study of the production module response in great detail through their entire volume.

The response of the TileCal Demonstrator module was studied using the 2016–2018 and 2021–2022 test beam data. Demonstrator is equipped with new Phase–II upgrade electronics which will be used for HL-LHC. The Demonstrator response is studied with 150 GeV, 160 GeV, 165 GeV and 300 GeV muon beam hitting the module from $\pm 90^{\circ}$. Noise thresholds of new electronics were evaluated.

The muon data recorded by Demonstrator show a layer response uniformity within 1%. While comparing data to simulation, an offset of max 1.4% is observed for Data/MC for A layer, 0.2% for BC layer and 0.4% for D layer. Energy response uniformity is observed cell by cell within uncertainties.

Muons entering the calorimeter modules at $\pm 90^{\circ}$ along the centers of the tile-rows are used to cross-check the calibration procedure of the TileCal modules. For this reason the light response from the center of the tile was studied using the muon and ^{90}Sr data, by evaluating the ratio of response in the central region to the response averaged over the total tile area (R ratio) as a function of the tile-row number. The current studies showed that, the central region average response is $\sim 3.9\%$ bigger than the total tile surface average response for tile-rows studied. It is tile size independent within uncertainties. The R ratio is > 1 due to the fact that tile has a trapezoidal shape and it's response is not uniform across the surface.

^{90}Sr data analysis showed that for both PSM and BASF scintillating tile material the R ratio is decreasing with increasing of the tile size. It must be noted that within different batch production of tile calorimeter scintillators, there is a difference in R ratio, that is few percent, but for more complete and precise measurement not enough data were available. Muon data

results are compatible with Sr data within uncertainties and by taking into account different batch effect on R ratio.

Chapter 4

Response of testing modules to hadrons

The defining role of hadron calorimetry is to measure the energies of jets. For this purpose, its performance for isolated hadrons is a necessary starting point and is the subject of this study. For this purpose the calorimeter response and resolution to positive pions and kaons and protons, with energies in the range 16–30 GeV were measured. The results are compared with the simulated data produced using the ATLAS Geant4 toolkit.

4.1 Test beam setup for hadron beam

Three spare modules of the Tile Calorimeter, two long-barrels and one extended-barrel, were exposed to hadrons with different energies, at incident angle of $\theta = 14^{\circ}$ at test beams in 2017 (see Figure 4.1).

Hadron beam reaching the testing modules of TileCal is a mixture of pions, kaons, protons, electrons and muons. The counters Ch1 and Ch3 distinguish electrons and pions from kaons and protons. They were filled with CO_2 and He respectively. For the different beam energies different pressure values were set (Abdallah et al., 2021). The Cherenkov counter Ch2 was also filled with CO_2 (see Figure 2.10). The higher pressure in Ch2 allows for the separation of kaons from protons. More details can be found in Ref. (Di Girolamo et al., 2005).

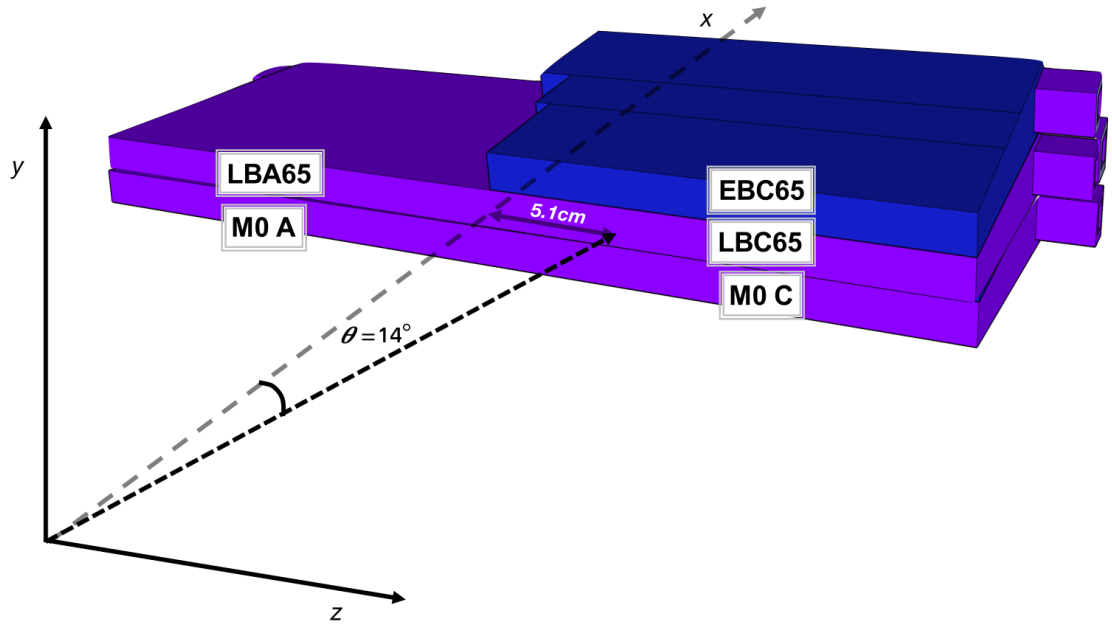

Figure 4.1: Schematic layout of the hadron beam hitting testing modules of TileCal.

As in the ATLAS detector at LHC, the energy deposited in a cell of the TB detector, $E_{\mathrm{c}}^{\mathrm{raw}}$, was determined making use of the Optimal Fit method.

To be consistent, the Optimal Fit method was applied also to reconstruct the energy deposited in the cells in the case of simulated events. The scale of the cell energy measurements was obtained from the cell response to simulated electrons. The energy deposited by the beam particles incident the detector, E^{raw}, was determined as the sum of the energy measured in the calorimeter cells.

4.2 Analysis of experimental data

The results discussed below were obtained exposing the TB calorimeter setup to enriched positive hadron beams with energy, E_{beam}, equal to 16, 18, 20 and 30 GeV. As shown in Figure 4.1, the beams hit at the middle of the cell A3 of the super-drawer LBC65 with an azimuth angle $\phi = 0$ and polar angle from the calorimeter module θ of about $14°$, corresponding to a pseudo-rapidity values $\eta = 0.25$ (see Figure 2.6). For each hadron beam energy, around 1 million events were processed.

4.2.1 Selection of collimated single-particle events

Collimated single-particle events were first selected using beam detectors upstream of the TB calorimeter setup. The selection criteria on the beam line scintillating counters signals, E_{S1} and E_{S2}, were established making use of the responses of S1 and S2 to muons (Figure 2.10). Muon events were recognized by requiring an energy deposited in the module LBC65 compatible with the one deposited by a minimum ionizing particle. The retained events satisfy the criteria:

$$E_{\text{S1}} < 2 \times E_{\text{S1}}^{\text{m.p.}}(\mu) \tag{4.1}$$

and

$$E_{\text{S2}} < 2 \times E_{\text{S2}}^{\text{m.p.}}(\mu) \tag{4.2}$$

where the quantities $E_{\text{S1}}^{\text{m.p.}}(\mu)$ and $E_{\text{S2}}^{\text{m.p.}}(\mu)$ are the most probable (m. p.) values of the S1 and S2 muon signal distributions respectively. These selection criteria remove particles that initiated a shower upstream of the calorimeter, as well as multi-particle beam events. After the application of the criterion (selection 1) the number of events decreases by $\sim 5.4\%$.

Events with a beam trajectory far away from the beam axis were rejected because the beam particles might have scattered upstream and therefore be off-energy. The beam chamber BC1 allows a determination of the transverse beam impact point coordinates, x_{BC1} and y_{BC1}. Gaussian functions were fitted to the distributions of each data set to determine the peak values $x_{\text{BC1}}^{\text{peak}}$ and $y_{\text{BC1}}^{\text{peak}}$ respectively. The accepted events have the beam impact point coordinates inside the square surface of the trigger scintillating counters:

$$|x_{\text{BC1}} - x_{\text{BC1}}^{\text{peak}}| < 2.5cm \tag{4.3}$$

and

$$|y_{\text{BC1}} - y_{\text{BC1}}^{\text{peak}}| < 2.5cm \tag{4.4}$$

After the application of the criterion (selection 2) the number of remaining events decreases by $\sim 15.5\%$ (Abdallah et al., 2021).

4.2.2 Muon rejection

The second set of criteria allows identifying pure samples of hadrons. As already mentioned, muons are minimum ionizing particles and deposit in the scintillating tiles energy much smaller than electrons and hadrons (see Figure 4.2). The muon rejection was obtained requiring a reconstructed energy in the detector $E^{\text{raw}} > E^{\text{raw}}_{\mu\ cut} = 5$ GeV (selection 3). The selection criterion allows also a rejection of spurious trigger events. After the application of the criterion (selection 3) the number of remaining events decreases by $\sim 10.1\%$ (Abdallah et al., 2021).

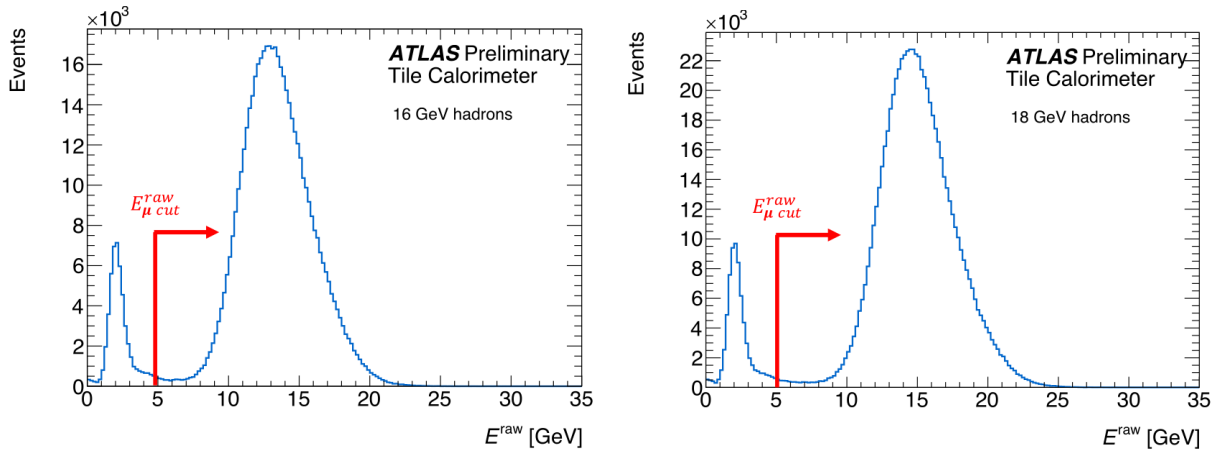

(a) (b)

Figure 4.2: Distributions of the energy E^{raw} in GeV measured in the calorimeter modules in the case of particle beam energies equal to 16 GeV (a) and 18 GeV (b). The events were selected applying the selection criteria up to selection 2. The muons and spurious events were rejected in the analysis requiring E^{raw} larger than $E^{\text{raw}}_{\mu\ cut}$ = 5 GeV as shown in the histograms (Abdallah et al., 2021).

E_{beam} [GeV]	16	18	20	30
Physics Trigger	694658	944460	1226756	1297099
Sel 1.: Beam line scintillators	656262	895863	1155580	1230470
Sel 2.: Beam line chamber	552179	771513	935131	1069709
Sel 3.: Muon and spurious events rejection	501013	700590	777386	983892
e/π	385718	556782	611687	723286
Electrons	67647 $\pm$ 9198	70834$\pm$3665	62137$\pm$3548	28288 $\pm$2481
Pions	318071 $\mp$ 9198	485948 $\mp$3665	549550$\mp$3548	694998$\mp$2481
K/p	86635	133071	154181	137119
Kaons	2372	4674	6782	11296
Protons	84263	128397	147399	125823

Table 4.1: Numbers of collected and retained experimental data events for each of the four beam energy values. The number of events identified as electrons, pions, kaons and protons is reported.

4.2.3 Electron identification

As shown in Figure 4.3, the signals measured in Cherenkov counters Ch1 and Ch3, S_{Ch1} and S_{Ch3} respectively, allow a separation of pions and electrons (e/π) from kaons and protons (K/p). The selection criteria in ADC counts applied on the signals are shown in Figure 4.3 with red lines.

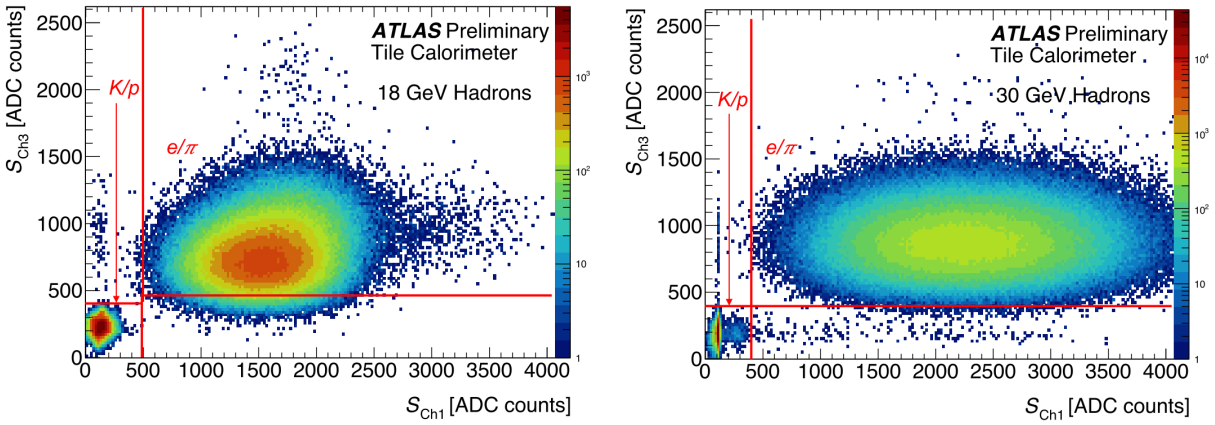

(a) (b)

Figure 4.3: Scatter plots of the signals measured in the Cherenkov counter Ch3, S_{Ch3}, as a function of the signals measured in the Cherenkov counter Ch1, S_{Ch1}, in ADC counts. The histograms were obtained analysing data with beam energies equal to 18 GeV (a) and 30 GeV (b). The events were selected applying the selection criteria up to selection 3. The selection values used to select K/p (left/bottom) and e/π (right/top) events are shown (Abdallah et al., 2021).

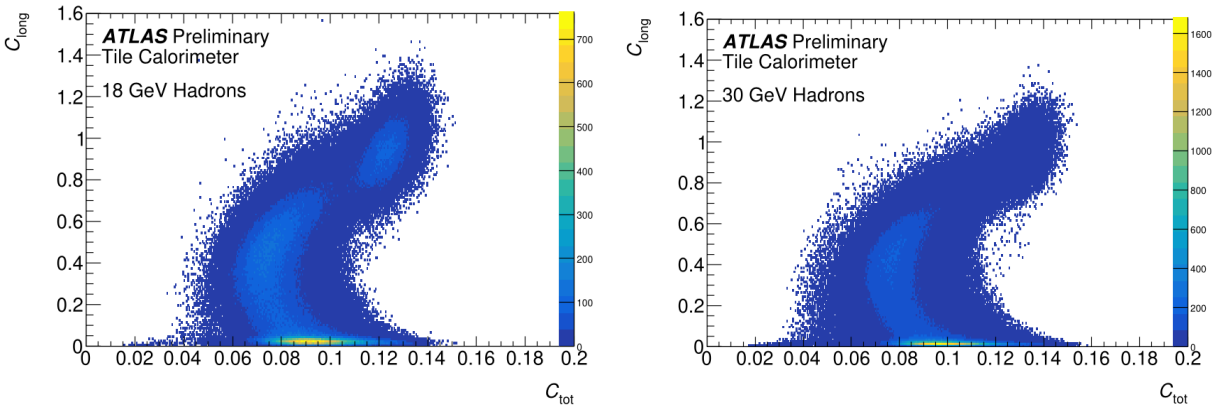

(a) (b)

Figure 4.4: Scatter plot C_{long} vs C_{tot} of e/π sample events produced by particle beams with energies equal to 18GeV (a) and 30 GeV(b) (Abdallah et al., 2021).

The electron components in e/π samples were determined statistically exploiting the difference of electromagnetic and hadronic shower profiles in the calorimeter modules. Two separators, C_{long} and C_{tot}, were used:

- The shower profile parameter C_{long} represents the fraction of the beam energy, E_{beam},

deposited in the layers A of the modules:

$$C_{\text{long}} = \frac{\sum_{i=1}^{3}\sum_{j=1}^{3}(E_{\text{c}}^{\text{raw}})_{i,j}}{E_{\text{beam}}} \tag{4.5}$$

where i = 1, 2 and 3 indicate the super-drawers M0C, LBC65 and EBC65 respectively. The parameter j runs over 3 contiguous cells of the three layers A around the cell hit by the beam and ($E_{\text{c}}^{\text{raw}}$ stands for the energy measured in a cell.

- The separator C_{tot} measures the spread of the energy $E_{\text{c}}^{\text{raw}}$ deposited in the cells of the modules:

$$C_{\text{tot}} = \frac{1}{\sum_{i=1}^{N_{\text{cell}}}[(E_{\text{c}}^{\text{raw}})_i]^{\alpha}} \sqrt{\frac{1}{N_{\text{cell}}}\sum_{i=1}^{N_{\text{cell}}}\left([(E_{\text{c}}^{\text{raw}})_i]^{\alpha} - \frac{1}{N_{\text{cell}}}\sum_{i=1}^{N_{\text{cell}}}[(E_{\text{c}}^{\text{raw}})_i]^{\alpha}\right)^2} \tag{4.6}$$

where N_{cell} = 24 stands for the total number of contiguous cells, around the hit cell, considered for the shower profile estimate and the exponent $\alpha = 0.6$ was tuned using a Monte Carlo (MC) simulation to achieve maximum electron pion separation.

Scatter plots, C_{long} vs C_{tot}, of e/π sample events obtained using particle beams with E_{beam} equal to 18 and 30 GeV are shown in Figure 4.4. They can be compared with the ones in Figure 4.5 obtained using simulated electrons and pions events with the same beam energies. The pions have small values of C_{long} and C_{tot}, while in the case of electrons, the parameters have higher values.

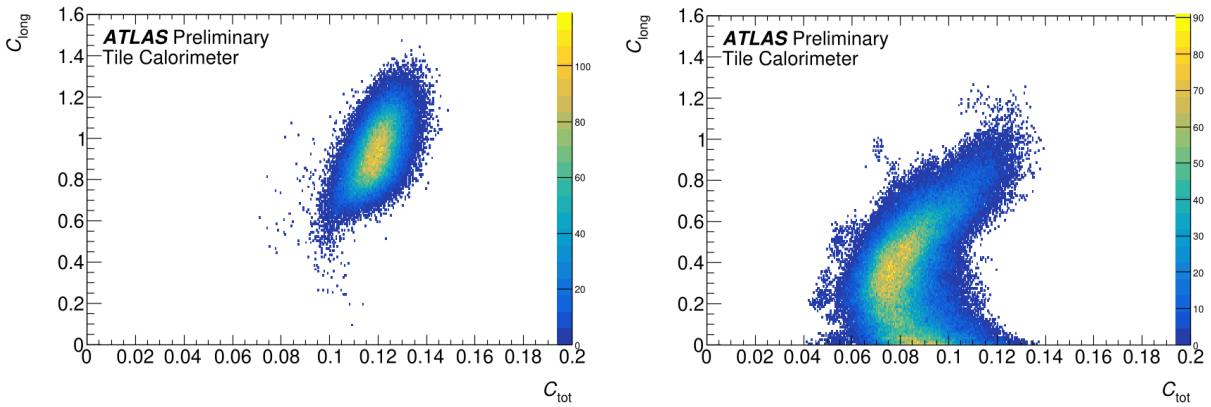

(a) (b)

Figure 4.5: Scatter plot C_{long} vs C_{tot} obtained using simulated 18 GeV electrons (a) and 18 GeV pions (b) (Abdallah et al., 2021).

The analysis is based on the fact that electron (pion) C_{tot} distributions are well described by one (two) Gaussian function. As an example, in Figure 4.6 (a), is shown the experimental

C_{tot} distribution obtained using an enriched electron beam with E_{beam} = 20 GeV and $C_{\text{long}} \geq C_{\text{long}}^{\text{min}} = 0.6$. The fit was performed in the region $C_{\text{tot}} \geq 1.125$. Figure 4.6 (b) demonstrate that also simulated electron C_{tot} distributions at 18 GeV is well described by one Gaussian function.

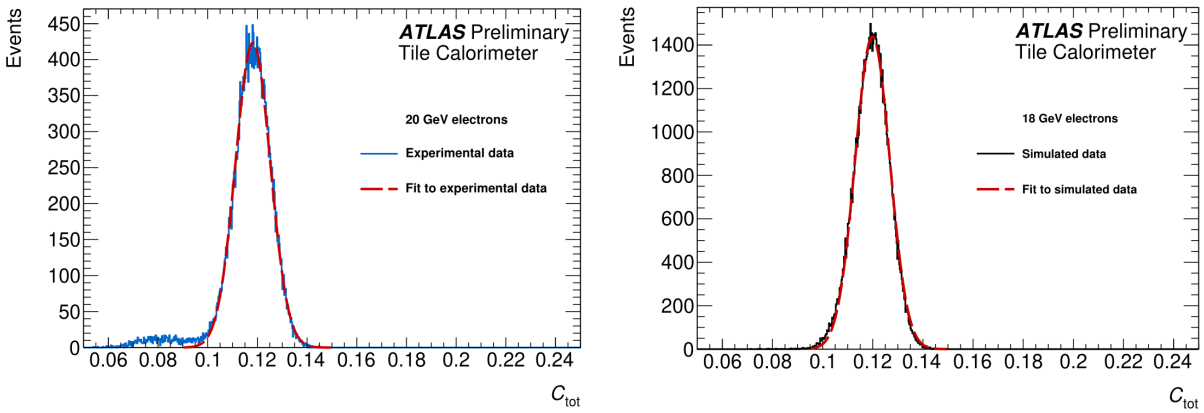

(a) (b)

Figure 4.6: Distributions of C_{tot} obtained using experimental electron-enriched beams of particles with 20 GeV energy (a), and simulated electrons with E_{beam} equal to 18 GeV (b). Fit Gaussian functions obtained using the method of the least squares are overlapped in red to the distributions (Abdallah et al., 2021).

Pion C_{tot} distributions are best described by two Gaussian functions. The distributions of e/π data events with $C_{\text{long}} < C_{\text{long}}^{\text{min}}$ and E_{beam} equal to 18 and 30 GeV respectively are shown in Figure 4.7. Two Gaussian contributions fit is shown. Individual Gaussian contributions are also presented. in Figure 4.8 C_{tot} distributions of simulated pions with E beam equal to 18 GeV (a) and 30 GeV (b) are shown. They are also well described by the sum of two Gaussian functions.

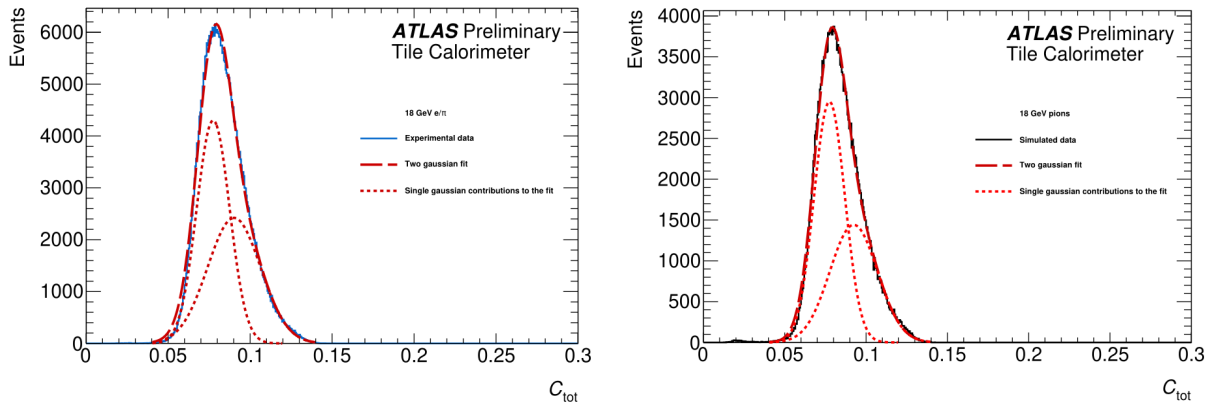

(a) (b)

Figure 4.7: The blue histogram in (a) shows C_{tot} distributions of experimental e/π sample events with E_{beam} equal to 18 GeV. Samples of pion events were selected requiring $C_{\text{long}} < 0.6$. The black histogram (b) show the same distribution for simulated pion events selected applying the same selection criteria and with E_{beam} equal to 18 GeV. Two Gaussian functions fits, obtained using the method of the least squares, are overlapped to the data (red dashed curves). Red dot curves show the individual Gaussian contributions (Abdallah et al., 2021).

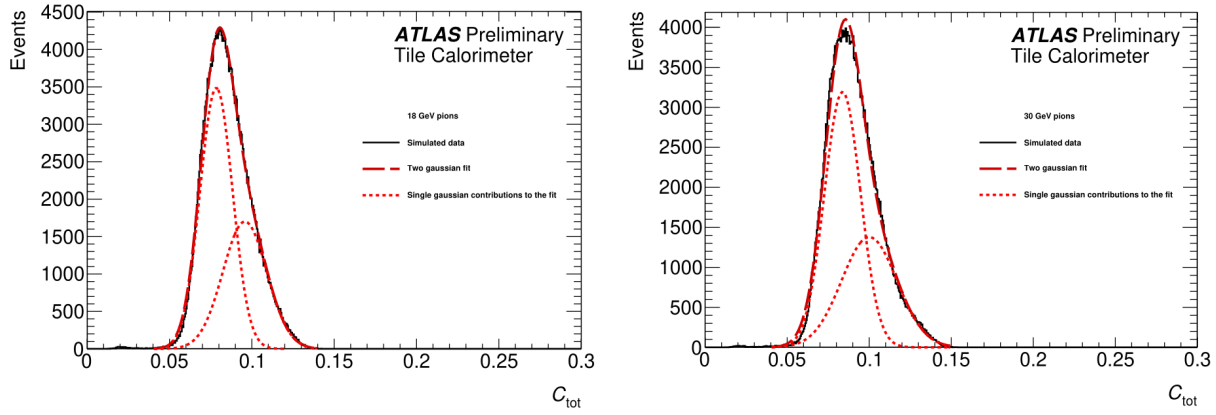

(a) (b)

Figure 4.8: The black histograms show C_{tot} distributions obtained using simulated pions with E_{beam} equal to 18 GeV (a) and 30 GeV (b). The events were selected requiring $C_{\text{long}} \geq 0.6$. Two Gaussian functions fits, obtained using the method of the least squares, are overlapped to the data (red dashed curve). Red dot curves show the individual Gaussian contributions (Abdallah et al., 2021).

The number of electrons in the four e/π samples were determined considering C_{tot} distributions of the events with $C_{\text{long}} \geq C_{\text{long}}^{\text{min}} = 0.6$. Examples of such distributions obtained in

the case of events produced by beams of particle with energies equal to 18 GeV and 30 GeV are shown in Figure 4.9. Three Gaussian function were fitted to the experimental distributions using the method maximum likelihood. The fit functions are overlapped in to the histograms in Figure 4.9. The individual Gaussian function contributions are also shown. The functions with the largest mean values μ describe the electron contributions. The numbers of the electrons are determined from the areas limited by such functions (Abdallah et al., 2021). The statistical uncertainties are equal to the corresponding diagonal terms of the fit error matrices.

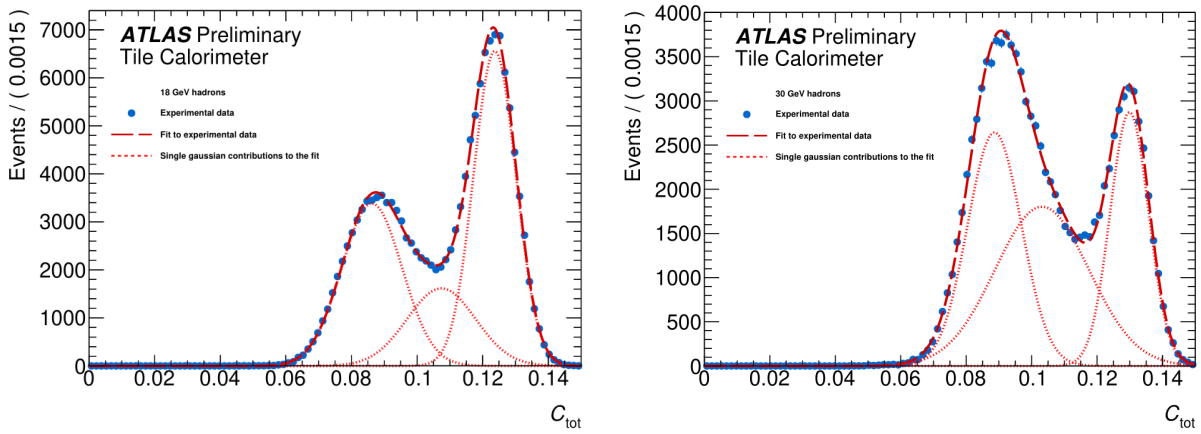

(a) (b)

Figure 4.9: The dot histograms (a) and (b) represent the C_{tot} distributions of e/π sample events with E_{beam} equal to 18 GeV and 30 GeV respectively. The events were selected requiring $C_{\text{long}} \geq 0.6$. Tree Gaussian fit functions (red dashed curves), are overlapped to the histograms (a) and (b). The functions parameters were obtained using the method maximum likelihood. Red dot curves show the individual Gaussian function contributions. In each histogram, the function with the largest value of the mean μ describes the electron contamination (Abdallah et al., 2021).

4.2.4 Pion, Kaon and Proton identification

The third set of selection criteria was specific to the type of hadronic particles being studied. For each E_{beam} data set the number of pions was estimated by subtracting the number of electron events obtained using the method described in Section 4.2.3 from the number of events of the corresponding e/π sample (Abdallah et al., 2021). The Ch2 signal measurements allow a separation of kaons and protons in the K/p samples. The scatter plots of the Ch2 signals, S_{Ch2}, in ADC counts units vs the energy measured in the calorimeter, E^{raw}, obtained by analyzing

data produced by particle beams with energies equal to 18 and 30 GeV, are shown in Figure 4.10. The S_{Ch2} selection values in ADC count units are shown in Figure 4.10 with red horizontal lines, detailed values and obtained numbers of kaons and protons can be found in Ref. (Abdallah et al., 2021).

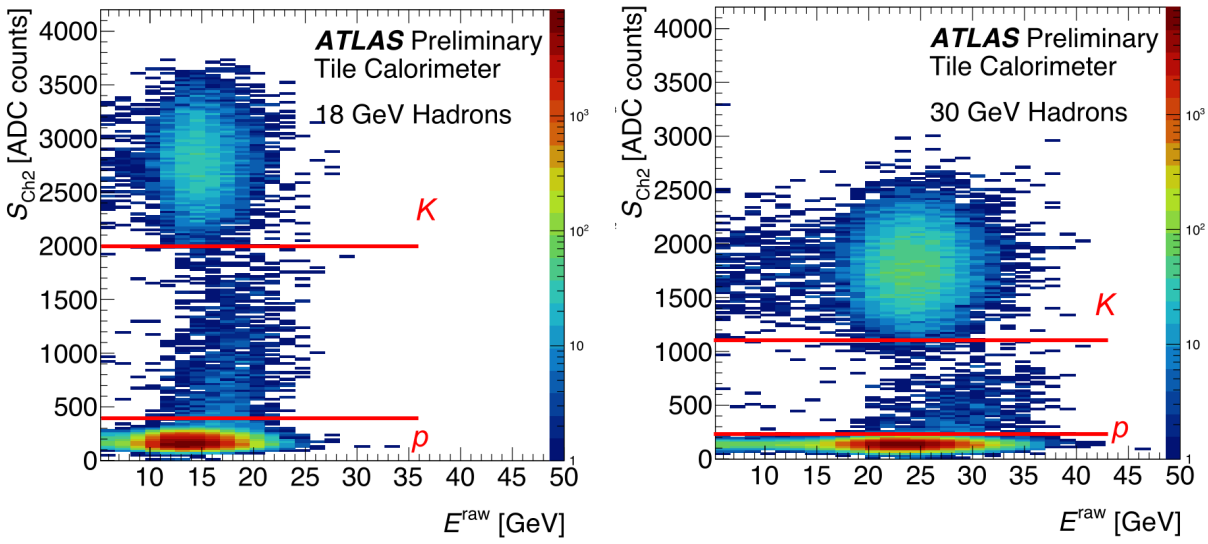

(a) (b)

Figure 4.10: Scatter plot of the Ch2 signals, S_{Ch2}, in ADC counts units, vs the energy measured in the calorimeter, E^{raw} obtained analyzing K/p sample events produced by particle beams with energy equal to 18 (a) and 30 (b) GeV. The selection criteria applied in the analysis to select kaon and proton events are shown with red horizontal lines (Abdallah et al., 2021).

4.3 Reconstruction of the energy

As already discussed in Section 4.2, the energy deposited by incident particles in the detector E^{raw} was obtained as the sum of the energy measured in the calorimeter cells. In this study only cells with $|E_{\text{c}}^{\text{raw}}| > 2\sigma$ noise were considered in the sum. For each run, the cell electronics noise σ noise was determined using random events collected between beam bursts (Pedestal Triggers). Typical noise values are of the order of 30 MeV.

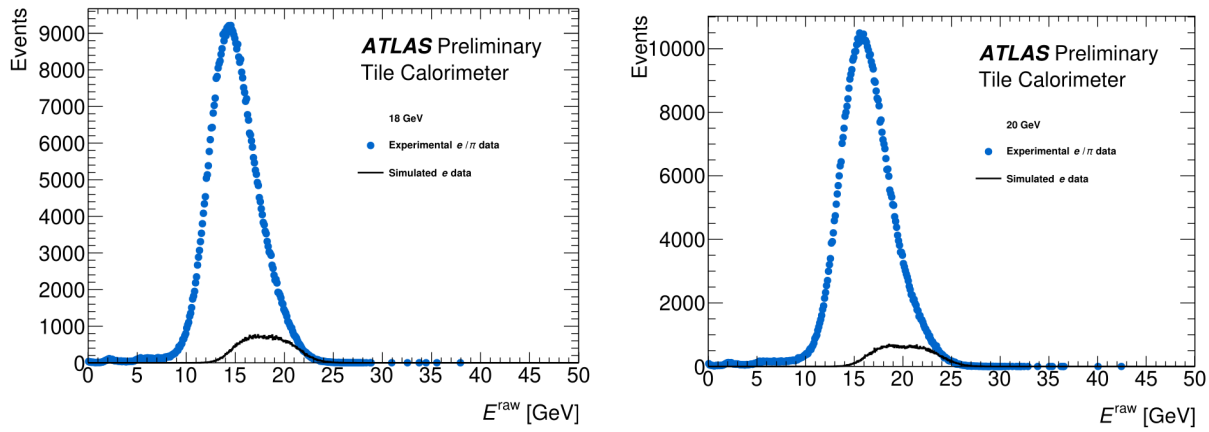

(a) (b)

Figure 4.11: Distributions of the reconstructed energy E^{raw} of the e/π samples events with E_{beam} equal to 18 GeV (a) and 20 GeV (b). The blue dot histograms correspond to the experimental data. The black histograms correspond to the expected distributions of the electrons contaminating the samples obtained using simulated events (Abdallah et al., 2021).

As sketched in Figure 4.11, the pion energy distributions $n_\pi(E^{\text{raw}})$ were obtained using, bin per bin, the formula

$$n_\pi(E^{\text{raw}}) = n_{e/\pi}(E^{\text{raw}}) - N_e f_e(E^{\text{raw}}) \tag{4.7}$$

where $n_{e/\pi}(E^{\text{raw}})$ is the number of e/π events in the considered E^{raw} bin, the electron distribution $f_e(E^{\text{raw}})$ is normalized to 1 and the number of electrons, N_e, was determined using the procedure described in Section 4.2.3. Simulated electron distributions were used in the analysis because experimental data are available only for electron beam energy equal to 20 GeV.

Figure 4.12 show the E^{raw} distributions obtained in the case of beams of pions, kaons and protons with energy equal to 18 GeV.

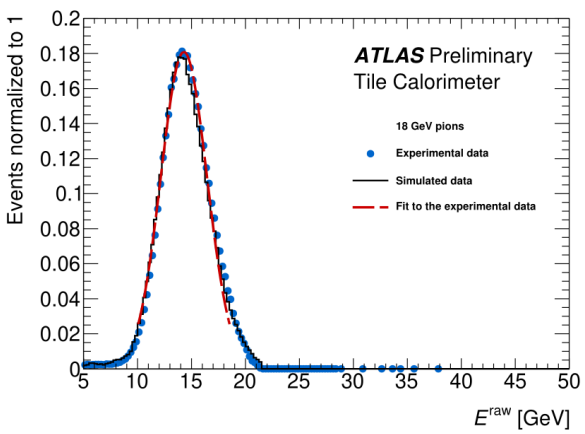

(a)

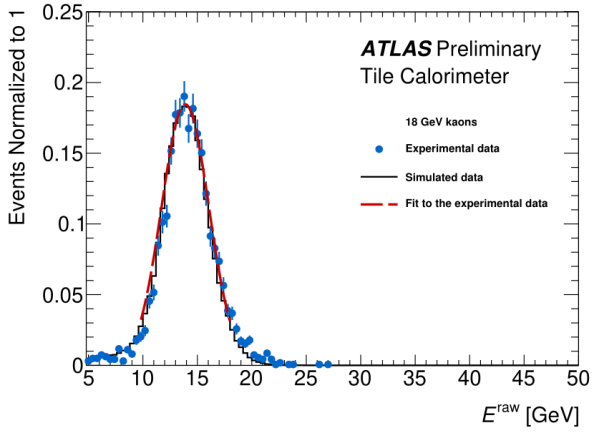

(b)

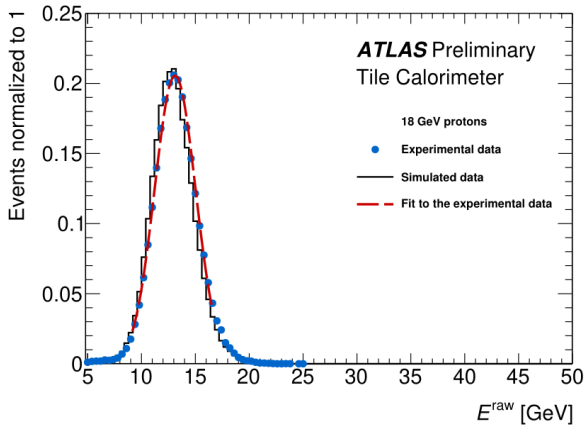

(c)

Figure 4.12: Distributions of the reconstructed energy E^{raw} obtained analyzing pion (a), kaon (b) and proton (c) data with $E_{\text{beam}} = 18$ GeV. The blue dot histograms represent the experimental data. Only statistical uncertainties are shown. The dashed curves in red correspond to the fit of a Gaussian function to the experimental data in a region $\pm 2\sigma$ around the peak value. The black histograms correspond to the predictions of the MC simulation (Abdallah et al., 2021).

The experimental results obtained using positive pions and kaons and protons beams, with energies in the range 16–30 GeV, were compared to the predictions of the Geant4-based ATLAS simulation program (Agostinelli et al., 2003). The FTFP_BERT_ATL hadronic showering model (Bertini & Guthrie, 1971) was used in the simulation. This is the model presently being used in the simulation of the ATLAS events collected during the LHC Run 1 and Run 2. For pion, kaon and proton, for each beam energy value 300k events were generated. The responses of the beam counters and Cherenkov counters were not included in the event simulation. The distributions of the transverse beam impact point coordinates in the detector were tuned to re-

produce the ones measured using the BC1. The TB detector material and geometry were fully described (Allison et al., 2006).

4.4 Determination of the energy response and resolution

The experimental and simulated E^{raw} distributions of pions, kaons and protons are described reasonably well by Gaussian function around the peak values (see Figure 4.12). As in Ref. (Adragna et al., 2009), the μ and σ parameters of Gaussian functions fitting the distributions in a region $\pm 2\sigma$ around the peak values were used to estimate the measurement responses $\langle E^{\text{raw}} \rangle$ and resolutions σ^{raw}. An iterative procedure has been applied in order to get stable values of the parameters. The method of the least squares has been used. The fit functions are superimposed to the data distributions in Figure 4.12. Energy response normalized to incident beam energy

$$R^{\langle E^{\text{raw}} \rangle} = \frac{\langle E^{\text{raw}} \rangle}{E_{\text{beam}}} \tag{4.8}$$

and energy resolution normalized to incident beam energy

$$R^{\sigma^{\text{raw}}} = \frac{\sigma^{\text{raw}}}{E_{\text{beam}}} \tag{4.9}$$

are plotted in Figures 4.13 and 4.14, respectively, as a function of E_{beam} and $1/\sqrt{E}_{\text{beam}}$. In the case of experimental results, statistical and systematic uncertainties are combined in quadrature. In the case of simulated results only statistical uncertainty is shown.

The seven sources contributed to systematical uncertainties of $R^{\langle E^{\text{raw}} \rangle}$ and $R^{\sigma^{\text{raw}}}$ (full details on systematic studies can be found in Ref. (Abdallah et al., 2021)):

1. Systematic uncertainty 1 affects only pion determinations. It corresponds to the statistical uncertainty on the determination of the number of electrons contaminating the e/π samples, discussed in section 4.2.3.

2. The electron contamination was determined studying the C_{tot} distributions of the e/π sample events with $C_{\text{long}} \geq C_{\text{long}}^{\text{min}}$ = 0.6. As systematic uncertainty was taken half of the differences of the determinations of $R^{\langle E^{\text{raw}} \rangle}$ and $R^{\sigma^{\text{raw}}}$ obtained using $C_{\text{long}}^{\text{min}}$=0.5 and $C_{\text{long}}^{\text{min}}$=0.7 respectively.

3. Effects due to the miss-modeling of the C_{tot} distributions used to determine the number of electrons contaminating the e/π samples was estimated comparing the results obtained using three Gaussian functions fits with the ones obtained using two Gaussian functions fits. Systematic Uncertainty 3 values are affecting only pion determinations and is equal to the differences of the values of $R^{\langle E^{\text{raw}}\rangle}$ and $R^{\sigma^{\text{raw}}}$ obtained using the two fitting functions.

4. The effects of the uncertainty on the distribution of the z coordinates of the electron impact point on the determinations of $R^{\langle E^{\text{raw}}\rangle}$ and $R^{\sigma^{\text{raw}}}$ was estimated using the E^{raw} distributions of the events with a z value corresponding to $E^{\text{raw}} > p_0$, "high energy events", and $E^{\text{raw}} < p_0$, "low energy events", were p_0 corresponds to the electron mean energy determined using the simulation. Source 4 systematic uncertainty values are derived from half of the differences of the values obtained using these two distributions. This uncertainty affects only pion determinations.

5. The 30 GeV scatter plot S_{Ch1} vs. S_{Ch3} in Figure 4.3 shows two spots in the K/p region. Their origin is not clear. Systematic uncertainty 5 values correspond to the differences of the $R^{\langle E^{\text{raw}}\rangle}$ and $R^{\sigma^{\text{raw}}}$ values obtained using the events with $S_{\text{Ch1}} \leq 400$ [ADC counts] and $S_{\text{Ch1}} \leq 250$ [ADC counts], respectively.

6. As it appears in Figure 4.10, proton S_{Ch2} distributions show large tails. Their origin is not understood. Systematic Uncertainty 6 values correspond to the differences of the values of $R^{\langle E^{\text{raw}}\rangle}$ and $R^{\sigma^{\text{raw}}}$ obtained by selecting the events with $S_{Ch2} \leq [200, 500]$ ADC counts, and the ones obtained selecting the events with $S_{Ch2} \leq 2000$ ADC counts at 16 GeV, 18 GeV and 20 GeV and 1000 ADC counts at 30 GeV respectively. The same effect could also be present in the case of kaons. Since they produce a signal in Ch2, the effect may not be visible. For this reason the systematic uncertainty obtained for protons is also applied in kaon determinations.

7. The effect of the uncertainty on the scale of the reconstructed cell energy $\Delta C_{\text{c}}^{\text{EM}}$ on the measurements was also investigated. An estimation of the uncertainty on the energy response can be obtained using the formula:

$$\Delta\langle E^{\text{raw}}\rangle^{\text{EM}} = \Delta C_c^{\text{EM}} \sqrt{\sum_i \langle E^{\text{raw}}\rangle_i^2} \tag{4.10}$$

where ΔC_c^{EM} is equal to 2.4% (see Section 3.5) and $\langle E^{\mathrm{raw}} \rangle_i$ is the average energy deposited in the cell i. Energies of the beam are known at few per mile precision and one obtains the values of $\Delta R^{\langle E^{\mathrm{raw}} \rangle}$ directly from the Equation 4.10. No significant dependence of the values on the beam energies was found. The uncertainty on C_c^{EM} affects in a negligible way the determinations of $R^{\sigma^{\mathrm{raw}}}$.

The effects of each of the seven considered sources of systematic uncertainties on the four energy determinations are correlated. In the study, correlation coefficient values equal to +1 were used. The total systematic uncertainties were obtained by combining in quadrature the effects of the seven sources.

Eleven (Nine) determinations of the twelve energy responses (resolutions) normalized to incident beam energy have a total uncertainty smaller than 1.4% (1.9%). It is mainly defined by the uncertainty in the calibration of the energy response of the relatively small part of the calorimeter involved in the study. In the case of kaons with E_{beam} = 16 GeV, due to the large statistical error, the uncertainty on the determination of $R^{\langle E^{\mathrm{raw}} \rangle}$, is equal to 2.4%. The uncertainty values of the determinations of $R^{\langle \sigma^{\mathrm{raw}} \rangle}$ obtained in the case of 16 GeV pion and kaon and 18 GeV kaon beams are equal to 3.1%, 20.3% and 10.4% respectively.

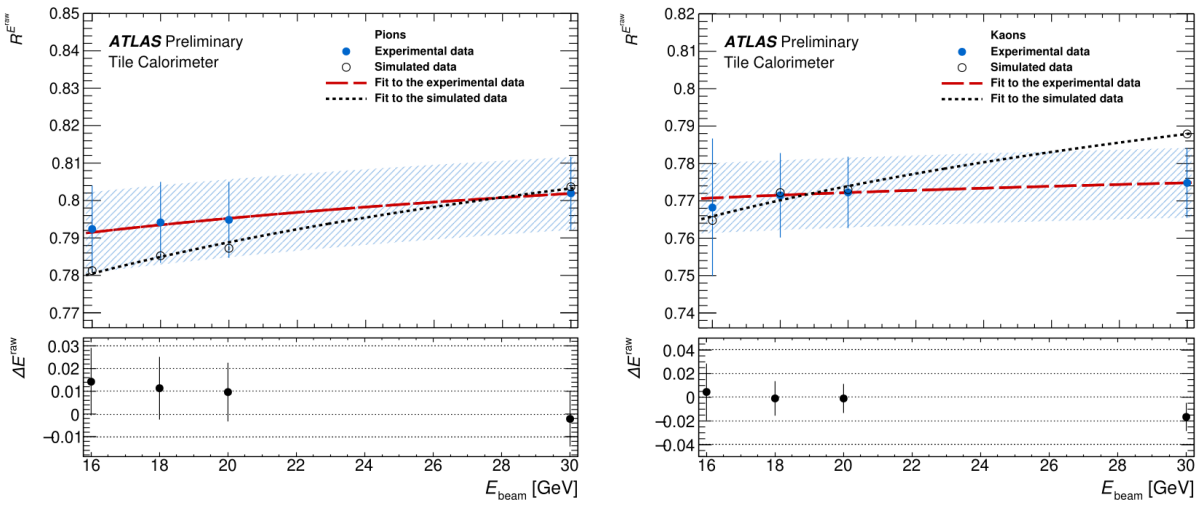

(a)

(b)

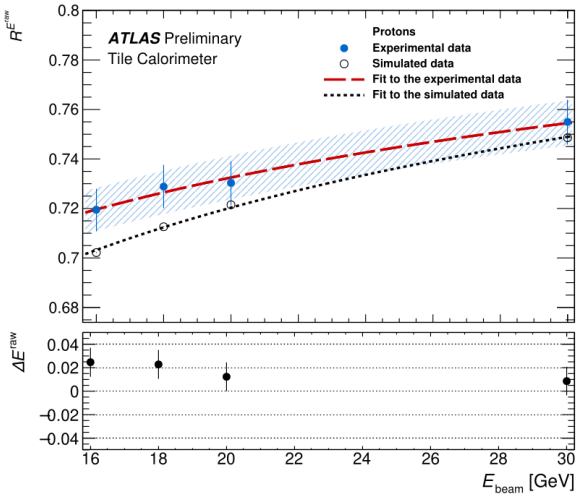

(c)

Figure 4.13: Energy response normalized to incident beam energy, $R^{\langle E^{\text{raw}} \rangle}$, measured (blue dots) and predicted by MC simulation (black circles) as a function of beam energy obtained in the case of pion (a), kaon (b) and proton (c) beams. The experimental uncertainties include statistical and systematic effects combined in quadrature. Simulated results show only statistical uncertainty. The red dashed (black dot) curves are fits of the Equation (4.13) to the experimental (simulated) data points. In case of experimental determinations the dashed blue strips display the correlated systematic uncertainties. In the bottom of the histograms are shown the fractional differences $\Delta\langle E^{\text{raw}} \rangle$ defined in Equation (4.16). The uncertainties include statistical and systematic effects combined in quadrature (Abdallah et al., 2021).

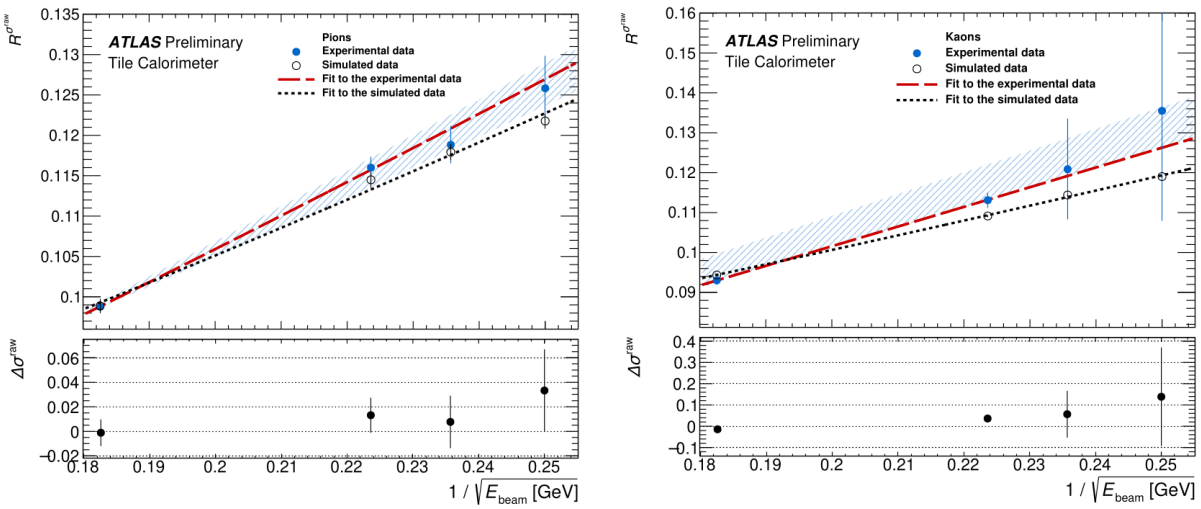

(a)

(b)

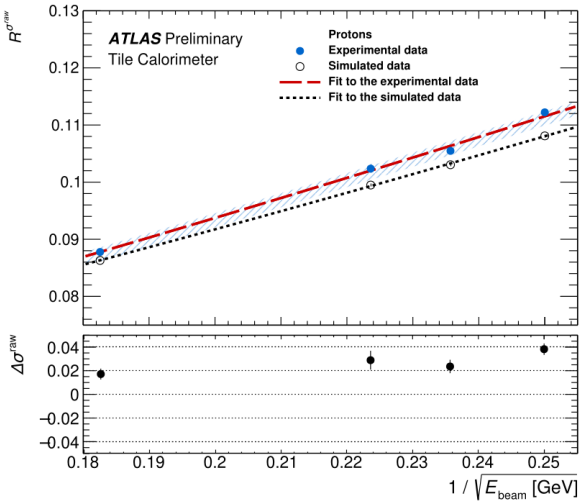

(c)

Figure 4.14: Energy resolution normalized to incident beam energy, $R^{\sigma^{\text{raw}}}$ measured (blue dots) and predicted by MC simulation (black circles) as a function of $1/\sqrt{E_{\text{beam}}}$ obtained in the case of pion (a), kaon (b) and proton (c) beams. The experimental uncertainties include statistical and systematic effects combined in quadrature. Simulated results show only statistical uncertainty. The red dashed (black dot) curves are fits of the Equation (4.15) to the experimental (simulated) data points. In case of experimental determinations the dashed blue strips display the correlated systematic uncertainties. In the bottom of the histograms are shown the fractional differences $\Delta\sigma^{\text{raw}}$ defined in Equation (4.17). The uncertainty includes statistical and systematic effects combined in quadrature (Abdallah et al., 2021).

The calorimeter response for pions, kaons and protons can be described in terms of the

calorimeter non-compensation and leading particle effects (Wigmans, 2000). The hadron energy response normalized to incident beam energy as a function of the beam energy can be parametrized according to

$$R^{\langle E^{\text{raw}}\rangle} = (1 - F_h) + F_h \times (\frac{e}{h})^{-1} \tag{4.11}$$

where F_h represents the non-electromagnetic energy component of showers induced by incident hadrons of energy E_{beam} and e/h is the ratio between the responses to the purely EM and hadronic components of showers.

In Groom's parametrization (Gabriel, Groom, Job, Mokhov, & Stevenson, 1994; Wigmans, 2000; Groom, 2008), one has

$$F_h = (\frac{E_{\text{beam}}}{E_0})^{m-1} \tag{4.12}$$

where the quantity E_0 is the energy at which multiple pion production becomes significant and the parameter m describes the relation between the average multiplicity of secondary particles produced in the collision and the fraction of energy going into π^0s in one collision. One obtains:

$$R^{\langle E^{\text{raw}}\rangle} = 1 + \frac{1}{(E_0)^{m-1}}[(\frac{e}{h})^{-1} - 1](E_{\text{beam}})^{m-1} \tag{4.13}$$

Fits of Equation 4.13 to the determined values of $R^{\langle E^{\text{raw}}\rangle}$ as a function of E_{beam} (Figure 4.14) allows for the determination of m and

$$A = \frac{1}{(E_0)^{m-1}}[(\frac{e}{h})^{-1} - 1]. \tag{4.14}$$

Parameters A and m were determined by the fit procedure.

The resolution of the energy measurements as a function of the beam energy E_{beam} can be parametrized according to the formula:

$$R^{\sigma^{\text{raw}}} = \frac{a}{\sqrt{E_{\text{beam}}}} \oplus b \tag{4.15}$$

where a is the stochastic term, the constant term b describes the non-uniformity of the cell response and the symbol $\oplus$ indicates the sum in quadrature. Parameters a and b were determined by the fit procedure.

The resulting fits to the experimental and simulated determinations are overlapped in Figures 4.13 and 4.14 that shows that Equation 4.13 and Equation 4.15 correctly describes obtained results for both Data and MC.

Based on the results obtained, one can conclude, that with the increase of the hadrons energy, the precision of the energy, measured by the detector, increases as well (Figure 4.13), and the resolution of the detector improves (Figure 4.14).

Current measurements are consistent with the results obtained in Ref. (Adragna et al., 2009).

4.5 Comparison between experimental and simulated results

A quantitative comparison between experimental and simulated results can be obtained using the quantities

$$\Delta\langle E^{\text{raw}}\rangle = \frac{\langle E^{\text{raw}}\rangle}{\langle E^{\text{raw}}_{\text{MC}}\rangle} - 1 \tag{4.16}$$

and

$$\Delta\sigma^{\text{raw}} = \frac{\sigma^{\text{raw}}}{\sigma^{\text{raw}}_{\text{MC}}} - 1 \tag{4.17}$$

The results are also shown on the bottom of Figures 4.13 and 4.14 where statistical and systematic uncertainties are combined in quadrature.

Determinations of all the energy responses and of the pion and kaon energy resolutions obtained using experimental and simulated data agree within the uncertainties. The average of the absolute values of the differences of all the energy response measurements was found to be 1.1% with an average total uncertainty of 1.4%. The average difference of all the resolution measurements was found to be 3.4%, with the average total uncertainty for pions and kaons of 5.6% and for protons of 0.6%.

Numerical values of the results are reported in Table4.2

E_{beam}	$R^{\langle E^{\text{raw}}\rangle}(\pi)$		$R^{\sigma^{\text{raw}}}(\pi)$	
[GeV]	Exp. Data	Sim. Data	Exp. Data	Sim. Data
16	$0.7924 \pm 0.0005 \pm 0.0116$	0.7812 ± 0.0005	$0.1258 \pm 0.0009 \pm 0.0038$	0.1217 ± 0.0009
18	$0.7941 \pm 0.0004 \pm 0.0108$	0.7852 ± 0.0005	$0.1188 \pm 0.0007 \pm 0.0022$	0.1179 ± 0.0009
20	$0.7948 \pm 0.0002 \pm 0.0101$	0.7872 ± 0.0005	$0.1159 \pm 0.0002 \pm 0.0013$	0.1144 ± 0.0010
30	$0.8019 \pm 0.0001 \pm 0.0098$	0.8036 ± 0.0004	$0.0987 \pm 0.0001 \pm 0.0006$	0.0988 ± 0.0008
E_{beam}	$R^{\langle E^{\text{raw}}\rangle}(K)$		$R^{\sigma^{\text{raw}}}(K)$	
[GeV]	Exp. Data	Sim. Data	Exp. Data	Sim. Data
16	$0.7682 \pm 0.0158 \pm 0.0094$	0.7647 ± 0.0003	$0.1356 \pm 0.0276 \pm 0.000007$	0.1190 ± 0.0003
18	$0.7714 \pm 0.0064 \pm 0.0093$	0.7721 ± 0.0003	$0.1209 \pm 0.0126 \pm 0.0005$	0.1144 ± 0.0002
20	$0.7723 \pm 0.0017 \pm 0.0093$	0.7729 ± 0.0002	$0.1131 \pm 0.0017 \pm 0.0008$	0.1091 ± 0.0002
30	$0.7748 \pm 0.0012 \pm 0.0093$	0.7878 ± 0.0002	$0.0930 \pm 0.0012 \pm 0.0002$	0.0943 ± 0.0002
E_{beam}	$R^{\langle E^{\text{raw}}\rangle}(p)$		$R^{\sigma^{\text{raw}}}(p)$	
[GeV]	Exp. Data	Sim. Data	Exp. Data	Sim. Data
16	$0.7195 \pm 0.0005 \pm 0.0086$	0.7021 ± 0.0002	$0.1122 \pm 0.0004 \pm 0.000034$	0.1081 ± 0.0002
18	$0.7288 \pm 0.0004 \pm 0.0087$	0.7126 ± 0.0002	$0.1055 \pm 0.0003 \pm 0.0004$	0.1030 ± 0.0002
20	$0.7303 \pm 0.0003 \pm 0.0088$	0.7214 ± 0.0002	$0.1024 \pm 0.0003 \pm 0.0007$	0.0994 ± 0.0002
30	$0.7549 \pm 0.0003 \pm 0.0091$	0.7485 ± 0.0001	$0.0877 \pm 0.0003 \pm 0.0002$	0.0862 ± 0.0001

Table 4.2: Measured energy response (resolution) normalized to incident beam energy obtained using pions ($R^{\langle E^{\text{raw}}\rangle}(\pi)$ and ($R^{\sigma^{\text{raw}}}(\pi)$)), kaons ($R^{\langle E^{\text{raw}}\rangle}(K)$ and ($R^{\sigma^{\text{raw}}}(K)$)) and protons ($R^{\langle E^{\text{raw}}\rangle}(p)$ and ($R^{\sigma^{\text{raw}}}(p)$)) of different beam energy obtained analyzing experimental and simulated data. In the case of experimental data, statistical and systematic uncertainties are reported. The effects of the different sources of systematic sources discussed in the text were combined in quadrature. Only statistical uncertainties are reported in the case of simulated data.

4.6 Summary

The results of hadrons were obtained exposing three modules of the ATLAS Tile Calorimeter to positive pion and kaon and proton beams with energies equal to 16, 18, 20 and 30 GeV and incident at the centre of the front face of a calorimeter module cell with an angle of 14 degrees from the normal. Two Cherenkov counters in the beam line made it possible to identify pions, kaons and protons. The effects of electrons contaminating the pion samples in reconstructing the pion energy were determined by exploiting the difference of electromagnetic and hadronic shower profiles in the detector.

The main purpose of the study is to compare the measured energy of the particles with the predictions of the Geant4-based simulation program used in ATLAS to simulated jets produced in proton-proton collisions at the Large Hadron Collider.

Eleven (Nine) determinations of the twelve energy responses - $R^{\langle E^{\text{raw}}\rangle}$ (resolutions - $R^{\langle \sigma^{\text{raw}}\rangle}$) normalized to incident beam energy have a total uncertainty smaller than 1.4% (1.9%). In the case of kaons with E_{beam} = 16 GeV, due to the large statistical error, the uncertainty on the determination of $R^{\langle E^{\text{raw}}\rangle}$, is equal to 2.4%. The uncertainty values of the determinations of $R^{\langle \sigma^{\text{raw}}\rangle}$ obtained in the case of 16 GeV pion and kaon and 18 GeV kaon beams are equal to 3.1%, 20.3% and 10.4% respectively.

Determinations of all the energy responses and of the pion and kaon energy resolutions obtained using experimental and simulated data agree within the uncertainties. The average of the absolute values of the difference of all the energy response (resolution) measurements was found to be 1.1% (3.4%). In the case of the response determinations and the resolution determinations of pions and kaons, the differences are consistent within the uncertainties. The uncertainties of the proton resolution determinations are about one order of magnitude smaller.

Fitting the dependance of $R^{\langle E^{\text{raw}}\rangle}$ and $R^{\sigma^{\text{raw}}}$ on the beam energy shows that standard parametrization correctly describes obtained results for both Data and MC.

Based on the results obtained, one can conclude, that with the increase of the hadrons energy, the precision of the energy, measured by the detector, increases as well, and the resolution of the detector improves.

Current measurements are consistent with the results obtained in Ref. (Adragna et al., 2009).

Chapter 5

J/ψ and $\psi(2S)$ production study

Studies involving heavy quarkonia provide a unique insight into the nature of Quantum Chromodynamics (QCD) near the boundary of perturbative and non-perturbative regimes. However, despite the long history, the investigation of quarkonium production in hadronic collisions still presents significant challenges to both theory and experiment.

In high energy hadronic collisions, charmonium states can be produced either from the short-lived QCD sources (referred to as 'prompt' production), or from long-lived sources such as decays of beauty hadrons (referred to as 'non-prompt' production). These can be separated experimentally by measuring the distance between the production and decay vertices of the quarkonium state. Effects of feeddown from higher charmonium states contributes to production of J/ψ mesons, whereas no significant contribution occurs for the $\psi(2S)$ meson. While the FONLL (fixed-order next-to-leading-logarithm) calculations (Cacciari, Frixione, & Nason, 2001; Cacciari et al., 2012) within the framework of perturbative QCD have been reasonably successful in describing the non-prompt contributions, a satisfactory understanding of the prompt production mechanisms is still to be achieved.

The methods developed within non-relativistic QCD (NRQCD) approach provide a framework for describing these processes, giving rise to a variety of models with variable success and different predictive power. In particular, Ref. (Bodwin, Braaten, & Lepage, 1995b) introduced a number of phenomenological parameters — long-distance matrix elements (LDMEs) — which can be extracted from the fits to the experimental data, and are hence expected to describe the cross-sections and differential spectra reasonably well (ATLAS Collaboration, 2016, 2014c; LHCb Collaboration, 2012; CMS Collaboration, 2012). But several attempts to build a universal 'library' of LDMEs to be used to describe a wider range of measurements such as po-

larisation of quarkonia (Aad et al., 2016; ALICE Collaboration, 2012; CMS Collaboration, 2013; LHCb Collaboration, 2014; ALICE Collaboration, 2018), their associated production (ATLAS Collaboration, 2014b, 2015) or the production of quarkonium in a wider range of processes, such as photo- and electro-production, have not been particularly successful (Li, Song, Zhang, & Ma, 2011; Lansberg & Lorce, 2013; Gong, Lansberg, Lorce, & Wang, 2013; Song, Ma, Li, Zhang, & Guo, 2011; Butenschoen & Kniehl, 2012). A combination of ATLAS results with the cross-section and polarisation measurements from CMS (CMS Collaboration, 2012, 2015, 2018), LHCb (LHCb Collaboration, 2012) and ALICE (ALICE Collaboration, 2014) now includes a variety of charmonium production characteristics in a wide kinematic range, thus providing a wealth of information for a new generation of theoretical models.

It is hence increasingly important to broaden the scope of comparison between theory and experiment by providing a broader variety of experimental information on quarkonium production in a wider kinematic range. ATLAS has previously measured the inclusive differential cross-section of the J/ψ production at $\sqrt{s} = 7$ and 8 TeV (ATLAS Collaboration, 2016), as well as the differential cross sections of the production of χ_c states (ATLAS Collaboration, 2014a), and ψ(2S) production in its $J/\psi\pi\pi$ decay mode (ATLAS Collaboration, 2014c). In most of these measurements ATLAS exploited a dimuon trigger with the muon p_T threshold of 4 GeV, with the high-p_T reach limited mainly by the trigger performance to about 100 GeV. This thesis describes a measurement of the J/ψ (ψ(2S)) meson production, in their dimuon decay mode, at $\sqrt{s} = 13$ TeV in the range of high transverse momenta (p_{T}) from 8 to 360 GeV (8–140 GeV), well beyond the existing measurements. This was made possible by the use of 2 different triggers. Production of J/ψ and ψ(2S) at low p_{T} , in the interval between 8 and 60 GeV is measured using the dimuon trigger '2mu4_Jpsimumu' (`HLT_2mu4_bJpsimumu_noL2`), requiring a pair of muons with p_{T} threshold of 4 GeV, which ran unprescaled throughout 2015 data taking, with integrated luminosity about 2.57 fb^{-1}, on the other hand, production of J/ψ and ψ(2S) at high p_{T}, in the interval between 60 and 360 GeV is measured using the single-muon trigger 'mu50' (`HLT_mu50`), requiring a muon with p_{T} threshold of 50 GeV, which ran unprescaled throughout Run 2 data-taking, with integrated luminosity about 139 fb^{-1}.

The measurements include the double-differential cross section of the two vector charmonium states (separately for prompt and non-prompt production mechanisms), the non-prompt fraction for each state, and the production ratios of ψ(2S) over J/ψ.

5.1 Event selection

Data for this analysis were taken during proton-proton collision runs of the LHC at $\sqrt{s} = 13$ TeV in years 2015, 2016, 2017 and 2018. Respective integrated luminosities for the chosen triggers `HLT_2mu4_bJpsimumu_noL2` and `HLT_mu50` are: 2.6 fb^{-1} and 139 fb^{-1}.

The data are processed with the `BPHY1` derivation framework, looking for loose di-muon candidates with $m_{\mu\mu}$ within the $\psi(nS)$ mass regions. Selected events are required to have a pair of oppositely charged muons.

The two ID tracks are fitted to a common vertex, with fit quality requirement of $\chi^2 < 200$ and the di-muon mass within the range $2.6 < m_{\mu\mu} < 4.2$ GeV. The decay length L_{xy} is used to calculate the pseudo-proper time

$$\tau = \frac{m}{p_T}\frac{L_{xy}}{c} \tag{5.1}$$

where m and p_T are respectively the mass and the transverse momentum of the dimuon system, and c is the speed of light. L_{xy} is defined as a projection of the vector L_{xy} pointing from the primary vertex to the ψ decay vertex in transverse plane onto the direction of ψ transverse momentum:

$$L_{xy} = \frac{\vec{L}_{xy} \cdot \vec{p_{\mathrm{T}}}}{p_{\mathrm{T}}} \tag{5.2}$$

The primary vertex is chosen as the collision vertex closest in $\Delta(z_0) = pv_z - z_0$, where z_0 is the z coordinate of the intersection of the di-muon's trajectory with the beam axis in the $z - \rho$ plane. Effects of the primary vertex smearing on the definition of rapidity bins has been found to be negligible.

Each muon is required to have transverse momentum greater than 4 GeV and $|\eta| < 2.4$. Muons are further matched to chosen trigger object(s) by requiring a spatial match of $\Delta R <$ 0.01.

A subsequent slimming of the samples is also performed on the xAOD, removing unused collections and retaining only ID tracks associated to muons.

Athena xAOD package (OniaAna) is used for the rest of the analysis, resulting in a small ntuple used for the final fits.

5.2 Choosing analysis bins

The use of `HLT_2mu4_bJpsimumu_noL2` trigger effectively means the acceptance selection "mu4 + mu4", which would allow us to start the covered p_{T} range from 8 GeV and statistics allowing

to reach beyond 60 GeV, while at high p_{T} the use of `HLT_mu50` trigger effectively means the acceptance selection "mu52.5 + mu4", which would allow us to start the covered p_{T} range from 60 GeV.

Looking at the yields of J/ψ over the years 2015-18, we are able to have the last bin covering 300-360 GeV with (just about) reasonable statistics.

The phase space is divided into bins in absolute (true) rapidity $|y|$ and onia transverse momentum p_{T}. There are 3 bins in $|y|$, with bin boundaries at 0, 0.75, 1.5, 2.0, while in p_{T} the bin boundaries are 8, 9, 10, 11, 12, 13, 14, 15, 16, 17, 18, 19, 20, 22, 24, 26, 28, 30, 35, 40, 45, 50, 55, 60, 70, 80, 90, 100, 120, 140, 160, 180, 200, 240, 300, 360 GeV (35 bins). Overall, there are 35 $\times$ 3 = 105 separate analysis bins.

In most of low p_{T} bins the event statistics are very high, and p_{T} dependence of many parameters and correction factors varies quite significantly within the bin, thus affecting fit stability. In order to reduce such effects, the fits were performed in narrower sub-bins, and the resulting yields, after all corrections, were added together to form the cross section in the full analysis bins described above. In particular, bins between 8 and 13 GeVwere split into sub-bins of 0.1 GeV, bins between 13 and 20 GeV into sub-bins of 0.2 GeV, bins between 20 and 30 GeV into sub-bins of 0.4 GeV, and the bin between 30 and 35 GeV into sub-bins of 1 GeV.

5.3 Measurement strategy

In each (p_{T}, y) bin, a 2-dimensional unbinned maximum likelihood fit is applied to the distribution of (unweighted) dilepton candidates, in invariant mass and (pseudo-proper) lifetime of the lepton pair, to obtain the raw yields $N_{\psi}^{P,NP}$, for prompt (P) and non-prompt (NP) ψ states, where $\psi = J/\psi,\ \psi(2S)$. The raw yields are then corrected for: acceptance, trigger and reconstruction efficiencies, and trigger and reconstruction correction scale factors. Each event is assigned a correction factor, defined as a product of the above-listed efficiencies and corrections. These are then averaged over the analysis (sub)bin to form the overall correction factor for this bin.

So, the prompt P and non-prompt NP double-differential production cross sections for $\psi = J/\psi,\ \psi(2S)$ are calculated as follows:

$$\frac{d^2\sigma^{P,NP}(pp \to \psi)}{dp_{\mathrm{T}}dy} \times \mathcal{B}(\psi \to \mu^+\mu^-) = \frac{1}{\mathcal{A}(\psi)\epsilon_{\mathrm{trig}}\epsilon_{\mathrm{trigSF}}\epsilon_{\mathrm{reco}}\epsilon_{\mathrm{recoSF}}} \frac{N_{\psi}^{P,NP}}{\Delta p_{\mathrm{T}}\ \Delta y\ \int \mathcal{L}dt} \tag{5.3}$$

where:

- $\mathcal{A}(\psi)$ is the geometrical acceptance (averaged over the bin) calculated separately for low p_{T} and high p_{T} bins, using the cuts:
  - in low p_{T} range: $p_{\mathrm{T}}(\mu_1) > 4$ GeV, $p_{\mathrm{T}}(\mu_2) > 4$ GeV, $|\eta(\mu_1), \eta(\mu_2)| < 2.4$
  - in high p_{T} range: $p_{\mathrm{T}}(\mu_1) > 52.5$ GeV, $p_{\mathrm{T}}(\mu_2) > 4$ GeV, $|\eta(\mu_1), \eta(\mu_2)| < 2.4$
- ϵ_{trig} is the trigger efficiency, calculated for low p_{T} and high p_{T} ranges with corresponding trigger information, using MC for J/ψ and ψ(2S).
- $\epsilon_{\mathrm{trigSF}}$ is the trigger correction scale factor accounting for MC-data differences, calculated using corresponding trigger scale factor maps.
- ϵ_{reco} is the reconstruction efficiency, calculated using the Monte Carlo samples for J/ψ and ψ(2S).
- $\epsilon_{\mathrm{recoSF}}$ is the reconstruction efficiency correction scale factor accounting for MC-data differences, calculated using corresponding reconstruction scale factor maps.
- $N_{\psi}^{\mathrm{P,NP}}$ are the raw yields of J/ψ and ψ(2S), obtained from 2D maximum likelihood fits.
- Δp_{T} and Δy are corresponding bin widths in p_{T} and absolute rapidity.
- $\int \mathcal{L}dt$ is the corresponding integrated luminosity.

Acceptance $\mathcal{A}(\psi)$ is the probability that a J/ψ with (true) momentum within the range covered by an analysis (sub)bin survives the acceptance cuts on the muon parameters. The acceptance calculation is performed using truth-level kinematic variables, with the 'bin migration' correction taken care of at the efficiency correction stage (see below).

5.3.1 Fit model

The 2-dimensional unbinned maximum likelihood fit is applied to the distribution of dilepton candidates, in invariant mass in the range between 2.7 GeVand 4.1 GeV, and in (pseudo-proper) lifetime of the lepton pair between -1 ps and 12 ps. The fit model is described by a sum of the following terms:

$$PDF(m,\tau) = \sum_{i=1}^{7} \kappa_i f_i(m) \cdot (h_i(\tau) \otimes R(\tau)) \cdot C_i(m,\tau). \tag{5.4}$$

where m is the dimuon invariant mass, while τ is the pseudo-proper lifetime of the dimuon. $R(\tau)$ in eq. (5.4) is the function describing the experimental resolution in pseudo-proper lifetime. It is parameterised as a weighted sum of three Gaussians with related widths.

Terms corresponding to $i = 1, 2$ describe the J/ψ prompt and non-prompt signal respectively; similarly, terms $3, 4$ correspond to prompt and non-prompt signal from ψ(2S). Term 5 describes the prompt background, where non-resonant di-muons are produced from the primary vertex (e.g. Drell-Yan pairs). Term 6 corresponds to the 'single-sided' non-prompt background, mainly events where the di-muon continuum is produced from a (cascade) decay of the same B hadron, while term 7 describes the part of the non-prompt continuum where the two muons are produced from different B hadrons, yielding a secondary vertex which may appear on both sides of the beamline (hence the 'double-sided' exponential).

The mass lineshape of the J/ψ (ψ(2S)) peak is parameterised as a superposition of two Gaussians $G_1^{'}(G_2^{'})$ and $G_1^{''}(G_2^{''})$ and a Crystal Ball function $B_1(B_2)$ (function similar to Gaussian, with small asymmetry on the left tail), which are the same for prompt and non-prompt components.

The lifetime distributions of prompt J/ψ and ψ(2S) are parameterised as delta-functions (smeared with the lifetime resolution $R(\tau)$).

For non-prompt J/ψ and ψ(2S) the lifetime dependence is described by a superposition of two exponential functions with linked slopes, convoluted with the resolution function $R(\tau)$.

As for the three background terms, here all non-prompt mass distributions are parameterised as exponentials, with independent parameters. Prompt background in the mass is modelled using the first three Bernstein polynomials, which are defined as

$$B_{i,n}(t) = \binom{n}{i} t^i (1-t)^{n-1} \tag{5.5}$$

where t is the mass variable linearly scaled to the fitting interval, so that $t = 0$ corresponds to $m = 2.7$ GeVand $t = 1$ corresponds to $m = 4.1$ GeV. Hence, they are always positive-definite in the fitted range. The first three polynomials are:

$$B_{0,1}(t) = 1 - t, \quad B_{1,1}(t) = t, \quad B_{0,2}(t) = (1-t)^2 \tag{5.6}$$

The lifetime distribution is a delta-function for the prompt term, a single-sided exponential for the main non-prompt term, and a symmetric double-sided exponential for the last term. Each of these are also convoluted with lifetime the resolution function $R(\tau)$.

In order to take into account possible correlations between mass m and lifetime τ of a dimuon, in eq. 5.4 in the term with $i = 1$, the simple product of two Gaussians is replaced by a bivariate normal distribution (BV), defined as:

$$BV(m,\tau) = \text{Const} * \exp\left[\frac{1}{2(1-\rho^2)}\left(\frac{(m-\mu_m)^2}{\sigma_m^2} - \frac{2\rho(m-\mu_m)(\tau-\mu_\tau)}{\sigma_m\sigma_\tau} + \frac{(\tau-\mu_\tau)^2}{\sigma_\tau^2}\right)\right] \tag{5.7}$$

where ρ is the correlation coefficient between m and τ.

These parameterisations are summarised in table 5.1.

i	Type	P/NP	$f_i(m)$	$h_i(\tau)$	$C_i(m,\tau)$
1	J/ψ	P	$\omega_0 G_1'(m) + (1-\omega_0)[\omega_1 CB_1'(m) + (1-\omega_1)G_1''(m)]$	$\delta(\tau)$	$BV(m,\tau,\rho)$
2	J/ψ	NP	$\omega_0 G_1'(m) + (1-\omega_0)[\omega_1 CB_1'(m) + (1-\omega_1)G_1''(m)]$	$\omega_2 E_1(\tau) + (1-\omega_2)E_1'(\tau)$	1
3	$\psi(2S)$	P	$\omega_0 G_2'(m) + (1-\omega_0)[\omega_1 CB_2'(m) + (1-\omega_1)G_2''(m)]$	$\delta(\tau)$	1
4	$\psi(2S)$	NP	$\omega_0 G_2'(m) + (1-\omega_0)[\omega_1 CB_2'(m) + (1-\omega_1)G_2''(m)]$	$E_2(\tau)$	1
5	Bkg	P	B	$\delta(\tau)$	1
6	Bkg	NP	$E_4(m)$	$E_5(\tau)$	1
7	Bkg	NP	$E_6(m)$	$E_7(\lvert\tau\rvert)$	1

Notation	Function
G	Gaussian
CB	Crystal Ball
E	Exponential
B	Bernstein polynomials
BV	Correlation term of the bivariate Gaussian dist.

Table 5.1: Parameterisation of the fit model. Notation is explained in the text and in the small table below.

More technical details of the fit model can be found in Appendix A.

5.3.2 Fit results

The fits are quite complex, and care must be taken to insure their stability by a careful choice of starting values of the parameters and the ranges of their variation. Some of the fit parameters were fixed to the values established during various preliminary studies, including using

the various MC samples. During systematic studies, the parameters fixed in the main fit were changed to other predetermined values, or were released altogether (see section 5.4).

Figures 5.1, 5.2 and 5.3 show the examples of the mass and lifetime projections of the fits in randomly chosen analysis (sub)bins. One-dimensional pull distributions in each dimension are also included at the bottom of the distributions.

In order to assess the quality of each fit, two-dimensional χ^2 values were calculated after the fits. The fit quality was found to be good in all (sub)bins. The table containing these values can be found in Appendix B.

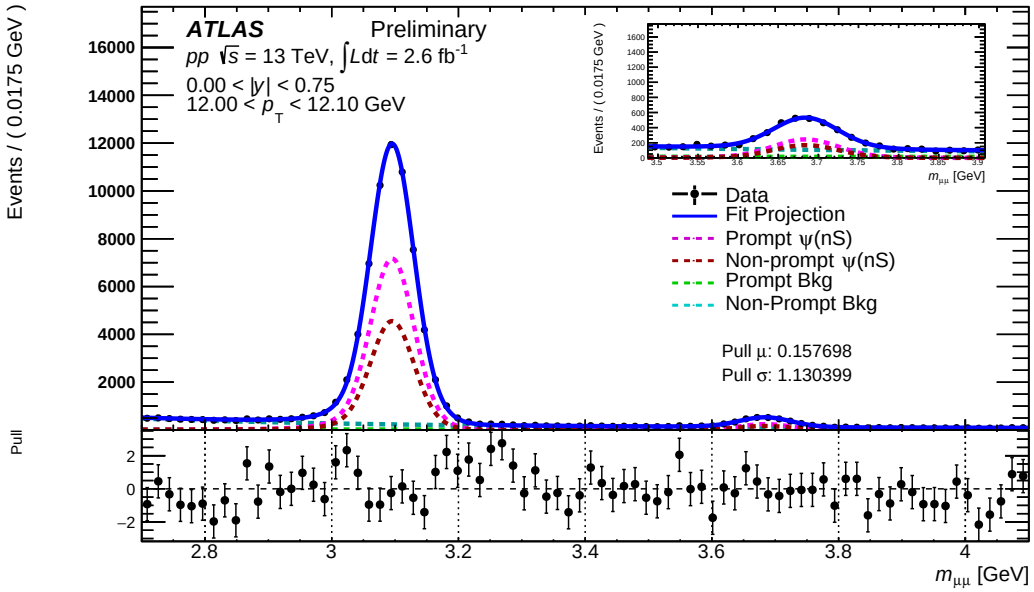

(a)

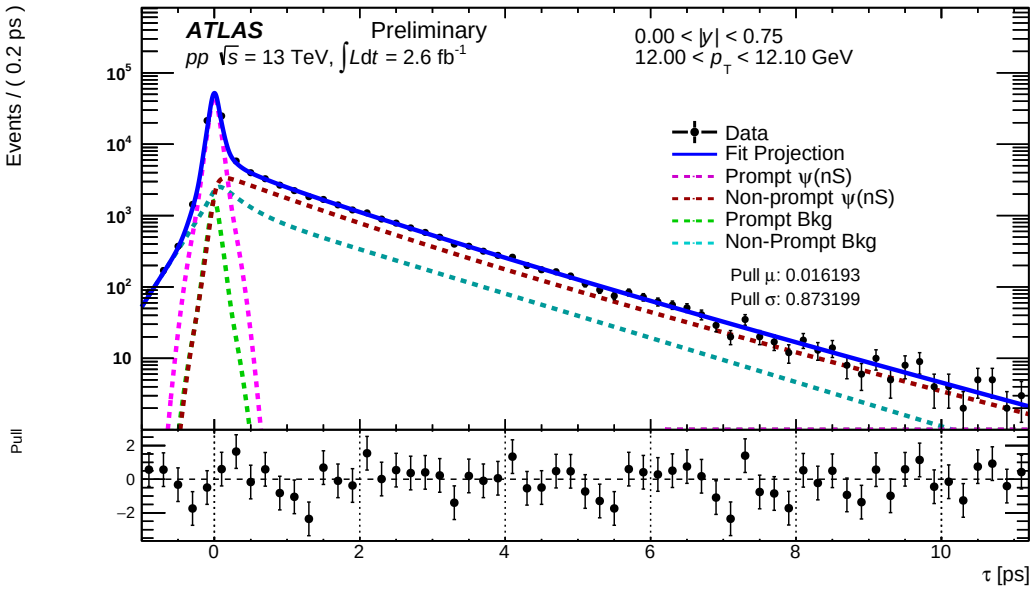

(b)

Figure 5.1: Mass (a) and lifetime (b) projections of the fit result for a randomly chosen analysis sub-bin in the first rapidity slice.

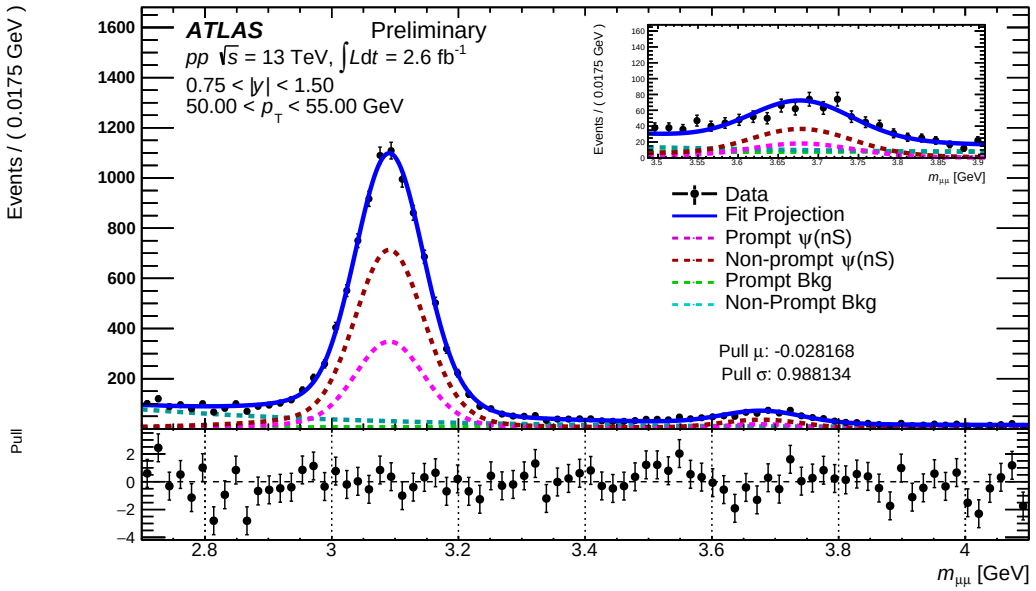

(a)

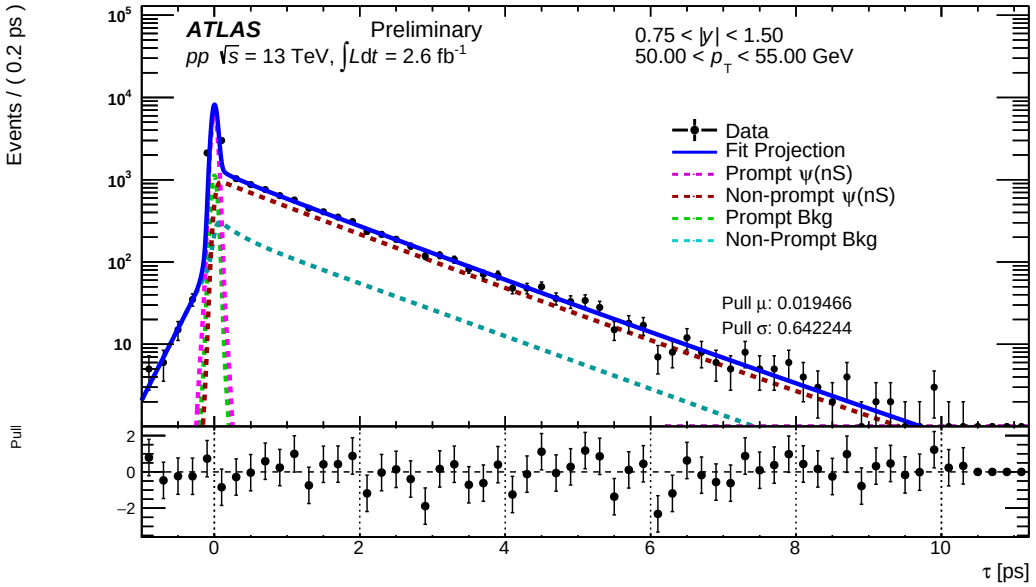

(b)

Figure 5.2: Mass (a) and lifetime (b) projections of the fit result for a randomly chosen analysis bin in the second rapidity slice.

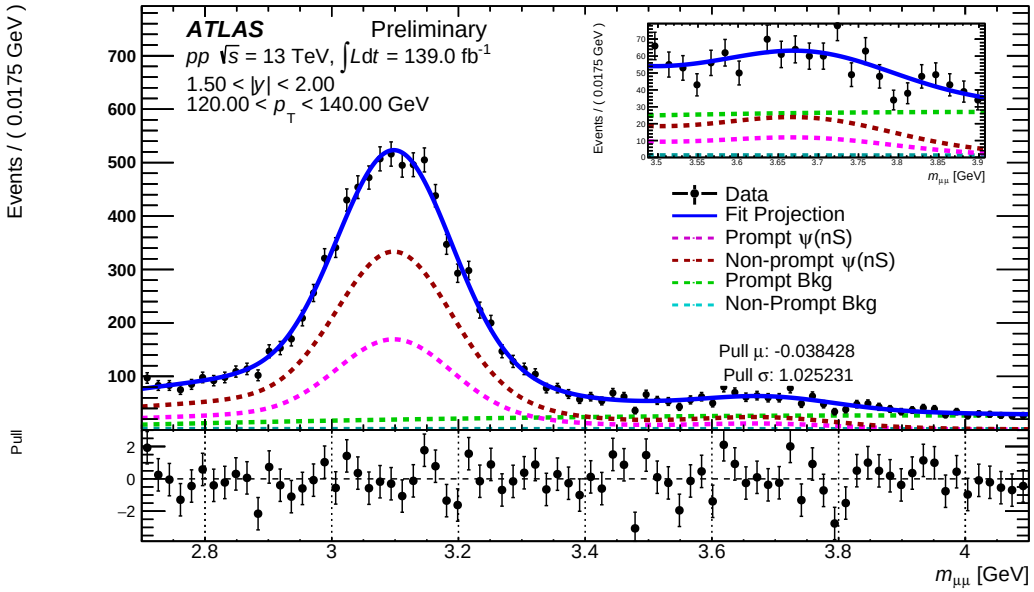

(a)

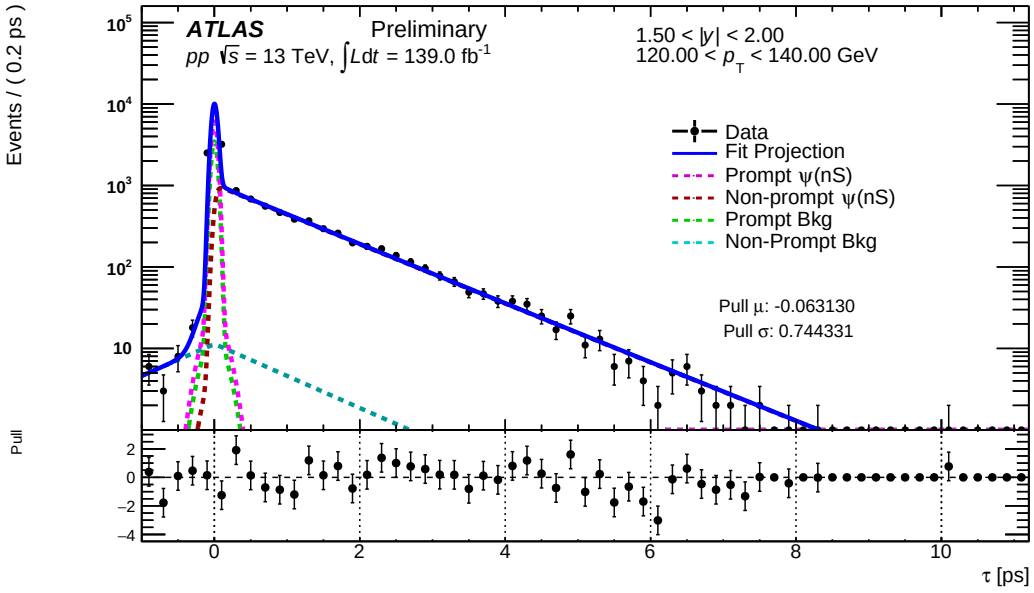

(b)

Figure 5.3: Mass (a) and lifetime (b) projections of the fit result for a randomly chosen analysis bin in the third rapidity slice.

The main parameters determined by the fit are the yields of J/ψ and $\psi(2S)$ states, and their non-prompt fractions. Separate yields for prompt and non-prompt production are then calculated, taking into account the correlations between the parameters.

The experimental resolution in pseudo-proper lifetime, $R(\tau)$, is parameterised as a nor-

malized weighted sum of three Gaussians, with $\sigma_2 = 2\sigma_1$ and $\sigma_3 = 4\sigma_1$. The fractional weights of these Gaussians are free parameters, but σ_1 is fixed to the value of 0.04 ps. Central values of all three Gaussians are fixed at zero.

Mean mass and σ of the main (narrow) J/ψ mass Gaussian are free parameters in the fit. Mean J/ψ mass is shared between the narrow Gaussian and the Crystal Ball functions, but the wider second Gausian is allowed to have a freely variable shift of the peak. The width of the second Gaussian is also allowed to float.

The fraction of the narrow Gaussian in the superposition is currently fixed at 0.75. The σ of the Crystal Ball function is a multiple of the σ of the narrow Gaussian, currently fixed at 1.45, while the remaining parameters of the Crystal Ball function, α and n, are fixed to 1.35 and 2.5, respectively.

The correlation factor ρ in eq. (5.7) is set to 0.3.

The lineshape of ψ(2S) follows the same structure, with the mean mass and σ linked to the corresponding values of J/ψ by a factor equal to the ratio of PDG masses, 1.1902.

The lifetime distribution of J/ψ is parameterised as a weighted sum of two exponentials, convoluted with the lifetime resolution function $R(\tau)$ defined above. The weights and slopes of the two exponentials are free parameters.

The lifetime distribution of ψ(2S) and slopes of the background mass exponentials are free parameters determined from the fit.

Overall normalisation of the background and relative weights of the three background terms are also free parameters and are determined from the fit.

In very high-p_{T} bins (namely, for $p_{\mathrm{T}} > 140$ GeV) the yields of ψ(2S) cannot be reliably determined, due to low statistics and worsening mass resolution. For these bins, the ψ(2S) yield was fixed at 6% of the J/ψ yield, its non-prompt fraction was fixed at 0.7, and J/ψ yields were determined as usual.

Various preliminary test fits were performed to obtain the values for the fixed parameters listed above. These values were freed or varied within pre-established limits at the stage of systematic studies.

The total yields and non-prompt fractions for J/ψ and ψ(2S), obtained from the fits, are shown in Fig. 5.4 and Fig. 5.5 respectively.

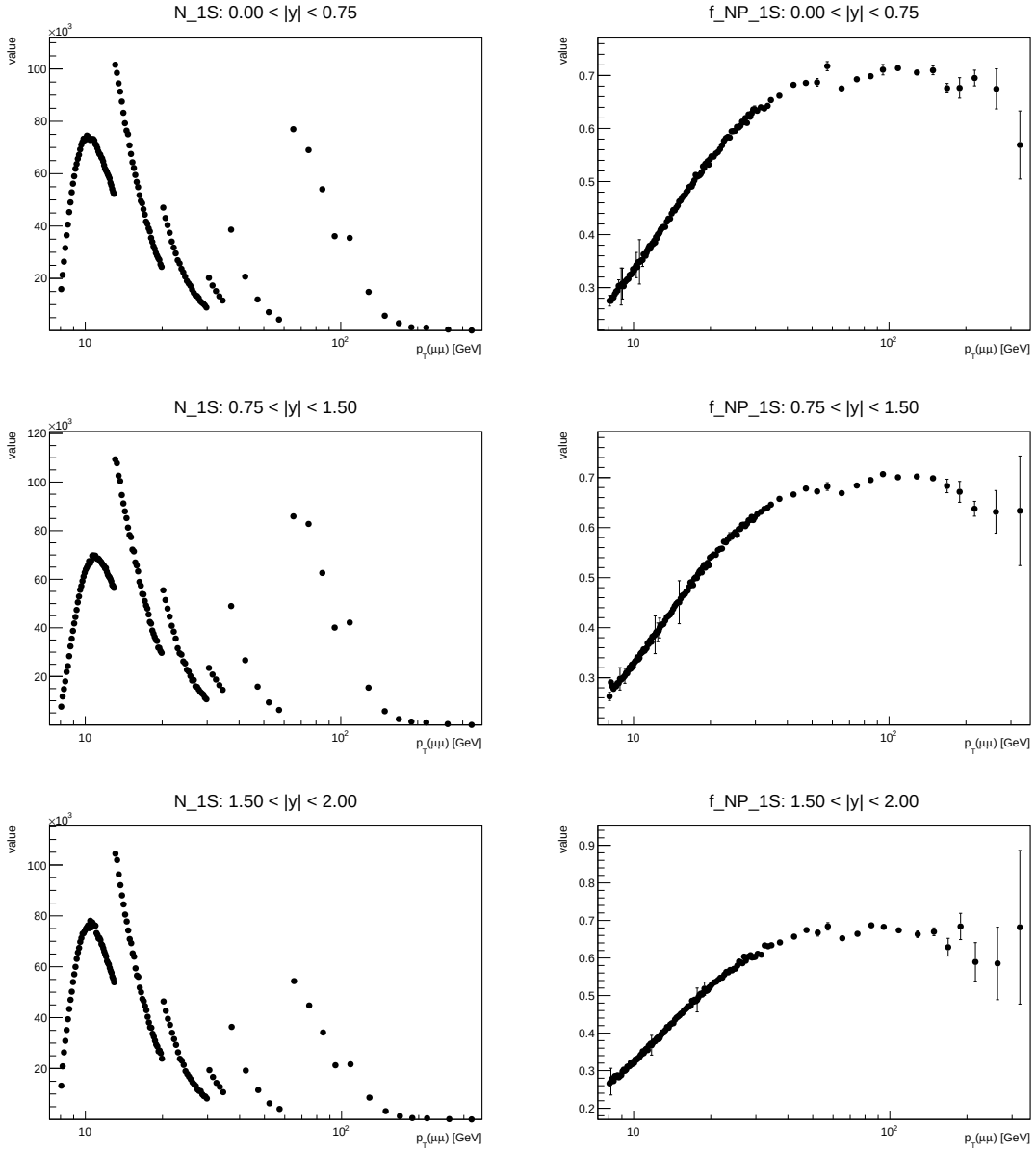

Figure 5.4: p_{T} dependence of J/ψ yield (left) and non-prompt fraction (right), in the three rapidity ranges (central to forward from top to bottom). The structures in the plots of the yields are caused by the changes in the p_{T} bin widths.

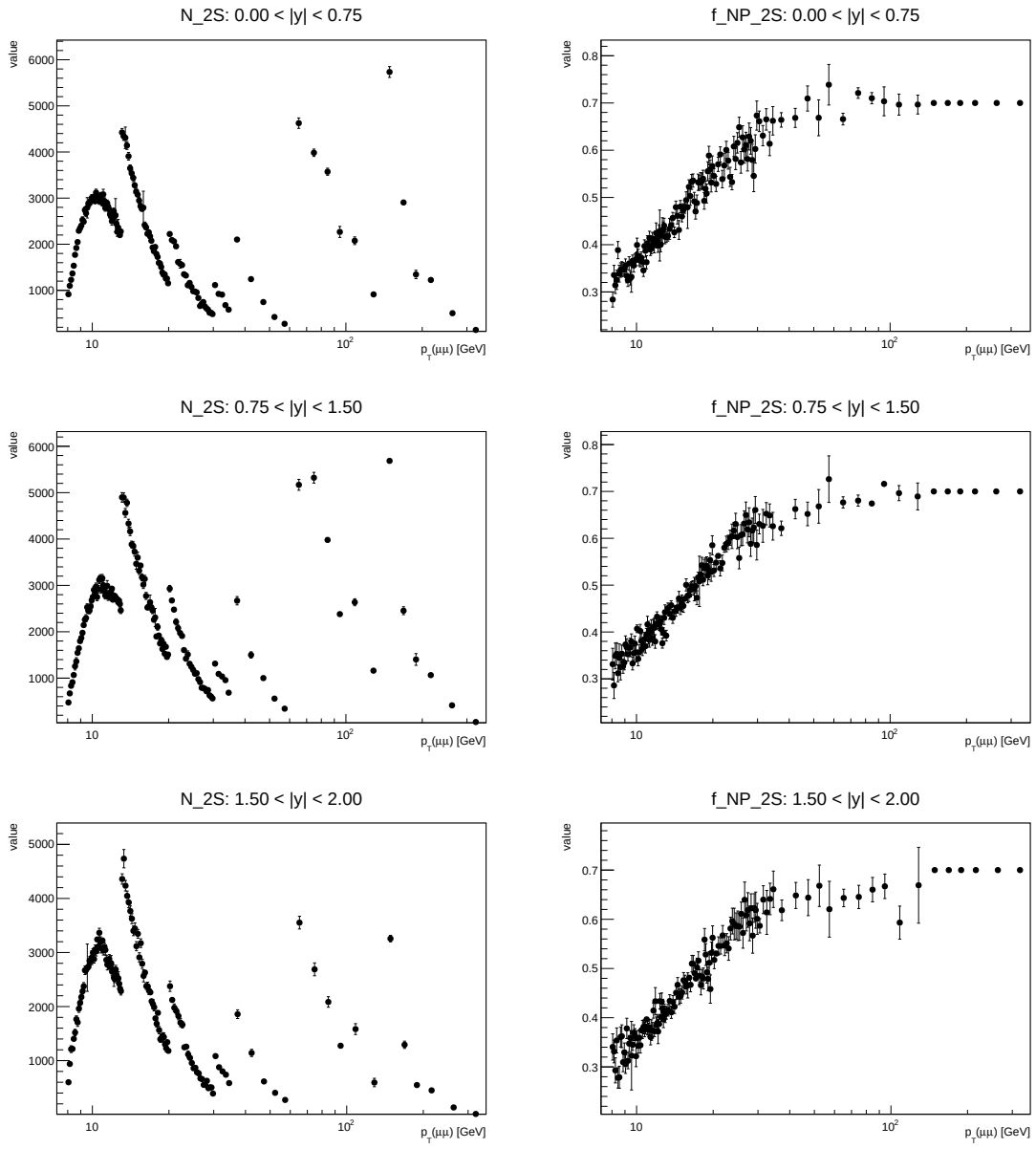

Figure 5.5: p_{T} dependence of ψ(2S) yield (left) and non-prompt fraction (right), in the three rapidity ranges (central to forward from top to bottom). The structures in the plots of the yields are caused by the changes in the p_{T} bin widths.

5.3.3 Monte Carlo simulation

Various aspects of this measurement require Monte Carlo simulations. Here is the list of MC samples used:

1. Prompt J/ψ; Event generatior: Pythia-MC; Event number: 10 M; Athena release 21.2.105
2. Non-prompt J/ψ; Event generatior: Pythia-MC; Event number: 50 M; Athena release 21.2.103
3. Prompt J/ψ; Event generator: ParticleGun-MC; Event number: 1 M; Athena release 21.2.68
4. Non-prompt J/ψ; Event generatior: ParticleGun-MC; Event number: 1 M; Athena release 21.2.68
5. Prompt ψ(2S); Event generator: ParticleGun-MC; Event number: 2 M; Athena release 21.6.83
6. Non-prompt ψ(2S); Event generator: ParticleGun-MC; Event number: 2 M; Athena release 21.6.83

Samples 1,2 naturally have p_{T} distributions close to that in real data. Particle-gun samples 3,5 were genarated with flat p_{T} distribution, and $L_{xy} = 0$. Particle-gun samples 4,6 were genarated with flat p_{T} distribution and flat L_{xy} distribution. These were either used in very narrow bins of p_{T} and/or τ, or reweighted as necessary, using simple analytical weight functions obtained from fits to data.

5.3.4 Acceptance

The kinematic acceptance $\mathcal{A}(\psi)$ for a $\psi \to \mu^+\mu^-$ decay with specific p_{T} and y is given by the probability that muons pass the fiducial selection:

- for low p_{T} range: $p_{\mathrm{T}}(\mu_1) > 4$ GeV and $p_{\mathrm{T}}(\mu_2) > 4$ GeV and $|\eta(\mu_{1,2})| < 2.4$,
- for high p_{T} range: $_{\mathrm{T}}(\mu_1) > 4$ GeV and $_{\mathrm{T}}(\mu_2) > 52.5$ or $\mu_1 \leftrightarrow \mu_2$ and $|\eta(\mu_{1,2})| < 2.4$.

This is calculated using generator-level 'accept-reject' simulations, in fine bins of true p_{T} and true rapidity y. It should be noted that the acceptance is a fast-varying function of p_{T}, especially in the threshold regions, while its dependence on y is minimal.

Acceptance is defined in the 'true' variable space, and any corrections due to true vs measured differences are taken care of as part of the efficiency corrections (see below).

In general, acceptance $\mathcal{A}$ depends on five independent variables (the two muon momenta are constrained by the $m(\mu\mu)$ mass condition), chosen as p_{T}, $|y|$, azimuthal angle ϕ of the ψ meson in the laboratory frame, and two angles characterizing the decay $\psi \to \mu^+\mu^-$, $\theta^\star$ and $\phi^\star$, described in detail in Ref. (Faccioli et al., 2010). The angle $\theta^\star$ is the angle between the direction of the positive-muon momentum in the ψ rest frame and the momentum of the ψ in the laboratory frame, while $\phi^\star$ is defined as the angle between the dimuon production and decay planes in the laboratory frame. The ψ production plane is defined by the momentum of the ψ in the laboratory frame and the positive z-axis direction. The distributions in $\theta^\star$ and $\phi^\star$ differ for various possible spin-alignment scenarios of the ψ state.

The coefficients λ_θ, λ_ϕ and $\lambda_{\theta\phi}$ in

$$\frac{\mathrm{d}^2N}{\mathrm{d}\cos\theta^\star \mathrm{d}\phi^\star} \propto 1 + \lambda_\theta \cos^2\theta^\star + \lambda_\phi \sin^2\theta^\star \cos 2\phi^\star + \lambda_{\theta\phi} \sin 2\theta^\star \cos\phi^\star \tag{5.8}$$

are related to the spin-density matrix elements of the dimuon spin wave function.

Since the polarization of the ψ state may affect acceptance, seven extreme cases that lead to the largest possible variations of acceptance within the phase space of this measurement are identified. These cases, described in Table 5.2, are used to define a range in which the results may vary under any physically allowed spin-alignment assumptions. This analysis adopts the isotropic distribution in both $\cos\theta^\star$ and $\phi^\star$ as nominal, and the variation of the results for a number of extreme spin-alignment scenarios is studied and presented as sets of correction factors.

For each of the two mass points (corresponding to the J/ψ and ψ(2S) masses), 2D maps are produced as a function of dimuon $p_{\mathrm{T}}(\mu\mu)$ and $|y(\mu\mu)|$ for the set of spin-alignment hypotheses. Each point on the map is determined from a uniform sampling over $\phi^\star$ and $\cos\theta^\star$, accepting those trials that pass the fiducial selections. To account for various spin-alignment scenarios, all trials are weighted according to Eq. 5.8. Acceptance maps are defined within the range $8 < p_{\mathrm{T}}(\mu\mu) < 400$ GeVand $|y(\mu\mu)| < 2.4$, corresponding to the data considered in the analysis. The map is defined in 8 slices in $|y(\mu\mu)|$ and 1000 bins in $p_{\mathrm{T}}(\mu\mu)$, using 100k trials for each point, resulting in sufficiently high precision, such that its statistical uncertainty can be neglected.

Table 5.2: Values of angular coefficients describing the considered spin-alignment scenarios.

	Angular coefficients		
	λ_θ	λ_ϕ	$\lambda_{\theta\phi}$
Isotropic *(central value)*	0	0	0
Longitudinal	-1	0	0
Transverse positive	$+1$	$+1$	0
Transverse zero	$+1$	0	0
Transverse negative	$+1$	-1	0
Off-(λ_θ–λ_ϕ)-plane positive	0	0	$+0.5$
Off-(λ_θ–λ_ϕ)-plane negative	0	0	-0.5

Figure 5.6 shows the 2D acceptance map for unpolarized J/ψ and ψ(2S). After the map generation, mean acceptance for every analysis (sub)bin is calculated, using data events selected from within a 6σ range of the given ψ state mass. Thus obtained acceptance is used in eq. (5.3).

For the non-prompt fraction and ratio measurements, the acceptance correction factors are determined from the appropriate ratios of the individual correction factors.

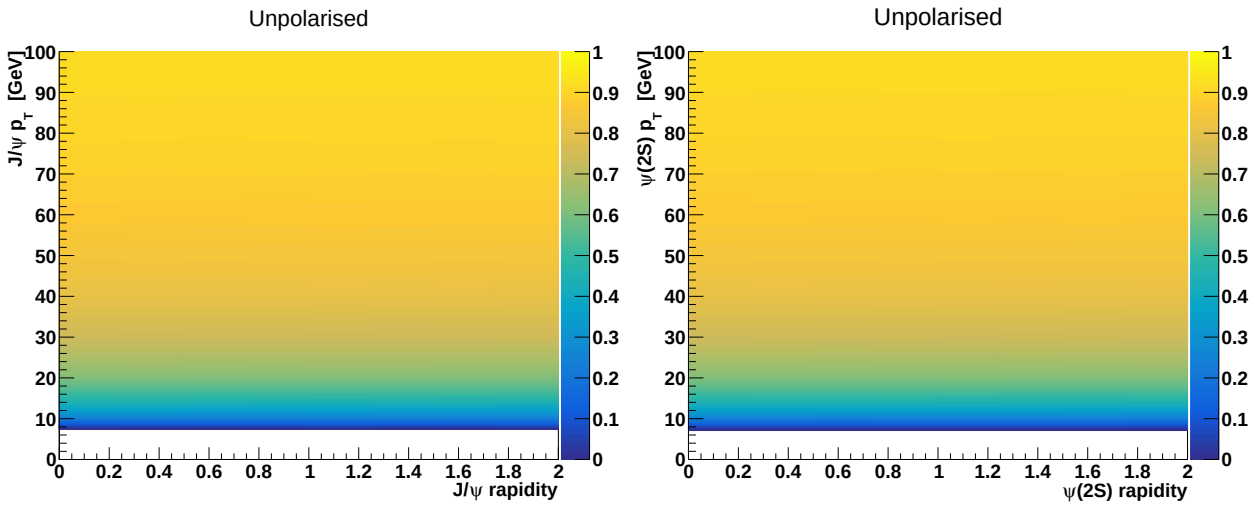

(a) (b)

Figure 5.6: Acceptance map for unpolarized J/ψ (a) and ψ(2S) (b)

Numerical values for average acceptance corrections in all analysis bins are shown in Figures 5.3.4 and 5.8.

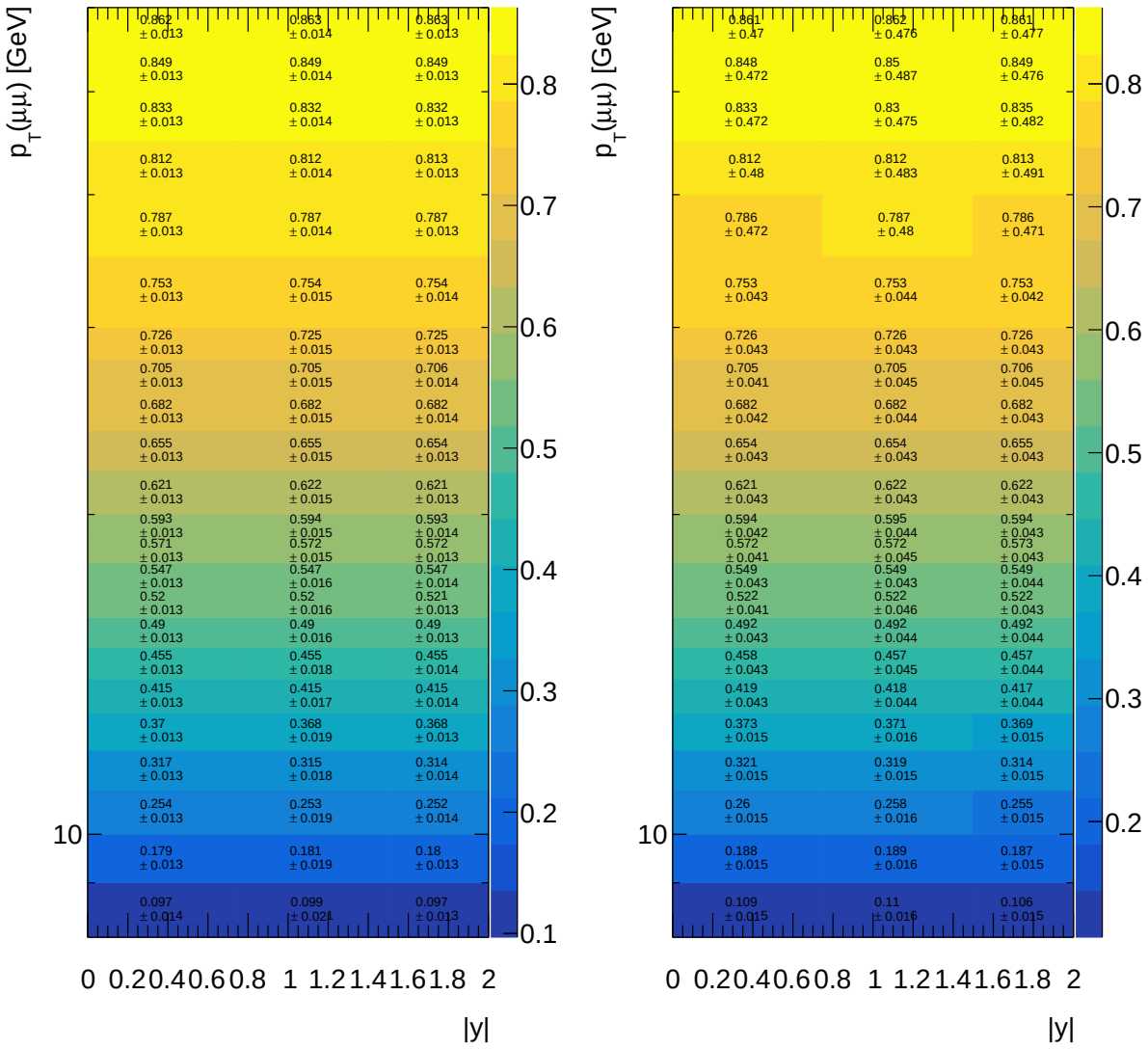

(a) (b)

Figure 5.7: Average acceptance values in low p_{T} analysis bins, for J/ψ (a) and $\psi(2S)$.

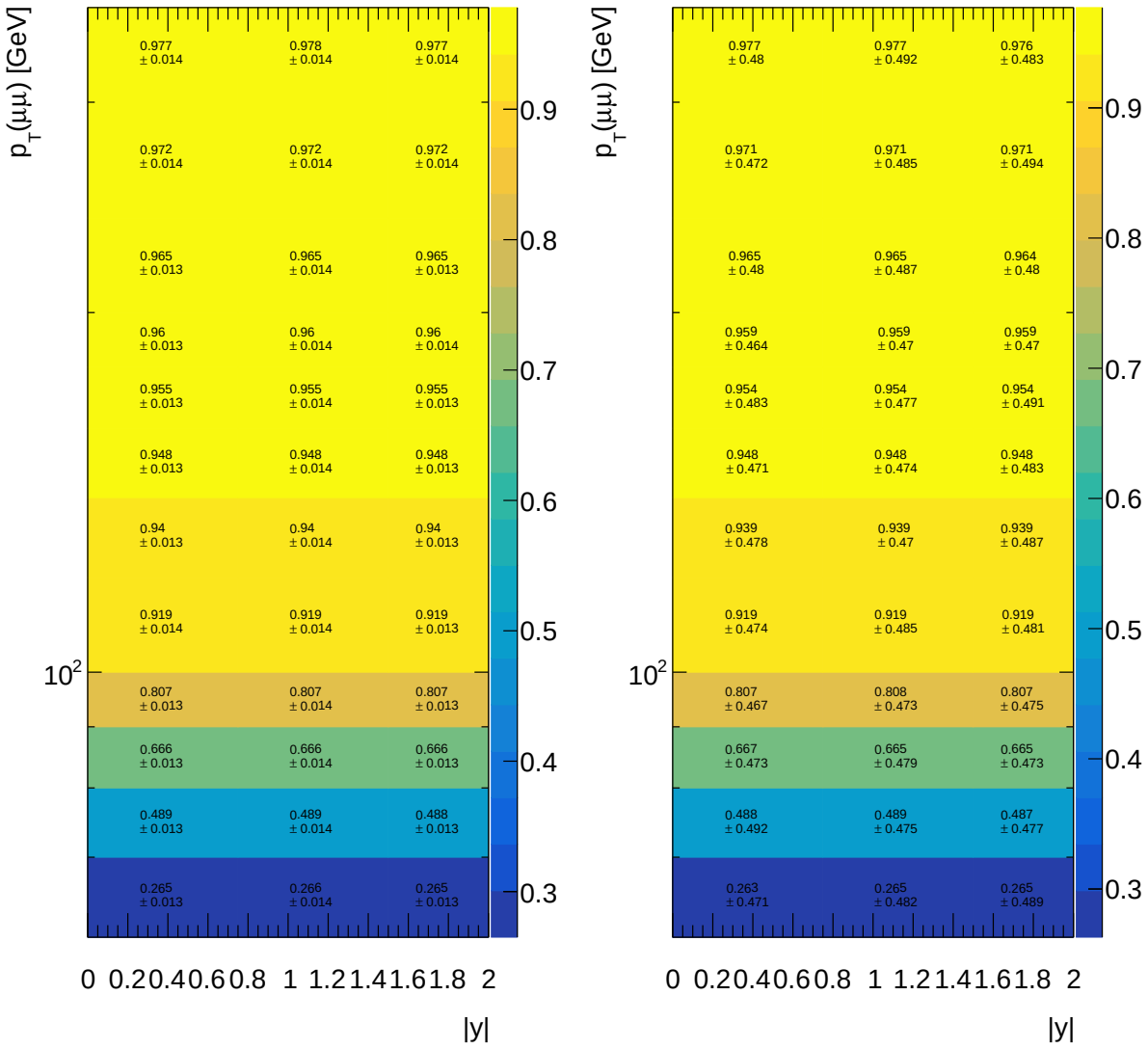

(a) (b)

Figure 5.8: Average acceptance values in high p_{T} analysis bins, for J/ψ (a) and $\psi(2S)$ (b).

The correction factors for different spin-density scenarios are shown in the Appendix D.

5.3.5 Efficiency corrections

Yields obtained from 2D maximum likelihood fits in each analysis (sub)bin, after acceptance corrections, are also corrected using reconstruction and trigger efficiencies obtained from J/ψ and $\psi(2S)$ Monte Carlo simulations, followed by the scale factors taking into account MC-data differences, as shown in eq. (5.3).

As mentined above, the acceptance is defined in the space of true variables, with fiducial cuts also defined in terms of true variables. On the contrary, the measurement is happening in the space of reconstructed p_{T} and y, fiducial cuts are applied in reconstructed variables, and binning is also done in terms of reconstructed variables. In order to correct the observed cross sections to the desired level of true variables, three tasks need to be performed:

- the binning in true variables needs to be 'translated' to the binning in reconstructed variables;
- acceptance defined in true variables need to be corrected to the level of reconstructed variables;
- events that have not been reconstructed need to be accounted for.

With a perfect Monte Carlo, all three tasks can be achieved by introducing a reconstruction efficiency ϵ_{reco}, defined, in each (sub)bin, as the ratio

$$\epsilon_{\text{reco}} = \frac{\text{reco yield in reco bins with reco acc.cuts}}{\text{true events in true bins with true acc.cuts}} \tag{5.9}$$

Under this notation, the trigger efficiency ϵ_{trig} (defined fully in terms of reconstructed variables) in each analysis (sub)bin is

$$\epsilon_{\text{trig}} = \frac{\text{number of triggered events among the reco yield}}{\text{reco yield in reco bins with reco acc.cuts}} \tag{5.10}$$

Since two different triggers are used in this measurement, the trigger efficiencies are different: in analysis bins below $p_{\mathrm{T}} = 60$ GeV the dimuon '2mu4' trigger efficiency correction is applied, while in analysis bins above $p_{\mathrm{T}} = 60$ GeV it's the single muon 'mu50' trigger efficiency.

With efficiencies defined this way, the desired true cross section is obtained from the raw yield after dividing the yield by ϵ_{reco} and acceptance $\mathcal{A}$, followed by the corrections for trigger

efficiency ϵ_{trig} and corrections for any differences between MC and real data, covered by trigger and reconstruction scale factors, ϵ_{trigSF} and ϵ_{recoSF}, respectively (see eq. (5.3)).

The efficiencies ϵ_{trig} and ϵ_{reco} are obtained using a combination of prompt, non-prompt and 'particle gun' Monte Carlo samples. They are shown in Figs. 5.9, 5.10 and Figs. 5.11, 5.12, respectively.

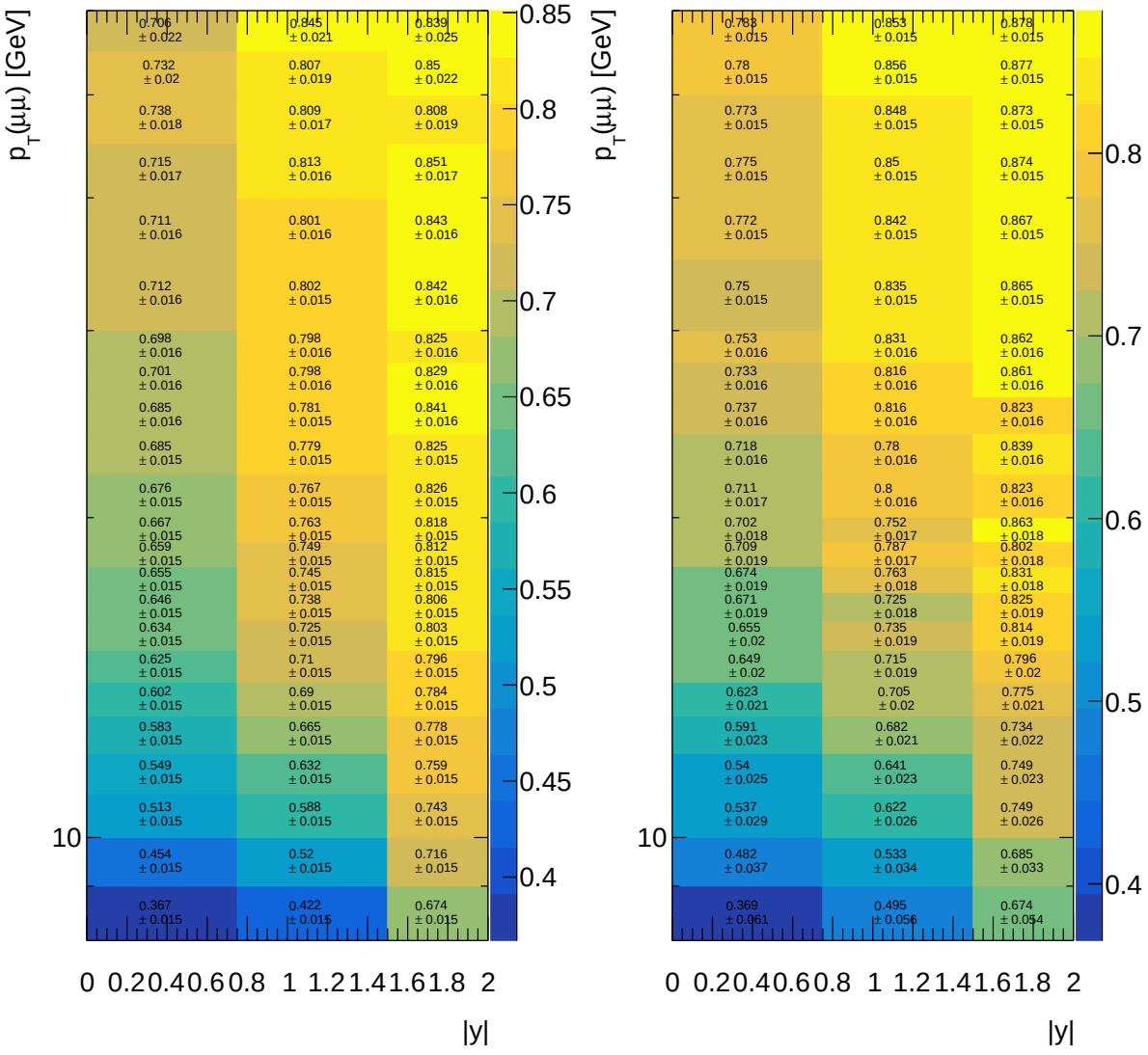

(a) (b)

Figure 5.9: Reconstruction efficiencies in low p_{T} analysis bins, for J/ψ (a) and $\psi(2S)$ (b).

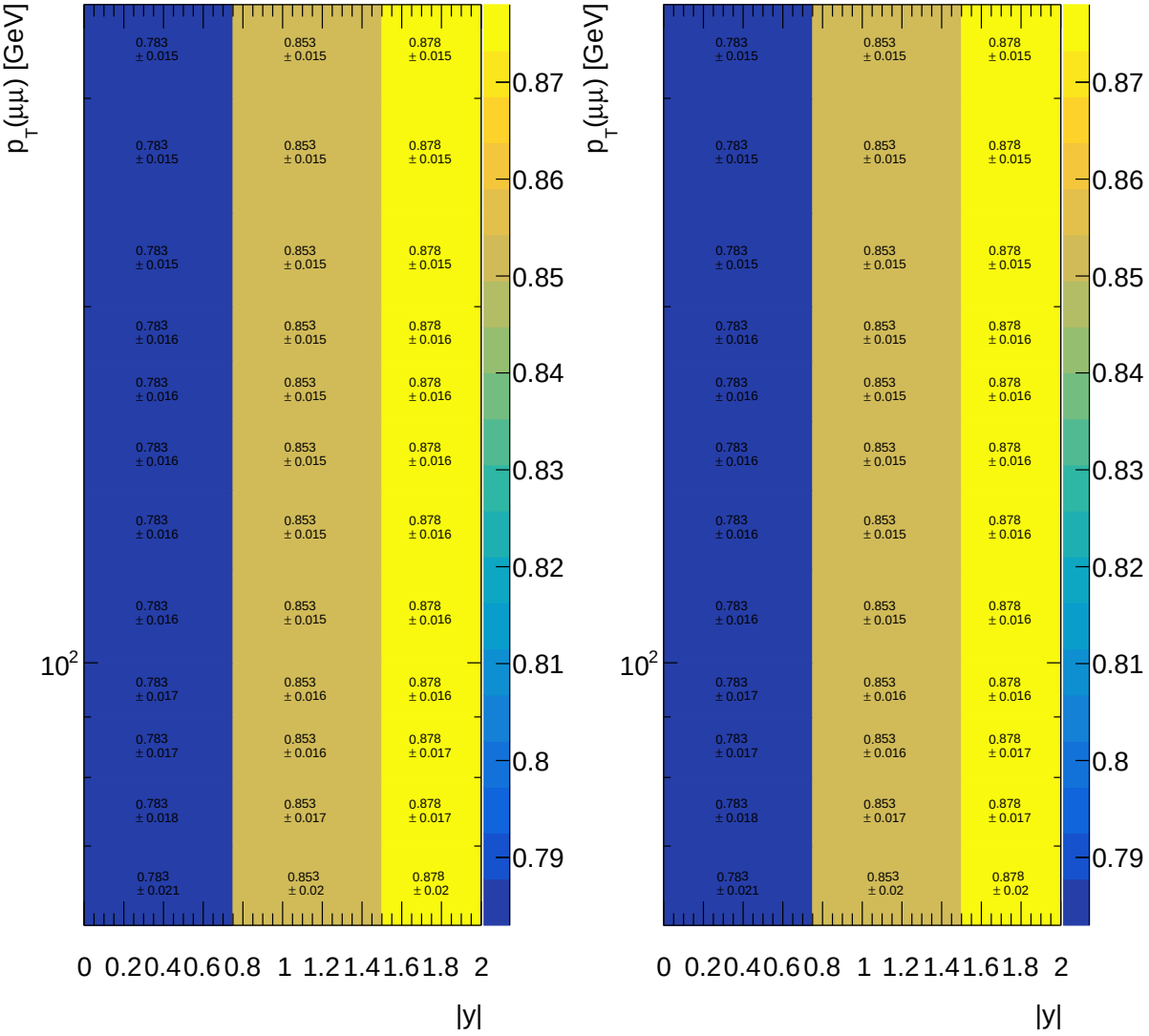

(a) (b)

Figure 5.10: Reconstruction efficiencies in high p_{T} analysis bins, for J/ψ (a) and $\psi(2S)$ (b).

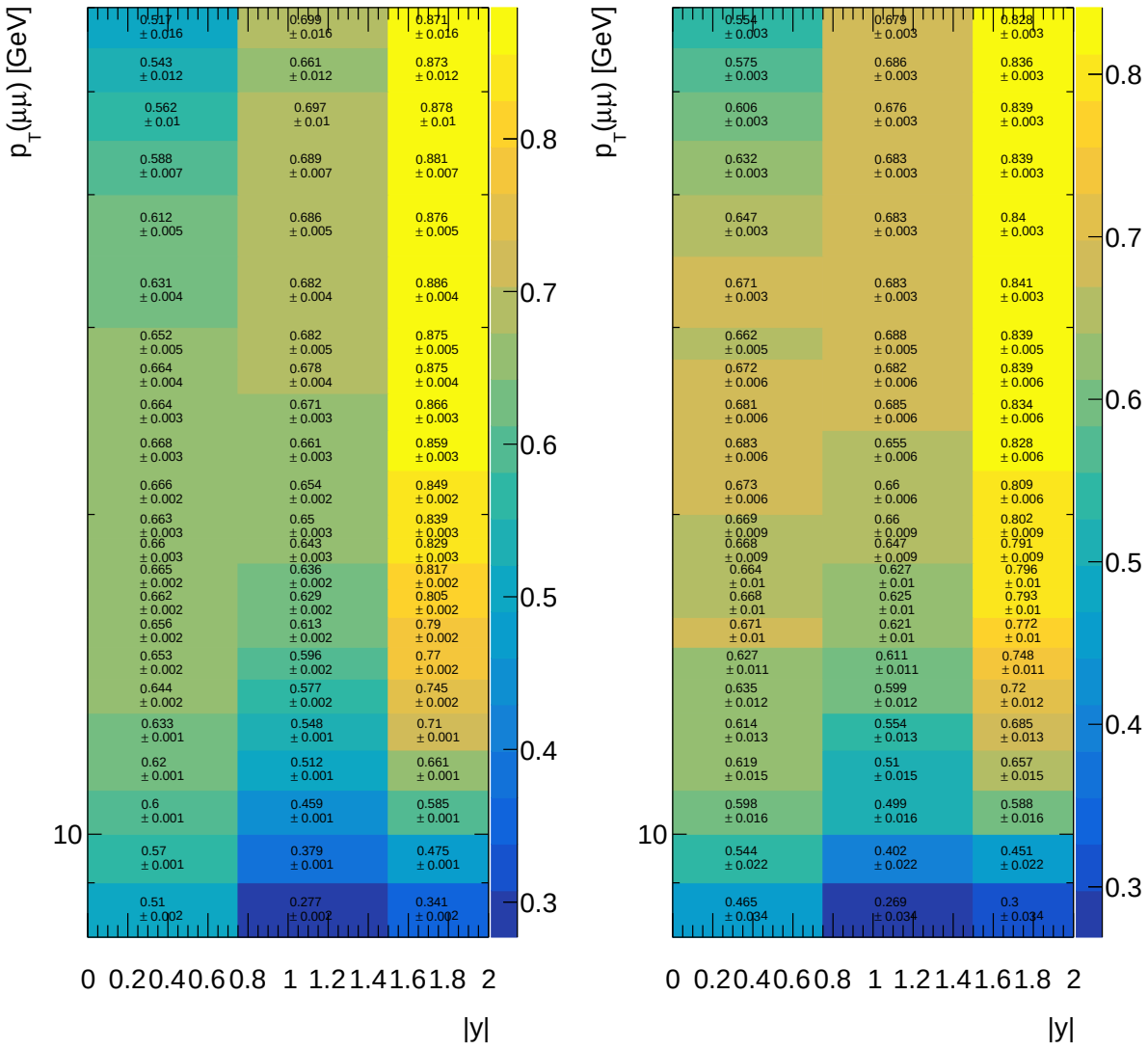

(a) (b)

Figure 5.11: Trigger efficiencies in low p_{T} analysis bins, for J/ψ (a) and $\psi(2S)$ (b).

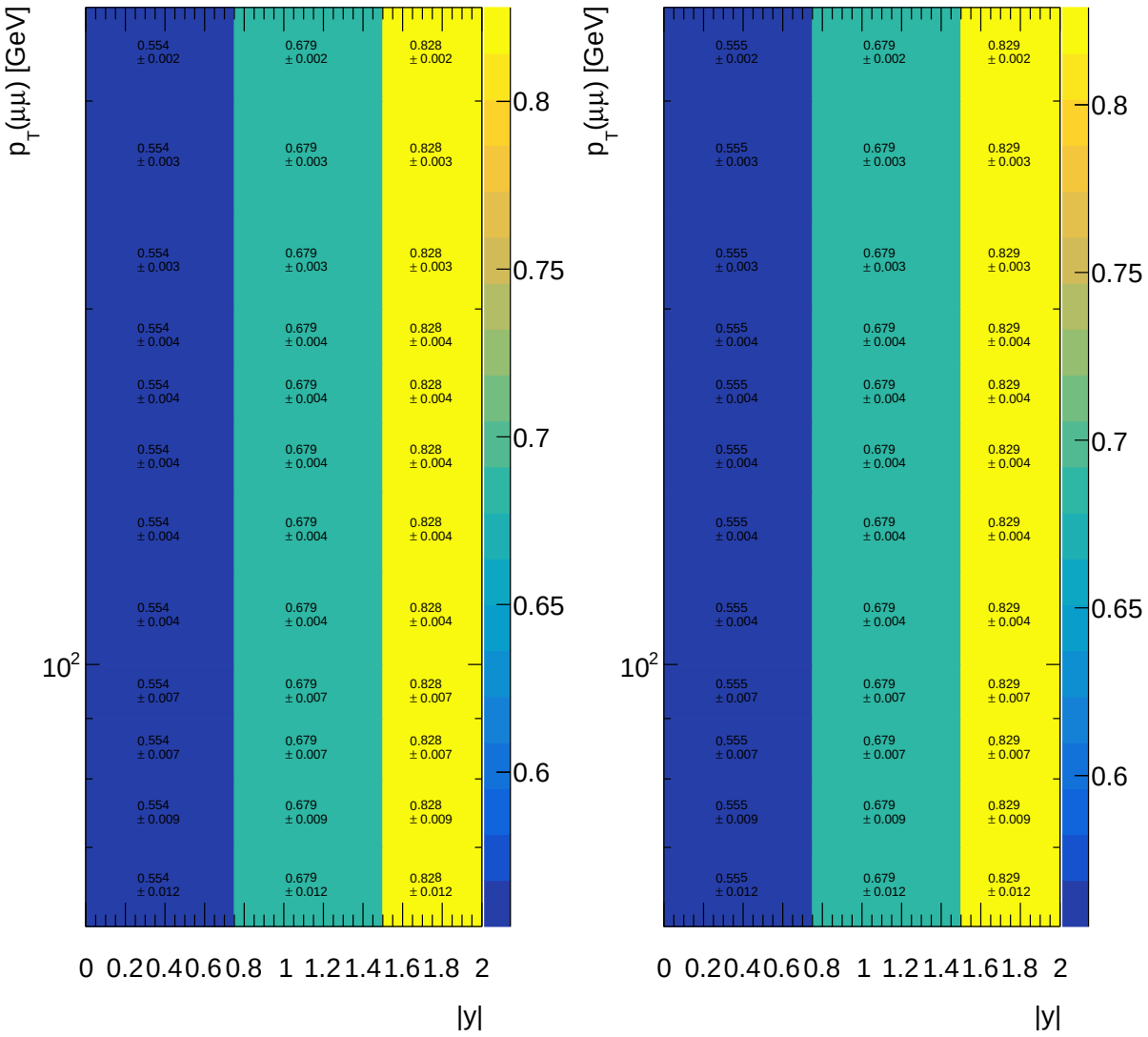

(a) (b)

Figure 5.12: Trigger efficiencies in high p_{T} analysis bins, for J/ψ (a) and $\psi(2S)$ (b).

The data-MC scale factor corrections are obtained using the maps provided by the relevant performance groups. The factors ϵ_{trigSF} for the two triggers are shown in Figures 5.13 and 5.14 respectively.

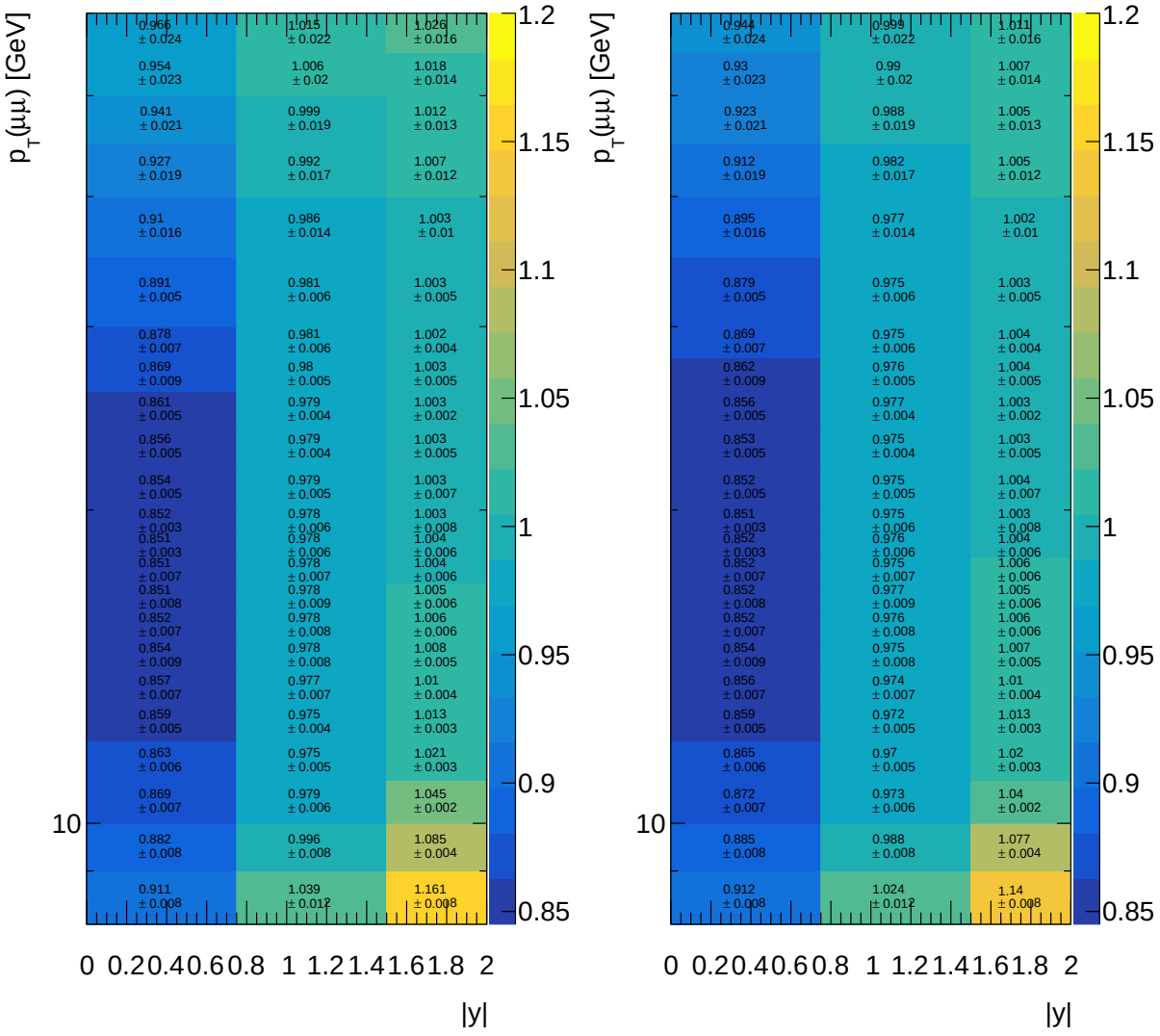

(a) (b)

Figure 5.13: Trigger scale factors in low p_{T} analysis bins, for J/ψ (a) and $\psi(2S)$ (b).

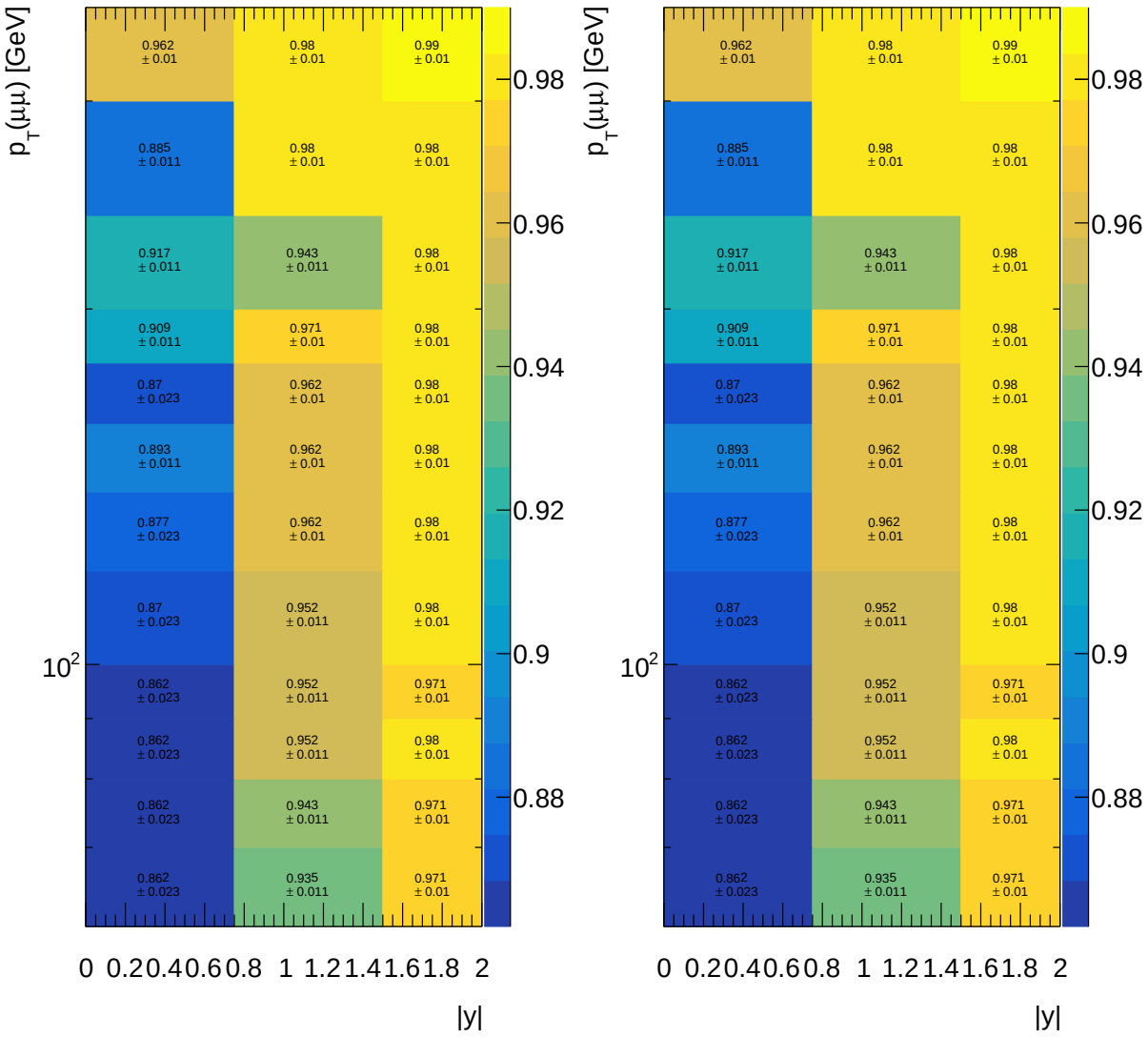

(a) (b)

Figure 5.14: Trigger scale factors in high p_{T} analysis bins, for J/ψ (a) and $\psi(2S)$ (b).

The reconstruction scale factors ϵ_{recoSF} were obtained using the maps provided by respective performance group - Muon Combined Performance (MCP) group and were found to be universally close to unity, in the range 0.99 ± 0.01, details can be found in Ref. (Kartvelishvili et al., 2019). This correction was applied to all data points, and the uncertainty was added to the list of systematics.

The results for all 8 measured distributions: J/ψ and $\psi(2S)$ cross sections and non-prompt fractions, and $\psi(2S)$ to J/ψ production ratios for prompt and non-prompt contributions, extracted from the fit results and corrected for trigger and reconstruction efficiencies and scale factors, are shown in Figures 5.15 – 5.17. At this stage the errors are statistical only.

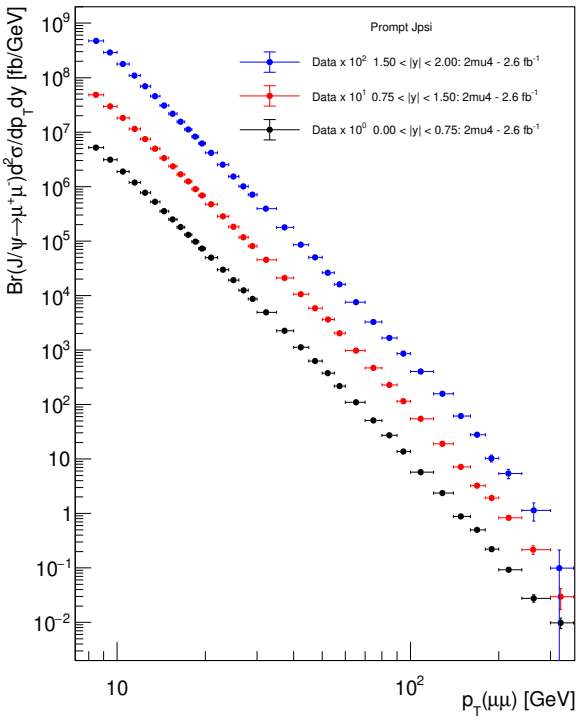

(a)

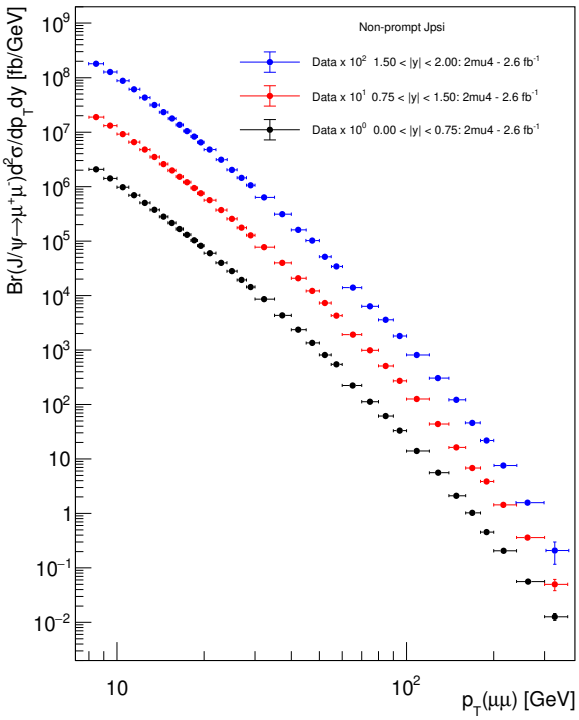

(b)

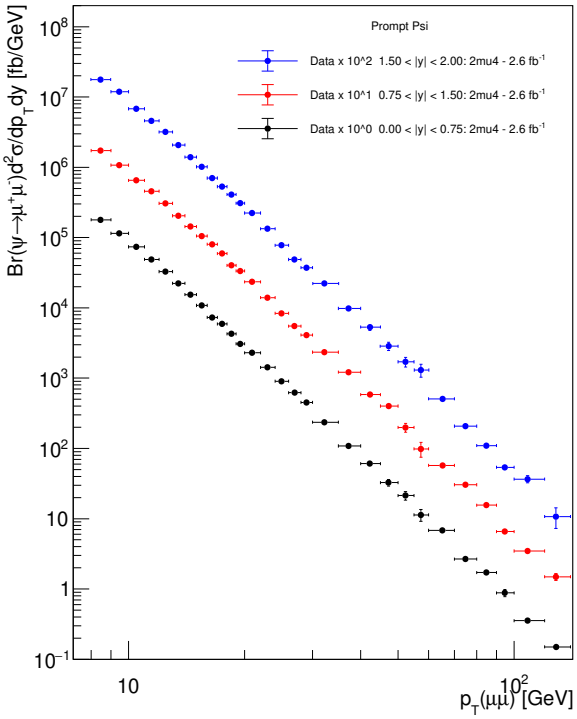

(c)

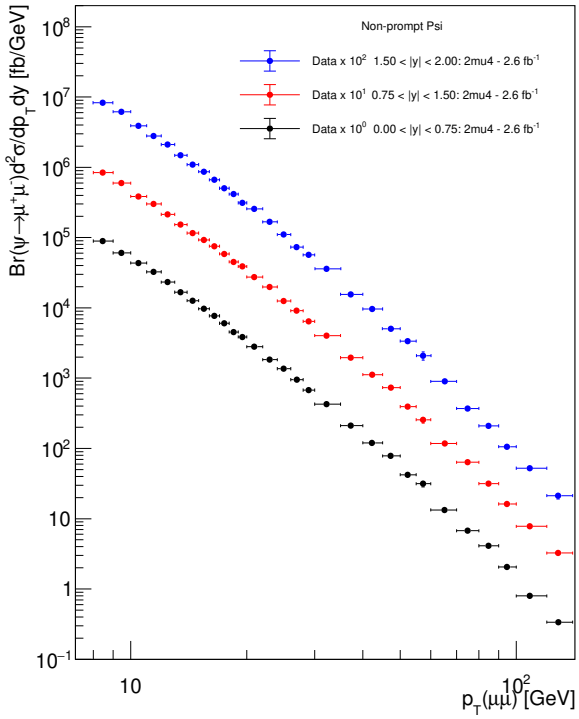

(d)

Figure 5.15: Differential cross sections of prompt J/ψ (a), non-prompt J/ψ (b), prompt $\psi(2S)$ (c) and non-prompt $\psi(2S)$ (d). All errors are statistical only.

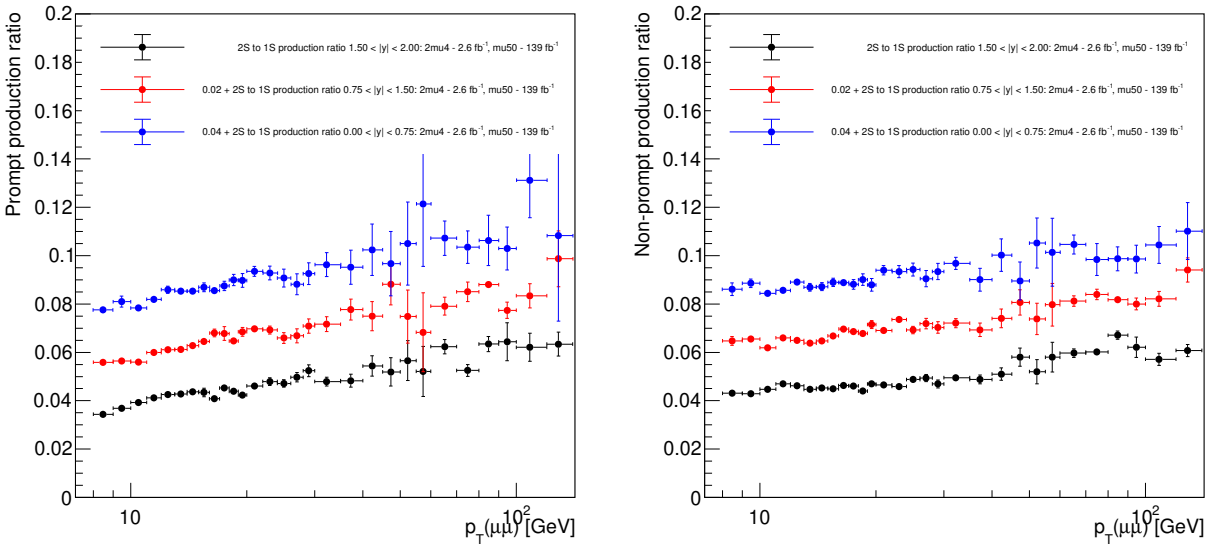

(a) (b)

Figure 5.16: Ratio of prompt (a) and non-prompt (b) $\psi(2S)$ to J/ψ production. All errors are statistical only.

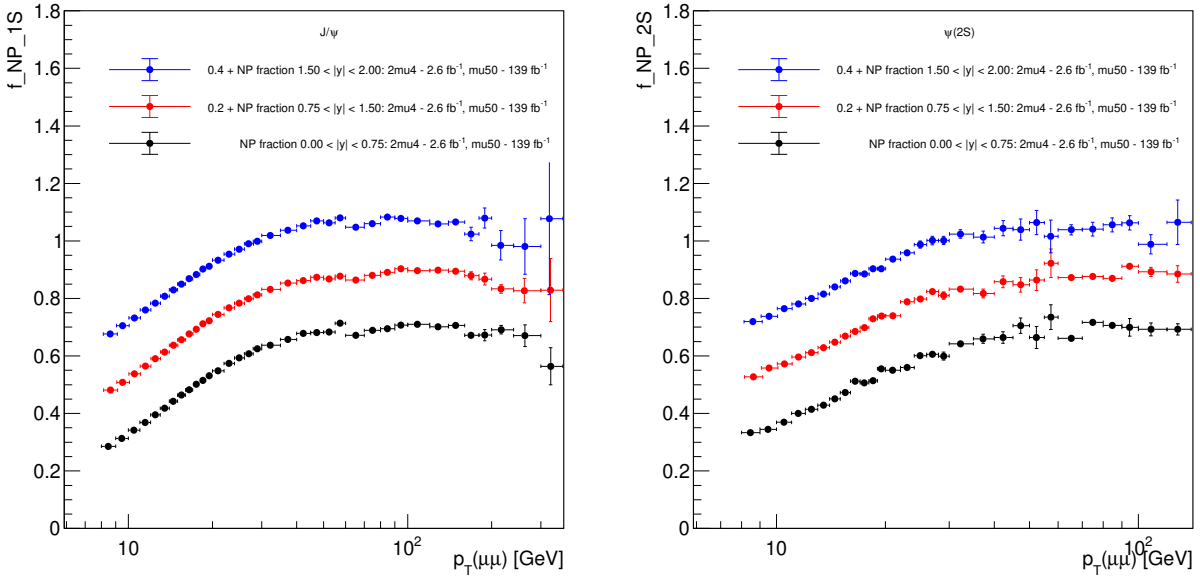

(a) (b)

Figure 5.17: Non-prompt fraction of J/ψ (a) and $\psi(2S)$ (b). Errors are statistical only.

5.4 Systematic studies

From past experience and current observations, the following systematic effects are expected to be significant:

1. Acceptance systematics.
2. Trigger efficiency systematics.
3. Reconstruction efficiency systematics.
4. Fit model systematics.
5. Luminosity uncertainty.
6. Spin alignment correction factors.

Each of these are considered separately below. The plots illustrating fractional statistical, total systematic and individual systematic uncertainties in each of the analysis bins for each of the 8 measured quantities are collected in subsection 5.5.

5.4.1 Acceptance-related systematics

Acceptance is a truth-space quantity, and acceptance-related systematics is in fact dominated by the statistics used to generate the corresponding acceptance maps. The maps, that are defined within the range $8 < p_{\mathrm{T}}(\mu\mu) < 400$ GeVand $|y(\mu\mu)| < 2.4$, corresponding to the data considered in the analysis. The map is defined in 8 slices in $|y(\mu\mu)|$ and 1000 bins in $p_{\mathrm{T}}(\mu\mu)$, using 100k trials for each point, resulting in sufficiently high precision, such that its statistical uncertainty is less than many other sources of systematics.

Fractional errors due to acceptance systematics are shown as red dashed lines in figures in subsection 5.5.5.

5.4.2 Trigger efficiency systematics

The systematics on trigger efficiency corrections has a number of components.

1. systematics on correction for trigger efficiency, calculated using MC samples, with respect to reconstructed events.

2. systematics on correction for trigger matching, to make sure that the two triggered muons indeed belong to the ψ state.

3. systematics on correction for trigger scale factor, accounting for differences between the data and MC simulations.

The systematic error for item 1 is calculated in each analysis bin as the binomial error on the ratio of triggered reconstructed events to the number of reconstructed events.

The systematic error for item 2 is calculated in each analysis bin as the binomial error on the ratio of triggered reconstructed events with matched muons to the number of triggered reconstructed events.

The systematic error for item 3 is calculated using the maps provided by the respective performance group, separately for low p_{T} bins with the 2mu4 trigger and high p_{T} bins with the mu50 trigger.

Fractional errors from these three sources in each bin were added in quadrature to form the overall systematic uncertainty for trigger efficiency, shown with blue dash-dotted lines in the plots in subsection 5.5.5.

5.4.3 Reconstruction efficiency systematics

As mentioned above, in order to correct the observed yields in reconstructed variables to the desired level of true variables, three tasks need to be performed:

1. the binning in true variables needs to be 'translated' to the binning in reconstructed variables;

2. acceptance defined in true variables need to be corrected to the level of reconstructed variables;

3. events from the true bin that have not been reconstructed need to be accounted for.

Using Monte Carlo samples listed in subsection 5.3.4.5.3.3, all three tasks were achieved by introducing in each (sub)bin the reconstruction efficiency, ϵ_{reco}, defined as the ratio of reconstructed events in a reconstructed (sub)bin, with acceptance cuts applied to reconstructed variables $N(RRR)$, over the number of true events in a true (sub)bin with acceptance cuts applied to true variables, $N(TTT)$

$$\epsilon_{\text{reco}} = \frac{N(RRR)}{N(TTT)} \tag{5.11}$$

In order to achieve a better understanding and a better control on respective uncertainties, the ratio (5.11) was decomposed into three ratios:

$$\epsilon_{\text{reco}} = \frac{N(RRR)}{N(TRR)} \cdot \frac{N(TRR)}{N(TTR)} \cdot \frac{N(TTR)}{N(TTT)} \tag{5.12}$$

Here the first label states whether the binning is done in true T or reconstructed R variables, the second – whether the acceptance cuts are applied on true T or reconstructed R variables, and the third – whether the events were reconstruced R or generated T. So it's the final of the three ratios which represents the probability of the event being reconstructed, but in true variables and acceptance, and the first two ratios represent the bin migration, due to variable definition (first) and acceptance cut "correction" (second). While the efficiency corrrection was applied according to eq.(5.11), the systematics were calculated for the three ratios in (5.12) separately, and then combined in quadrature.

Being a "proper" efficiency, the third ratio has a binomial uncertainty, which depends on MC statistics in the bin, while the first and the second ratios are close to identity and their uncertainties are determined by the fidelity of the MC simulated resolutions in p_{T}, which was found to be good. The first ratio was found to be scattered in various sub-bins within $\pm 1.5\%$ of the central value, which was applied as a corresponding systematic uncertainty. As for the second ratio, It was assessed to be the largest at the low end of p_{T} range, where it reaches 0.7%, and quickly falls at larger p_{T}.

Last part of systematics related to reconstruction is the reconstruction scale factor uncertainty ϵ_{recoSF}. Similarly to the trigger scale factor, the respective systematic error was assessed using the efficiency map scale factors provided by the MCP. This uncertainty was also added in quadrature to form the overall reconstruction systematics, shown on the plots presented in subsection 5.5.5 by the blue dashed lines.

In general, the use of efficiencies obtained from MC can depend on how close the data and the MC are in various differential distributions. In particular, in the low pT range, the shapes of individual MC samples do not follow the data, simply because the data contains a mix of prompt and non-prompt events which have different pT dependences. The efficiencies were obtained separately from prompt and non-prompt samples, with the difference assigned as a systematic uncertainty. In the high pT range, the MC samples were in fact particle-gun generated, with flat pT dependence, which were reweighted to data using smooth analytical function. The efficiencies were reweighted to match the distributions of J/ψ mesons in p_{T} and rapidity, and also in pileup (i.e. the number of primary vertices in the event).

5.4.4 Fit model variation systematics

As mentioned before, the fits are fairly complicated. Many of the 29 parameters have been fixed to some pre-determined values during the nominal fits. Variation of these parameters affects the yields and fractions extracted from the fits, so a number of studies are performed to assess the effects of varying these fixed parameters on the measured quantities.

Some of the parameters have been released, one at a time, and the fits were re-run. In some other cases, the fixed values were changed by a pre-determined amount, and the fits re-run. In a few cases, a parameterisation used in the main fit was replaced by some other parameterisation and the fit was re-run. After each re-run, changes in the measured yields and non-prompt fractions were recorded. At the end of this process, in each analysis (sub)bin, each yield or fraction gets a number of measurements, usually scattered around the result of the nominal fit. These measurements are not independent but are expected to be (strongly) correlated with each other, and follow some (unknown) probability distribution. In order to obtain a value for the systematic uncertainty corresponding to the fit variations, it is assumed that the above probability distribution is flat, and hence a 'one-sigma' uncertainty would correspond to the maximum deviation from the central value divided by $\sqrt{3}$.

The details of the 14 fit variations, and the results of these variations for each analysis bin and each of the 8 measured quantities are presented in Appendix A.

5.4.5 Luminosity systematics

The uncertainty in the combined 2015–2018 integrated luminosity is 1.7% (ATLAS Collaboration, 2019), obtained using the LUCID-2 detector (Avoni et al., 2018) for the primary luminosity measurements. This is relevant for high p_{T} bins.

In the low p_{T} part, only the integrated luminosity corresponding to the 2mu4 trigger in 2015 contributes to this measurement. This integrated luminosity has the uncertainty of 2.1% (ATLAS Collaboration, 2019; Avoni et al., 2018).

5.4.6 Spin alignment correction factors

Spin alignment correction factors are calculated as described in section 5.3.4. Tables contained in the Appendix D show spin-alignment correction factors for various spin-alignment scenarios.

5.5 Fractional uncertainties

The fractional uncertainty for each analysis bin are shown on Figures 5.18 - 5.25. Total uncertainty contributions are following:

1. Statistical
2. Acceptance
3. Reconstruction
4. Trigger
5. Fit variation

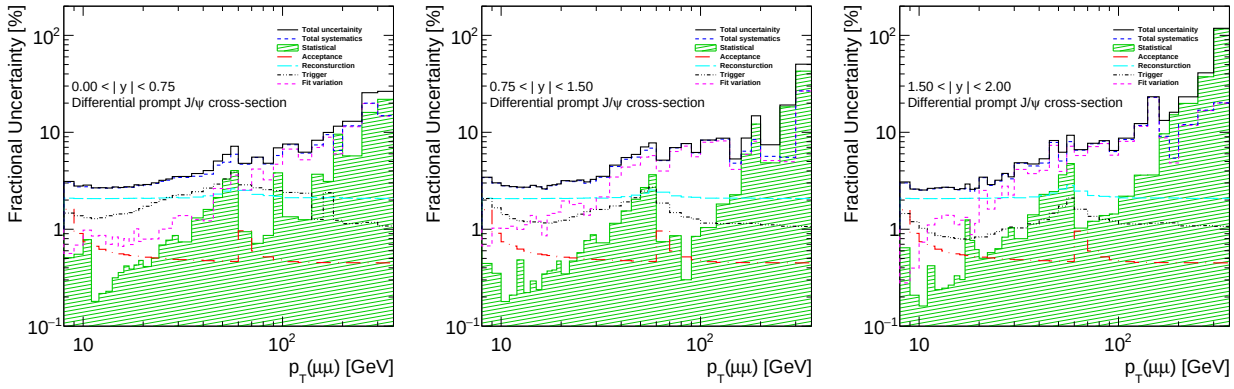

(a) (b) (c)

Figure 5.18: The fractional uncertainty contributions of the differential prompt J/ψ cross-section shown as a function of p_T in bins of increasing rapidity.

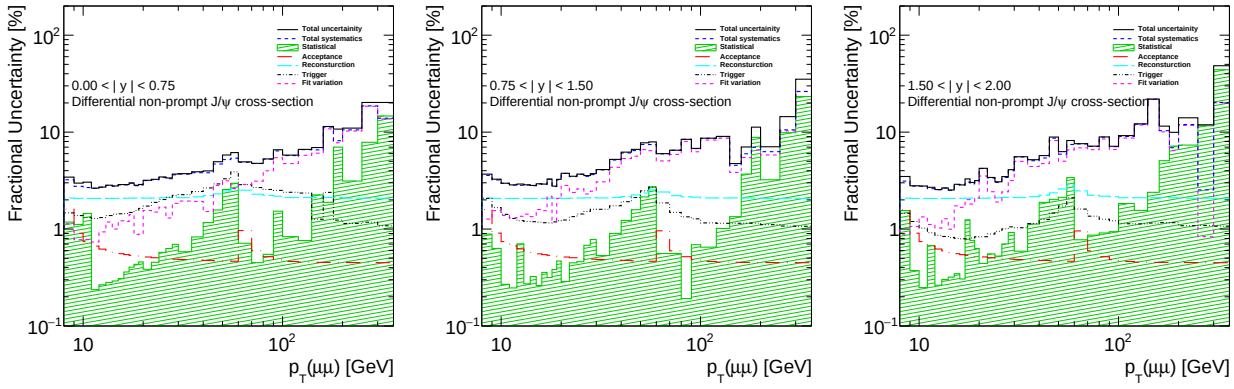

(a) (b) (c)

Figure 5.19: The fractional uncertainty contributions of the differential non-prompt J/ψ cross-section shown as a function of p_T in bins of increasing rapidity.

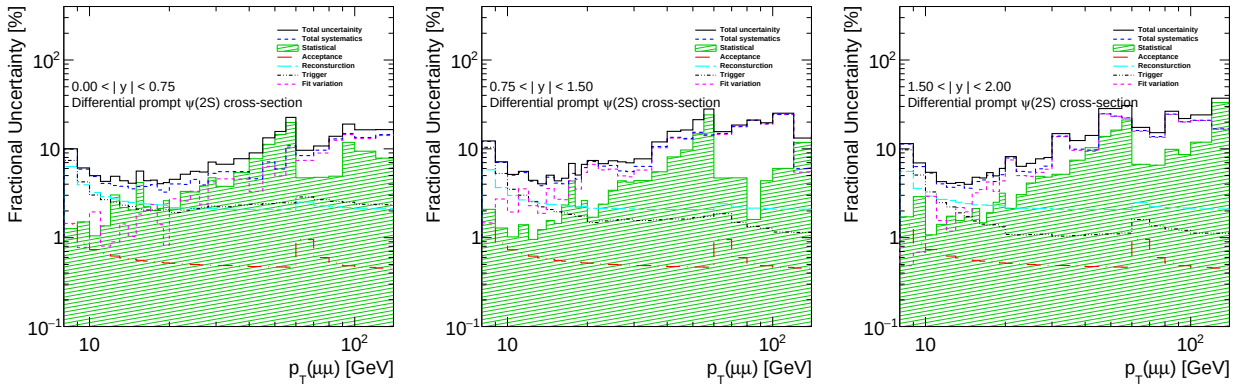

(a) (b) (c)

Figure 5.20: The fractional uncertainty contributions of the differential prompt $\psi(2S)$ cross-section shown as a function of p_T in bins of increasing rapidity.

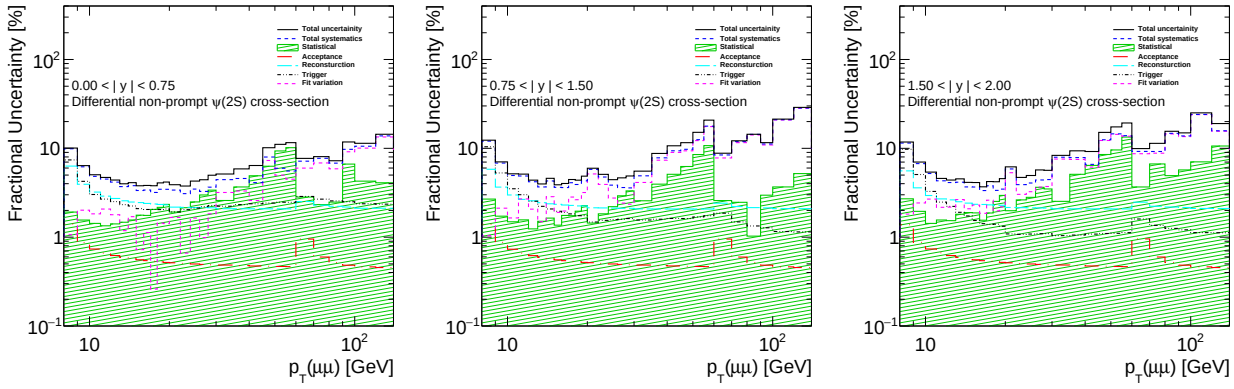

(a) (b) (c)

Figure 5.21: The fractional uncertainty contributions of the differential non-prompt $\psi(2S)$ cross-section shown as a function of p_T in bins of increasing rapidity.

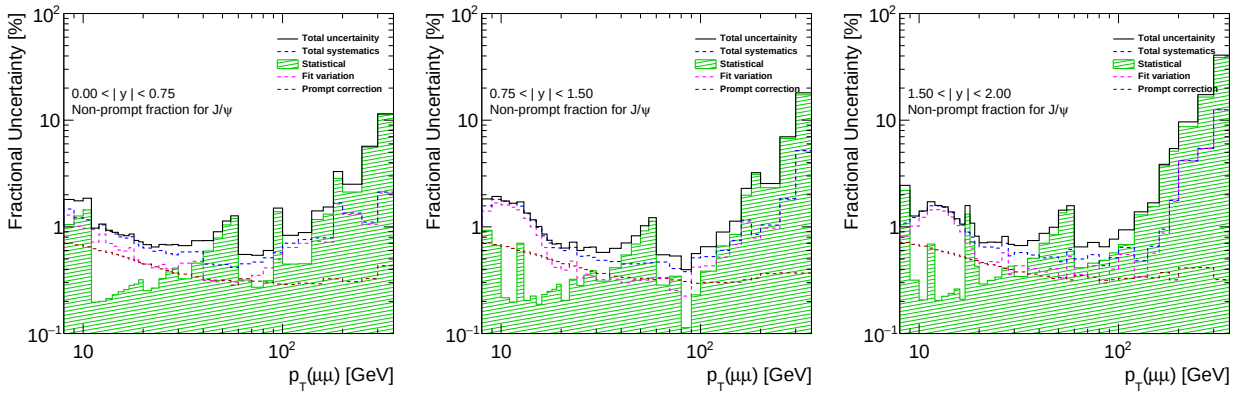

(a) (b) (c)

Figure 5.22: The fractional uncertainty contributions of the non-prompt fraction of J/ψ shown as a function of p_T in bins of increasing rapidity.

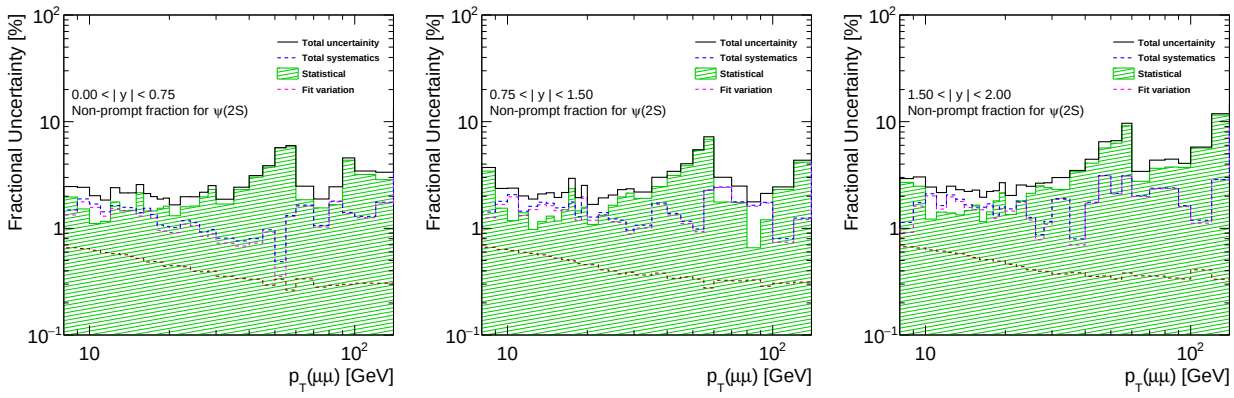

(a) (b) (c)

Figure 5.23: The fractional uncertainty contributions of the non-prompt fraction of $\psi(2S)$ shown as a function of p_T in bins of increasing rapidity.

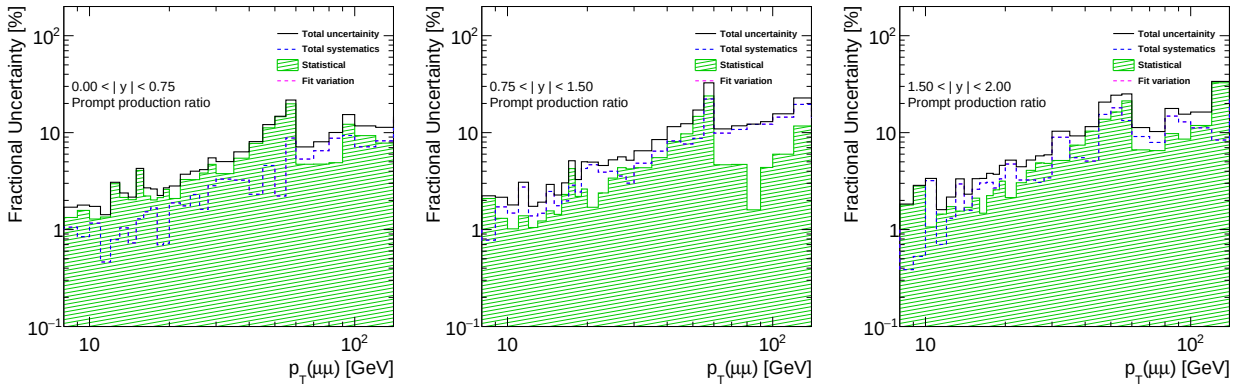

(a) (b) (c)

Figure 5.24: The fractional uncertainty contributions of the prompt production ratio shown as a function of p_T in bins of increasing rapidity.

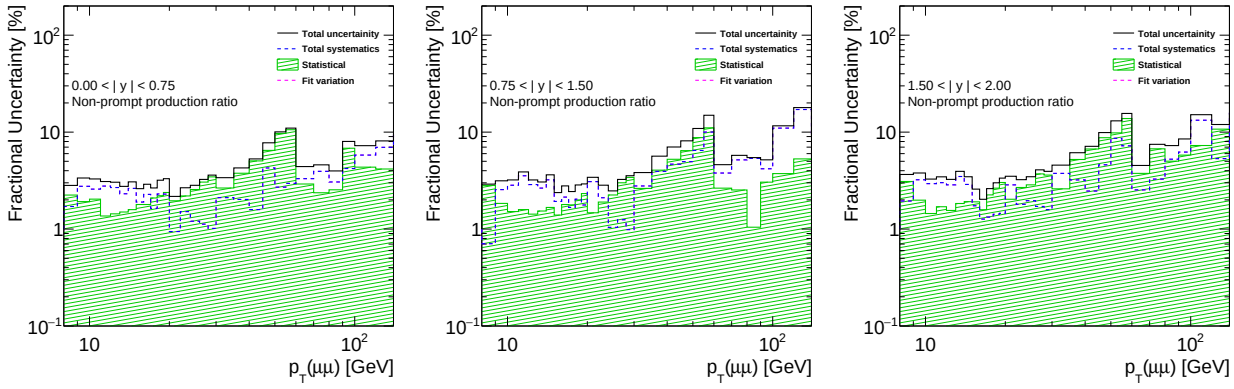

(a) (b) (c)

Figure 5.25: The fractional uncertainty contributions of the non-prompt production ratio shown as a function of p_T in bins of increasing rapidity.

5.6 Results

The results shown in this section include all systematic uncertainties.

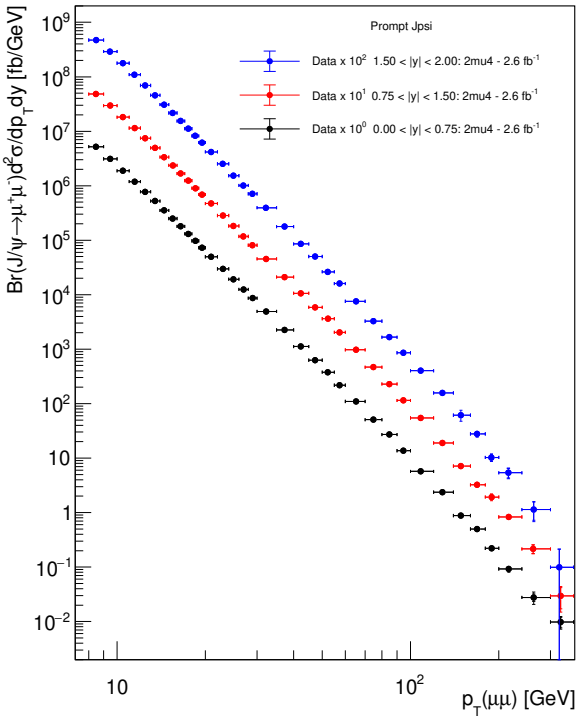

(a)

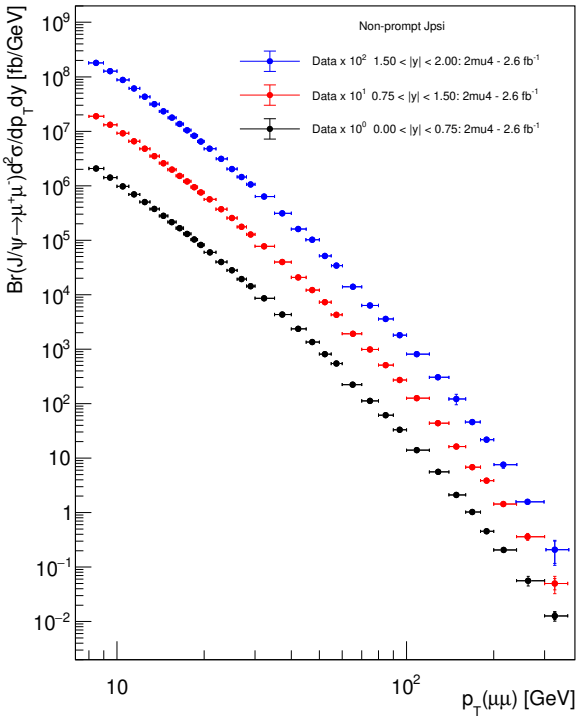

(b)

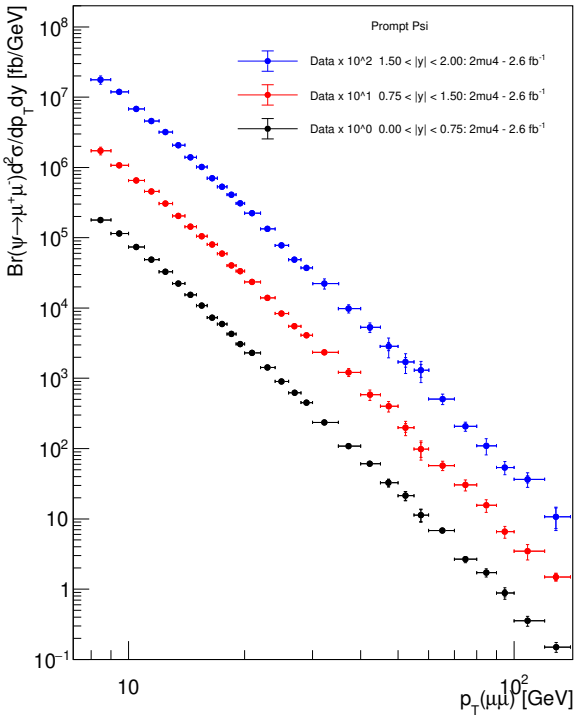

(c)

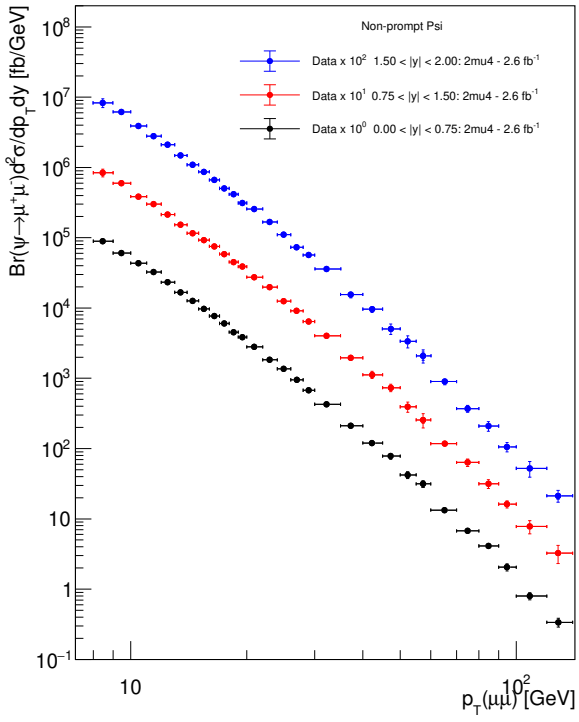

(d)

Figure 5.26: Differential cross sections of prompt J/ψ (a), non-prompt J/ψ (b), prompt $\psi(2S)$ (c) and non-prompt $\psi(2S)$ (d). Statistical and systematical errors are combined. Non-prompt cross sections are overlaid with FONLL predictions.

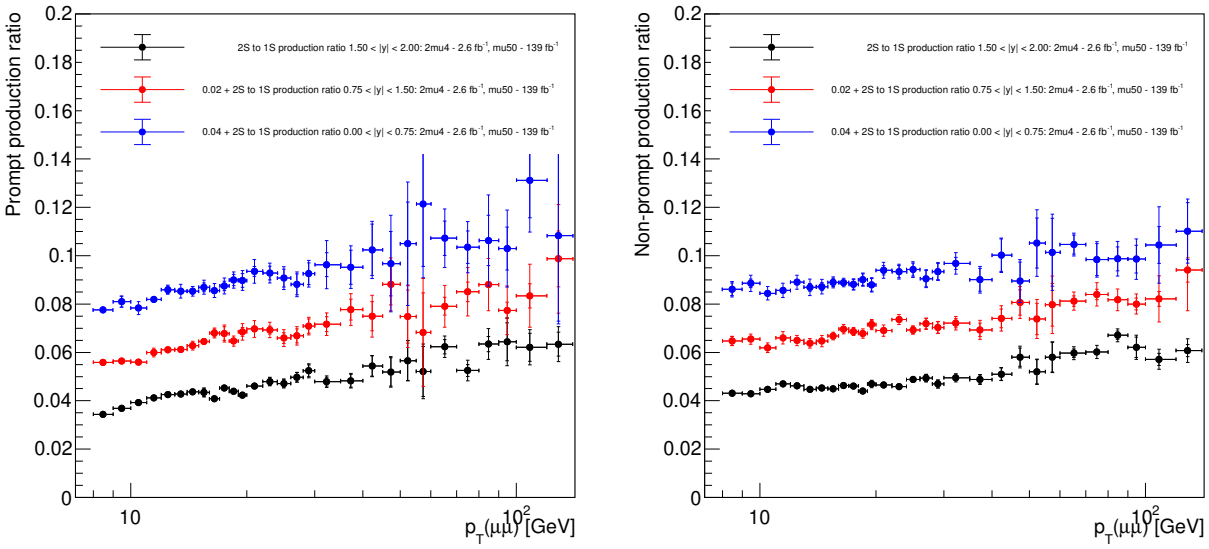

(a) (b)

Figure 5.27: Ratio of prompt (a) and non-prompt (b) $\psi(2S)$ to J/ψ production. Statistical and systematical errors are combined. Purple points show the same ratio at 8 TeV, for the central rapidity region.

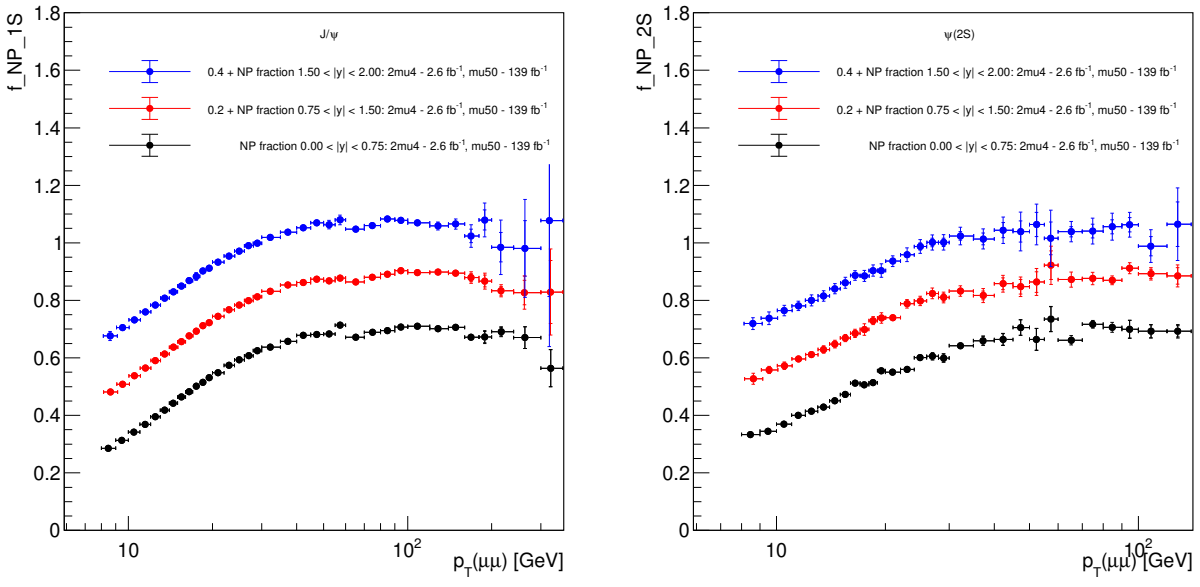

(a) (b)

Figure 5.28: Non-prompt fraction of J/ψ (a) and $\psi(2S)$ (b). Statistical and systematical errors are combined.

5.7 Summary

In the thesis was described the procedure and the results of a measurement of J/ψ and $\psi(2S)$ production, using the ATLAS detector and the full Run 2 data set collected with pp collisions at 13 TeV. Non-prompt fractions of J/ψ and $\psi(2S)$ are also measured, as well as the production ratios of $\psi(2S)$ to J/ψ, separately for prompt and non-prompt production mechanisms.

The measurements cover the range of transverse momenta between 8 and 360 GeV for J/ψ and 8 to 140 gev for $\psi(2S)$, and the range of rapidities between -2 and $+2$.

Our results are consistent with similar results obtained by the CMS collaboration (CMS Collaboration, 2018), and ALICE collaboration (Acharya et al., 2022) (Figure 5.29). FONLL predictions (?, ?) describe the non-prompt production results reasonably well, see Figures 5.30 and 5.31. Other theory predictions are being sought.

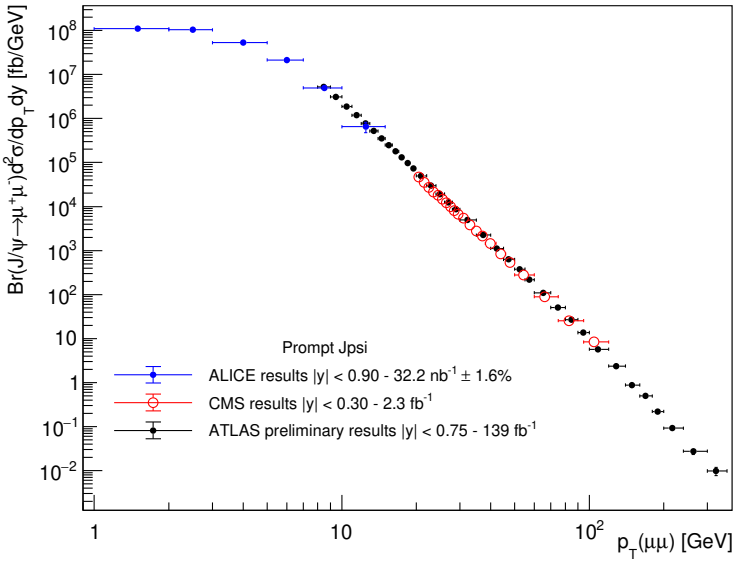

(a)

Figure 5.29: Comparison of the differential cross-section of prompt J/ψ production measured by ATLAS in the central rapidity range with the CMS (CMS Collaboration, 2018) and ALICE (Acharya et al., 2022) result in the closest-matching rapidity range.

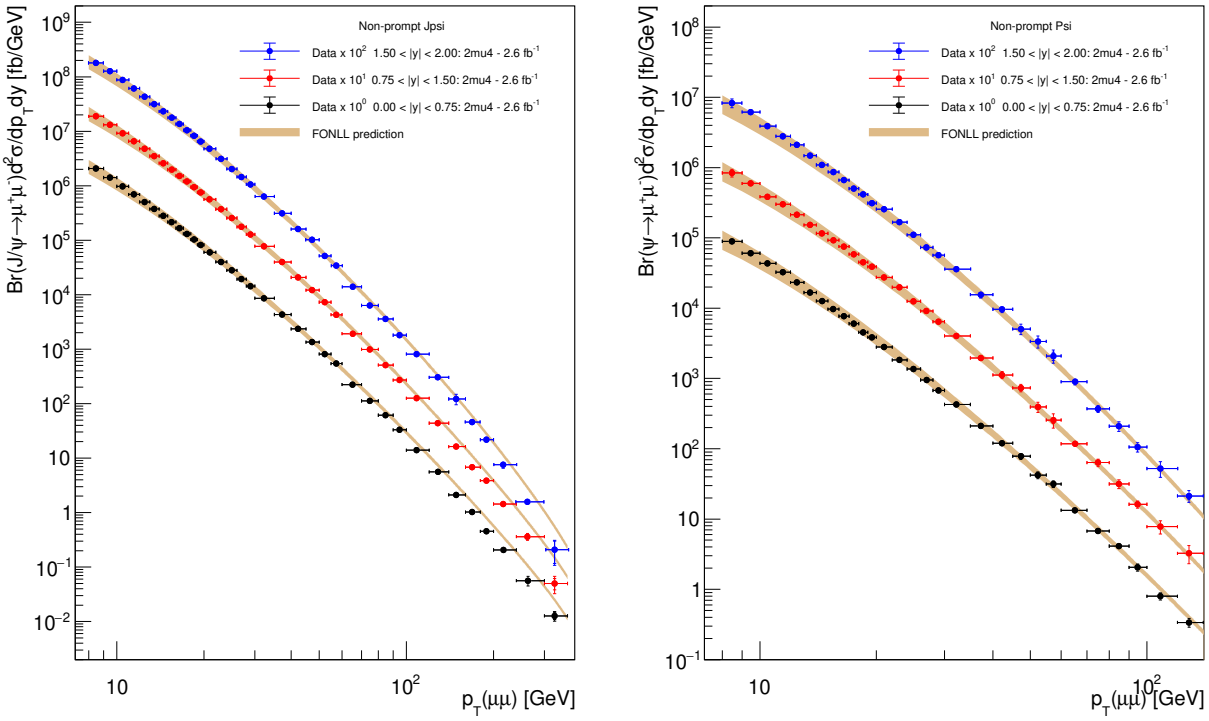

(a) (b)

Figure 5.30: Differential cross sections of non-prompt J/ψ (a) and non-prompt $\psi(2S)$ (b) overlaid with FONLL predictions.

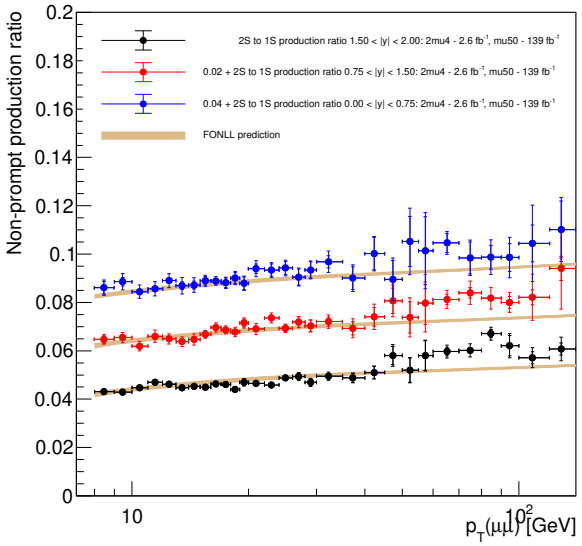

(a)

Figure 5.31: Ratio of non-prompt $\psi(2S)$ to J/ψ production overlaid with FONLL predictions.

Chapter 6

Summary and conclusions

In this thesis, first part is dedicated to investigation of the ATLAS hadronic calorimeter response to test beams. To date, has been built a Demonstrator - a fully functional prototype of the new system. The Demonstrator is a hybrid module equipped with the upgraded electronics that was installed into the ATLAS experiment for the evaluation of the new readout architecture for the ATLAS Phase-II Upgrade. The response of the TileCal Demonstrator module was studied using the 2016–2018 and 2021–2022 test beam data. The Demonstrator response is studied with 150 GeV, 160 GeV, 165 GeV and 300 GeV muon beam hitting the module from $\pm 90^{\circ}$. Noise thresholds of new electronics were evaluated and layer response uniformity was studied. Results show a layer response response uniformity within 1%. While comparing data to simulation, an offset of max 1.4% is observed for Data/MC for A layer, 0.2% for BC layer and 0.4% for D layer. Energy response uniformity is observed cell by cell within uncertainties. Muons entering the calorimeter modules at $\pm 90^{\circ}$ along the centers of the tile-rows are used to cross-check the calibration procedure of the TileCal modules, results obtained are consistent with previously done measurements.

Three spare modules of the ATLAS Tile Calorimeter were exposed to hadron beams from the Super Proton Synchrotron accelerator at CERN in 2017. The measurements of the energy response and resolution of the detector to positive pions and kaons and protons with energy in the range 16 to 30 GeV are reported in this thesis. The results have uncertainties of few percent. They were compared to the predictions of the Geant4-based simulation program used in ATLAS to estimate the response of the detector to proton-proton events at Large Hadron Collider. The determinations obtained using experimental and simulated data agree within the uncertainties. Based on the results obtained, one can conclude, that with the increase of the

hadrons energy, the precision of the energy, measured by the detector, increases as well, and the resolution of the detector improves.

In this thesis, second part describes the results of a measurement of the double-differential production cross-section of J/ψ and $\psi(2S)$ charmonium states through their decays to dimuons in pp collisions at $\sqrt{s} = 13$ TeV, performed using the data collected by the ATLAS detector at the LHC during Run 2. For both production mechanisms - prompt and non-prompt, the cross-sections were measured. Also the non-prompt fractions are measured, and the production ratios of $\psi(2S)$ to J/ψ, for each states. In case of J/ψ, the results cover the rapidity range $|y| < 2$ and the transverse momentum range between 8 GeV and 360 GeV. In case of $\psi(2S)$ the rapidity range is the same, but the transverse momentum range is between 8 GeV and 140 GeV. The transverse momentum range, for both J/ψ and $\psi(2S)$, goes well beyond the values reached so far, so the results may be helpful to discriminate various theoretical models.

Prompt and non-prompt differential cross sections, both show similar p_{T}-dependence. Non-prompt fraction, for both J/ψ and $\psi(2S)$, has a steep increase in low p_{T} region and is close to constant in high p_{T} region. The results for non-prompt production are compared with the predictions of the FONLL model, with default set of parameters and the results show that these predictions are consistent with the measurements measurements presented in thesis, at the low end of the p_{T} range, but exceed the experimental values at large transverse momenta.

References

A. Solodkov. (2017, May). *Upgrade of the ATLAS hadronic Tile Calorimeter for the High luminosity LHC* (Tech. Rep.). Geneva: CERN. Retrieved from https://cds.cern.ch/record/2264924 doi: 10.1088/1748-0221/12/08/C08004

Aad, G., et al. (2016). Measurement of the differential cross-sections of prompt and non-prompt production of J/ψ and $\psi(2S)$ in pp collisions at $\sqrt{s} = 7$ and 8 TeV with the ATLAS detector. *Eur. Phys. J. C*, *76*(5), 283. doi: 10.1140/epjc/s10052-016-4050-8

Abdallah, J., et al. (2013). The optical instrumentation of the ATLAS tile calorimeter. *JINST*, *8*, P01005. doi: 10.1088/1748-0221/8/01/P01005

Abdallah, J., et al. (2021). Study of energy response and resolution of the ATLAS Tile Calorimeter to hadrons of energies from 16 to 30 GeV. *Eur. Phys. J. C*, *81*(6), 549. doi: 10.1140/epjc/s10052-021-09292-5

Abe, F., Amidei, D., Anway-Wiese, C., Apollinari, G., Atac, M., Auchincloss, P., … Zucchelli, S. (1992, Dec). Inclusive j/ψ, ψ(2s), and b-quark production in $p^{-}p$ collisions at $\sqrt{s}$ =1.8 tev. *Phys. Rev. Lett.*, *69*, 3704–3708. Retrieved from https://link.aps.org/doi/10.1103/PhysRevLett.69.3704 doi: 10.1103/PhysRevLett.69.3704

Acharya, S., et al. (2022). Prompt and non-prompt J/ψ production cross sections at midrapidity in proton-proton collisions at $\sqrt{s}$ = 5.02 and 13 TeV. *JHEP*, *03*, 190. doi: 10.1007/JHEP03(2022)190

Adragna, P., et al. (2009). Testbeam studies of production modules of the ATLAS tile calorimeter. *Nucl. Instrum. Meth. A*, *606*, 362–394. doi: 10.1016/j.nima.2009.04.009

Agostinelli, S., Allison, J., Amako, K., Apostolakis, J., Araujo, H., Arce, P., … Zschiesche, D. (2003). Geant4—a simulation toolkit. *Nuclear Instruments and Methods in Physics Research Section A: Accelerators, Spectrometers, Detectors and Associated Equipment*, *506*(3), 250-303. Retrieved from https://www.sciencedirect.com/science/article/pii/S0168900203013688 doi: https://

doi.org/10.1016/S0168-9002(03)01368-8

A.K Olive. (2006). Passage of particle through matters. *Chin. Phys. C38, 090001*.

ALICE Collaboration. (2012). J/ψ polarization in pp collisions at $\sqrt{s} = 7$ TeV. *Phys. Rev. Lett.*, *108*, 082001. doi: 10.1103/PhysRevLett.108.082001

ALICE Collaboration. (2014). Measurement of quarkonium production at forward rapidity in pp collisions at $\sqrt{s} = 7$ TeV. *Eur. Phys. J.*, *C74*(8), 2974. doi: 10.1140/epjc/s10052 -014-2974-4

ALICE Collaboration. (2018). Measurement of the inclusive J/ψ polarization at forward rapidity in pp collisions at $\sqrt{\mathbf{s}} = \mathbf{8}$ TeV. *Eur. Phys. J.*, *C78*(7), 562. doi: 10.1140/epjc/s10052 -018-6027-2

Allison, J., Amako, K., Apostolakis, J., Araujo, H., Arce Dubois, P., Asai, M., … Yoshida, H. (2006). Geant4 developments and applications. *IEEE Transactions on Nuclear Science*, *53*(1), 270-278. doi: 10.1109/TNS.2006.869826

Anderson, K. J., Batkova, L., Cavalli-Sforza, M., Carli, T., Cascella, M., Davidek, T., … Zenis, T. (2008, Nov). *Calibration of ATLAS Tile Calorimeter at Electromagnetic Scale* (Tech. Rep.). Geneva: CERN. Retrieved from https://cds.cern.ch/record/1139228

Apollinari, G., et al. (Eds.). (2017). High-Luminosity Large Hadron Collider (HL-LHC): Technical Design Report V. 0.1. , *4/2017*. doi: 10.23731/CYRM-2017-004

ATLAS Collaboration. (2008). The ATLAS Experiment at the CERN Large Hadron Collider. *JINST*, *3*, S08003. doi: 10.1088/1748-0221/3/08/S08003

ATLAS Collaboration. (2014a). Measurement of χ_{c1} and χ_{c2} production with $\sqrt{s} = 7$ TeV pp collisions at ATLAS. *JHEP*, *07*, 154. doi: 10.1007/JHEP07(2014)154

ATLAS Collaboration. (2014b). Measurement of the production cross section of prompt J/ψ mesons in association with a $W^{\pm}$ boson in pp collisions at $\sqrt{s} = 7$ TeV with the ATLAS detector. *JHEP*, *04*, 172. doi: 10.1007/JHEP04(2014)172

ATLAS Collaboration. (2014c). Measurement of the production cross-section of $\psi(2S) \rightarrow J/\psi(\rightarrow \mu^+\mu^-)\pi^+\pi^-$ in pp collisions at $\sqrt{s} = 7$ TeV at ATLAS. *JHEP*, *09*, 079. doi: 10.1007/JHEP09(2014)079

ATLAS Collaboration. (2015). Observation and measurements of the production of prompt and non-prompt J/ψ mesons in association with a Z boson in pp collisions at $\sqrt{s} = 8$ TeV with the ATLAS detector. *Eur. Phys. J.*, *C75*(5), 229. doi: 10.1140/epjc/s10052-015-3406-9

ATLAS Collaboration. (2016). Measurement of the differential cross-sections of prompt and non-prompt production of J/ψ and $\psi(2S)$ in pp collisions at $\sqrt{s} = 7$ and 8 TeV with the ATLAS detector. *Eur. Phys. J. C*, *76*, 283. doi: 10.1140/epjc/s10052-016-4050-8

ATLAS Collaboration. (2017, Sep). *Technical Design Report for the Phase-II Upgrade of the ATLAS Tile Calorimeter* (Tech. Rep.). Geneva: CERN. Retrieved from https://cds.cern.ch/record/2285583

ATLAS Collaboration. (2019). *Luminosity determination in pp collisions at $\sqrt{s} = 13$ TeV using the ATLAS detector at the LHC* (Tech. Rep.).

Avoni, G., et al. (2018). The new lucid-2 detector for luminosity measurement and monitoring in atlas. *JINST*, *13*(07), P07017. doi: 10.1088/1748-0221/13/07/P07017

Barger, V., Keung, W., & Phillips, R. (1980). On ψ and production via gluons. *Physics Letters B*, *91*(2), 253-258. Retrieved from https://www.sciencedirect.com/science/article/pii/037026938090444X doi: https://doi.org/10.1016/0370-2693(80)90444-X

Bertini, H. W., & Guthrie, M. P. (1971). News item results from medium-energy intranuclear-cascade calculation. *Nuclear Physics A*, *169*(3), 670-672. Retrieved from https://www.sciencedirect.com/science/article/pii/037594747190710X doi: https://doi.org/10.1016/0375-9474(71)90710-X

Bettoni, D., & Calabrese, R. (2005). Charmonium spectroscopy. *Progress in Particle and Nuclear Physics*, *54*(2), 615-651. Retrieved from https://www.sciencedirect.com/science/article/pii/S0146641004001255 doi: https://doi.org/10.1016/j.ppnp.2004.12.001

Blanchot, G., et al. (2020). The Cesium Source Calibration and Monitoring System of the ATLAS Tile Calorimeter: Design, Construction and Results. *JINST*, *15*(03), P03017. doi: 10.1088/1748-0221/15/03/P03017

Bodwin, G. T., Braaten, E., & Lepage, G. P. (1995a). Rigorous QCD analysis of inclusive annihilation and production of heavy quarkonium. *Phys. Rev. D*, *51*, 1125–1171. ([Erratum: Phys.Rev.D 55, 5853 (1997)]) doi: 10.1103/PhysRevD.55.5853

Bodwin, G. T., Braaten, E., & Lepage, G. P. (1995b). Rigorous QCD analysis of inclusive annihilation and production of heavy quarkonium. *Phys. Rev.*, *D51*, 1125-1171. ([Erratum: Phys. Rev.D55,5853(1997)]) doi: 10.1103/PhysRevD.55.5853,10.1103/PhysRevD.51.1125

Butenschoen, M., & Kniehl, B. A. (2012). J/ψ production in NRQCD: A global analysis of

yield and polarization. *Nucl. Phys. Proc. Suppl.*, *222-224*, 151-161. doi: 10.1016/j.nuclphysbps.2012.03.016

Cacciari, M., Frixione, S., Houdeau, N., Mangano, M. L., Nason, P., et al. (2012). Theoretical predictions for charm and bottom production at the LHC. *JHEP*, *1210*, 137. doi: 10.1007/JHEP10(2012)137

Cacciari, M., Frixione, S., & Nason, P. (2001). The p(T) spectrum in heavy flavor photoproduction. *JHEP*, *0103*, 006.

Chang, C.-H. (1980). Hadronic Production of J/ψ Associated With a Gluon. *Nucl. Phys. B*, *172*, 425–434. doi: 10.1016/0550-3213(80)90175-3

Chen, A.-P., Ma, Y.-Q., & Zhang, H. (2021). *A short theoretical review of charmonium production.* arXiv. Retrieved from https://arxiv.org/abs/2109.04028 doi: 10.48550/ARXIV.2109.04028

Cho, P. L., & Leibovich, A. K. (1996). Color octet quarkonia production. *Phys. Rev. D*, *53*, 150–162. doi: 10.1103/PhysRevD.53.150

CMS Collaboration. (2012). J/ψ and ψ_{2S} production in pp collisions at $\sqrt{s} = 7$ TeV. *JHEP*, *02*, 011. doi: 10.1007/JHEP02(2012)011

CMS Collaboration. (2013). Measurement of the prompt J/ψ and $\psi(2S)$ polarizations in pp collisions at $\sqrt{s} = 7$ TeV. *Phys. Lett. B*, *727*, 381. doi: 10.1016/j.physletb.2013.10.055

CMS Collaboration. (2015). Measurement of J/ψ and $\psi(2S)$ Prompt Double-Differential Cross Sections in pp Collisions at $\sqrt{s} = 7$ TeV. *Phys. Rev. Lett.*, *114*, 191802. doi: 10.1103/PhysRevLett.114.191802

CMS Collaboration. (2018). Measurement of quarkonium production cross sections in pp collisions at $\sqrt{s} = 13$ TeV. *Phys. Lett. B*, *780*, 251. doi: 10.1016/j.physletb.2018.02.033

Di Girolamo, B., Dotti, A., Giangiobbe, V., Johansson, P., Pribyl, L., & Volpi, M. (2005). *Beamline instrumentation in the 2004 combined ATLAS testbeam* (Tech. Rep.). Geneva: CERN. Retrieved from https://cds.cern.ch/record/831497

Einhorn, M. B., & Ellis, S. D. (1975, Oct). Hadronic production of the new resonances: Probing gluon distributions. *Phys. Rev. D*, *12*, 2007–2014. Retrieved from https://link.aps.org/doi/10.1103/PhysRevD.12.2007 doi: 10.1103/PhysRevD.12.2007

Errede, S., et al. (2008, 11). The Effect of Tile Light Collection Reduction along Radius on the ATLAS Tile Calorimeter Uniformity.

F. Carrió and A. Valero. (2020). The PreProcessor module for the ATLAS Tile Calorimeter at the

HL-LHC. *Nuclear Instruments and Methods in Physics Research Section A: Accelerators, Spectrometers, Detectors and Associated Equipment*, *958*, 162487.

Faccioli, P., et al. (2010). Towards the experimental clarification of quarkonium polarization. *Eur. Phys. J. C*, *69*, 657-673.

Fritzsch, H. (1977). Producing Heavy Quark Flavors in Hadronic Collisions: A Test of Quantum Chromodynamics. *Phys. Lett. B*, *67*, 217–221. doi: 10.1016/0370-2693(77)90108-3

G. Drake. (2015). QIE12: A new High Performance ASIC for the ATLAS TileCal Upgrade. *TWEPP5*.

G. Usai. (2010). *Signal Reconstruction of the ATLAS Hadronic Tile Calorimeter: implementation and performance*. ATL-TILECAL-PROC-2010-008.

Gabriel, T., Groom, D., Job, P., Mokhov, N., & Stevenson, G. (1994). Energy dependence of hadronic activity. *Nuclear Instruments and Methods in Physics Research Section A: Accelerators, Spectrometers, Detectors and Associated Equipment*, *338*(2), 336-347. Retrieved from https://www.sciencedirect.com/science/article/pii/016890029491317X doi: https://doi.org/10.1016/0168-9002(94)91317-X

Gong, B., Lansberg, J.-P., Lorce, C., & Wang, J. (2013). Next-to-leading-order QCD corrections to the yields and polarisations of J/Psi and Upsilon directly produced in association with a Z boson at the LHC. *JHEP*, *03*, 115. doi: 10.1007/JHEP03(2013)115

Groom, D. E. (2008). Erratum to "energy flow in a hadronic cascade: Application to hadron calorimetry" [nucl. instr. and meth. a 572 (2007) 633–653]. *Nuclear Instruments and Methods in Physics Research Section A: Accelerators, Spectrometers, Detectors and Associated Equipment*, *593*(3), 638. Retrieved from https://www.sciencedirect.com/science/article/pii/S0168900208007924 doi: https://doi.org/10.1016/j.nima.2008.05.045

J. Hoff. (1999). SMQIE: The Shower Max QIE chip, Tech. Rep. FERMILAB-TM-2075. *FERMILAB-TM-2075*.

Kartvelishvili, V., Chen, J., Djobava, T., Hu, Q., Walder, J., Zakareishvili, T., & Chargeishvili, B. (2019, Sep). *Measurement of the production cross-section of J/ψ and $\psi(2S)$ mesons at high transverse momentum in pp collisions at $\sqrt{s} = 13$ TeV with the ATLAS detector* (Tech. Rep.). Geneva: CERN. Retrieved from https://cds.cern.ch/record/2689609

Krämer, M. (2001). Quarkonium production at high-energy colliders. *Progress in Particle and Nuclear Physics*, *47*(1), 141-201. Retrieved from https://www.sciencedirect.com/science/article/pii/S0146641001001545 doi: https://doi.org/10.1016/S0146-6410(01)00154-5

L. Landau. (1944). On the Energy Loss of Fast Particles by Ionization. *USSR 8 (1944) 201*.

L. Royer. (2015). FATALIC: A Dedicated Front-End ASIC for the ATLAS TileCal Upgrade. *TWEPP*.

Lansberg, J. P., & Lorce, C. (2013). Reassessing the importance of the colour-singlet contributions to direct $J/\psi + W$ production at the LHC and the Tevatron. *Phys. Lett.*, *B726*, 218-222. ([Erratum: Phys. Lett.B738,529(2014)]) doi: 10.1016/j.physletb.2013.07.059,10.1016/j.physletb.2014.10.015

LHCb Collaboration. (2012). Measurement of $\psi(2S)$ meson production in pp collisions at $\sqrt{s}$=7 TeV. *Eur. Phys. J.*, *C72*, 2100. doi: 10.1140/epjc/s10052-012-2100-4

LHCb Collaboration. (2014). Measurement of $\psi(2S)$ polarisation in pp collisions at $\sqrt{s} = 7$ TeV. *Eur. Phys. J.*, *C74*(5), 2872. doi: 10.1140/epjc/s10052-014-2872-9

Li, G., Song, M., Zhang, R.-Y., & Ma, W.-G. (2011). QCD corrections to J/ψ production in association with a W-boson at the LHC. *Phys. Rev.*, *D83*, 014001. doi: 10.1103/PhysRevD.83.014001

M. Marjanovic. (2019). ATLAS Tile calorimeter calibration and monitoring systems. *IEEE Trans. Nucl. Sci.*, *66*(7), 1228–1235. doi: 10.1109/TNS.2019.2921941

N. Pillet. (2011). FATALIC, a wide dynamic range integrated circuit for the tilecal VFE Atlas upgrade. *TWEPP*.

O. Solovyanov. (2017). Performance of the ATLAS hadronic Tile Calorimeter in Run-2 and its upgrade for the High Luminosity LHC. *EPJ Web Conf.*, *158*, 06002. doi: 10.1051/epjconf/201715806002

S. Errede et al. (2009). *The Effect of Tile Light Collection Reduction along Radius on the ATLAS Tile Calorimeter Uniformity.* ATLAS Note ATL-TILECAL-PUB-2009-005.

S. Meroli, D. Passeria, L. Servolia. (2011). Energy loss measurement for charged particles in very thin silicon layers. *JINST 6 P06013*.

Song, M., Ma, W.-G., Li, G., Zhang, R.-Y., & Guo, L. (2011). QCD corrections to J/ψ plus Z^0-boson production at the LHC. *JHEP*, *02*, 071. ([Erratum: JHEP12,010(2012)]) doi:

10.1007/JHEP12(2012)010,10.1007/JHEP02(2011)071

Spoor, M., & Mellado Garcia, B. (2015). The ATLAS Tile Calorimeter hybrid demonstrator. In *59th Annual Conference of the South African Institute of Physics* (pp. 257–262).

Wigmans, R. (2000). *Calorimetry: Energy measurement in particle physics* (Vol. 107). doi: 10.1093/oso/9780198786351.001.0001

Scientific publications made withing the scope of thesis work:

1. Title: **Upgrade of the ATLAS Hadronic Tile Calorimeter for the High Luminosity LHC**

   Author: Tamar Zakareishvili, on behalf of the ATLAS Collaboration

   Journal of Instrumentation 15(09):C09003-C09003

   DOI: 10.1088/1748-0221/15/09/C09003

2. Title: Measurement of the production cross-section of J/ψ and ψ(2S) mesons at high transverse momentum in pp collisions at √s = 13 TeV with the ATLAS detector

   Author: Tamar Zakareishvili, on behalf of the ATLAS Collaboration

   J.Phys.Conf.Ser. 1690 (2020) 1, 012160

   DOI: 10.1088/1742-6596/1690/1/012160

3. Title: **Study of energy response and resolution of the ATLAS Tile Calorimeter to hadrons of energies from 16 to 30 GeV**

   Authors: Jalal Abdallah,..., Tamar Zakareishvili,..., Pedro Diego Zuccarello

   The European Physical Journal C volume 81, Article number: 549 (2021)

   DOI: 10.1140/epjc/s10052-021-09292-5

4. Title: Charmonium production in pp collisions at the LHC

   Author: T. Zakareishvili

   Proceedings of Science - PoS Regio2021 (2022) 004

   DOI: 10.22323/1.412.0004

Appendices

Appendix A

Fit model details

Fit model and parameters

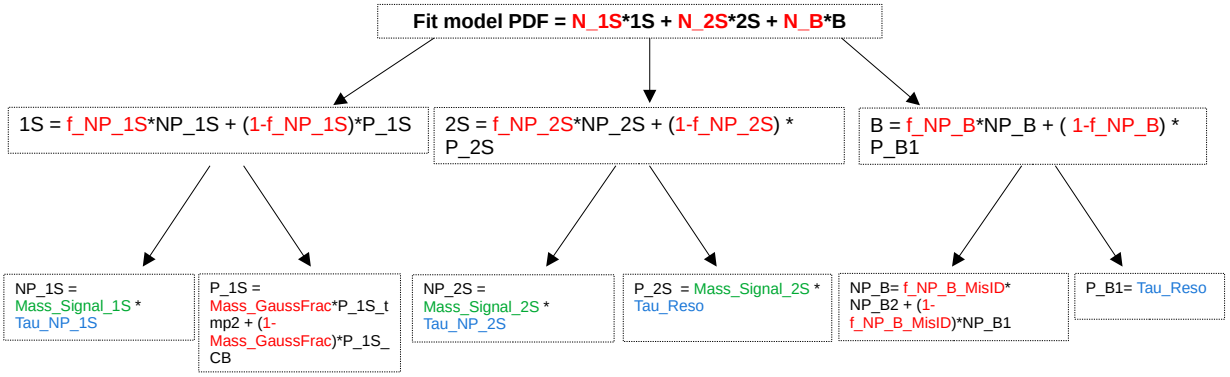

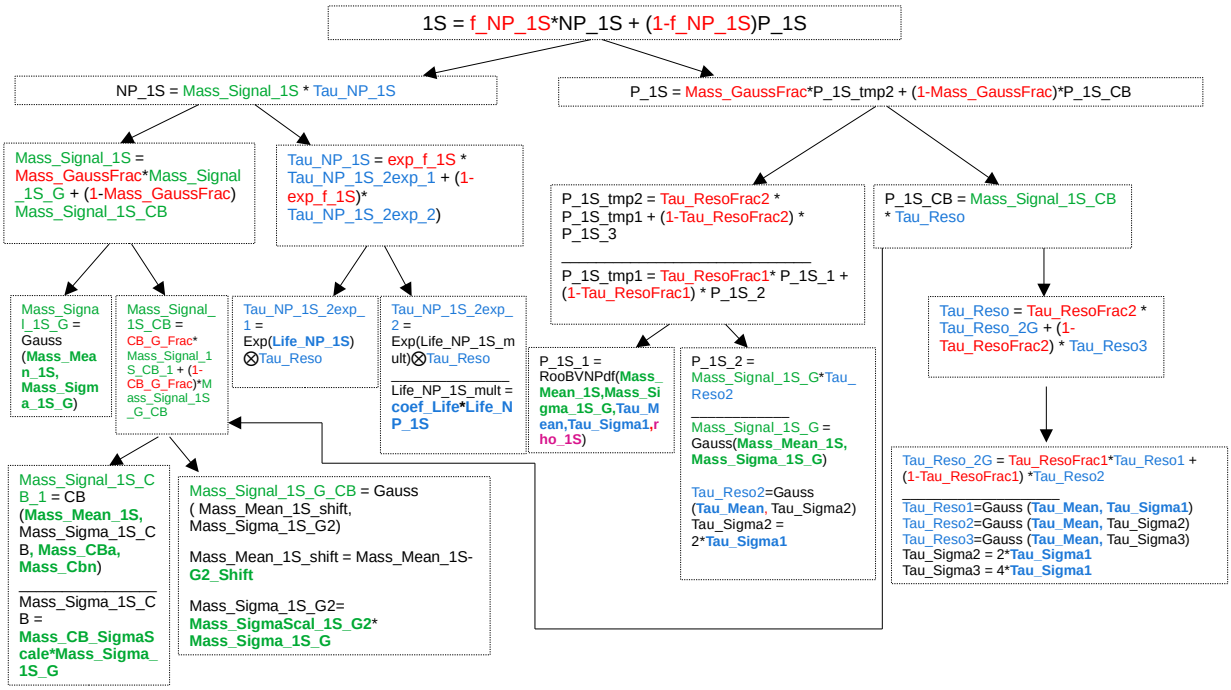

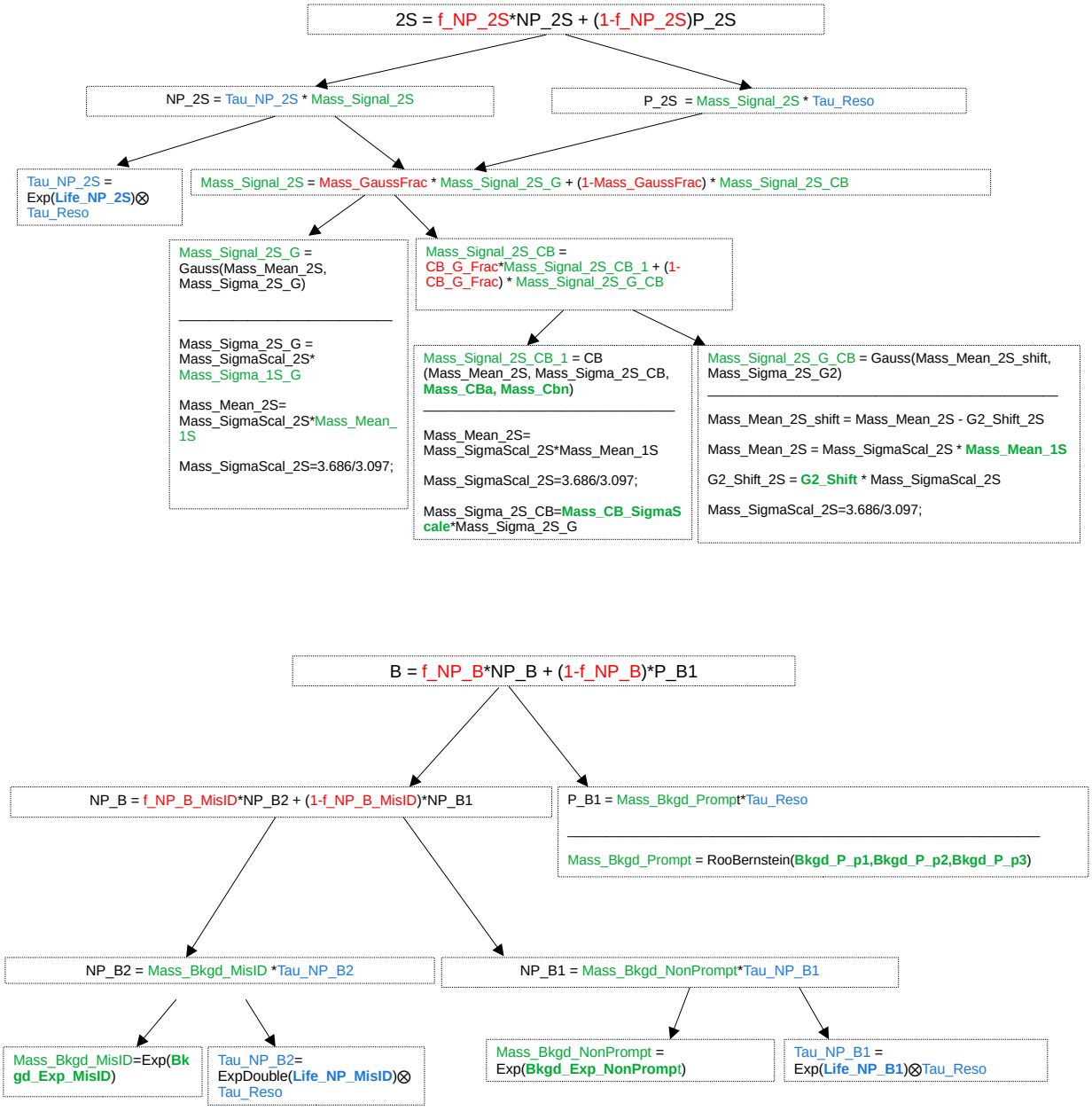
2S = f_NP_2S*NP_2S + (1-f_NP_2S)P_2S
NP_2S = Tau_NP_2S * Mass_Signal_2S
P_2S = Mass_Signal_2S * Tau_Reso
Tau_NP_2S = Exp(Life_NP_2S)⊗ Tau_Reso
Mass_Signal_2S = Mass_GaussFrac * Mass_Signal_2S_G + (1-Mass_GaussFrac) * Mass_Signal_2S_CB
Mass_Signal_2S_G = Gauss(Mass_Mean_2S, Mass_Sigma_2S_G)
Mass_Sigma_2S_G = Mass_SigmaScal_2S* Mass_Sigma_1S_G
Mass_Mean_2S= Mass_SigmaScal_2S*Mass_Mean_1S
Mass_SigmaScal_2S=3.686/3.097;
Mass_Signal_2S_CB = CB_G_Frac*Mass_Signal_2S_CB_1 + (1-CB_G_Frac) * Mass_Signal_2S_G_CB
Mass_Signal_2S_CB_1 = CB (Mass_Mean_2S, Mass_Sigma_2S_CB, Mass_CBa, Mass_Cbn)
Mass_Mean_2S= Mass_SigmaScal_2S*Mass_Mean_1S
Mass_SigmaScal_2S=3.686/3.097;
Mass_Sigma_2S_CB=Mass_CB_SigmaScale*Mass_Sigma_2S_G
Mass_Signal_2S_G_CB = Gauss(Mass_Mean_2S_shift, Mass_Sigma_2S_G2)
Mass_Mean_2S_shift = Mass_Mean_2S - G2_Shift_2S
Mass_Mean_2S = Mass_SigmaScal_2S * Mass_Mean_1S
G2_Shift_2S = G2_Shift * Mass_SigmaScal_2S
Mass_SigmaScal_2S=3.686/3.097;

B = f_NP_B*NP_B + (1-f_NP_B)*P_B1
NP_B = f_NP_B_MisID*NP_B2 + (1-f_NP_B_MisID)*NP_B1
P_B1 = Mass_Bkgd_Prompt*Tau_Reso
Mass_Bkgd_Prompt = RooBernstein(Bkgd_P_p1,Bkgd_P_p2,Bkgd_P_p3)
NP_B2 = Mass_Bkgd_MisID *Tau_NP_B2
NP_B1 = Mass_Bkgd_NonPrompt*Tau_NP_B1
Mass_Bkgd_MisID=Exp(Bkgd_Exp_MisID)
Tau_NP_B2= ExpDouble(Life_NP_MisID)⊗ Tau_Reso
Mass_Bkgd_NonPrompt = Exp(Bkgd_Exp_NonPrompt)
Tau_NP_B1 = Exp(Life_NP_B1)⊗Tau_Reso

Appendix B

Tables of 2D χ^2/ndf

p_T [GeV]	0.00 <|y|< 0.75		0.75 <|y|< 1.50		1.50 <|y|< 2.00	
	χ^2/ndf	Prob.	χ^2/ndf	Prob.	χ^2/ndf	Prob.
8 - 8.1	0.768	1	0.752	1	0.836	1
8.1 - 8.2	0.811	1	0.802	1	0.825	1
8.2 - 8.3	0.836	1	0.827	1	0.839	1
8.3 - 8.4	0.855	1	0.83	1	0.861	1
8.4 - 8.5	0.902	1	0.847	1	0.83	1
8.5 - 8.6	0.873	1	0.828	1	0.916	1
8.6 - 8.7	0.966	0.901	0.882	1	0.92	1
8.7 - 8.8	0.941	0.995	0.852	1	0.91	1
8.8 - 8.9	0.969	0.889	0.844	1	0.971	0.855
8.9 - 9	0.921	1	0.85	1	0.924	1
9 - 9.1	0.938	0.998	0.905	1	0.974	0.832
9.1 - 9.2	0.954	0.978	0.87	1	0.934	0.999
9.2 - 9.3	0.964	0.934	0.886	1	0.962	0.939
9.3 - 9.4	0.952	0.983	0.917	1	0.923	1
9.4 - 9.5	0.943	0.995	0.92	1	0.919	1
9.5 - 9.6	0.969	0.896	0.938	0.997	0.981	0.739
9.6 - 9.7	0.955	0.978	0.923	1	0.977	0.803
9.7 - 9.8	0.999	0.408	0.911	1	0.943	0.995
9.8 - 9.9	0.953	0.983	0.935	0.998	0.996	0.471
9.9 - 10	0.923	1	0.986	0.662	0.931	0.999

p_T [GeV]	0.00 <|y|< 0.75		0.75 <|y|< 1.50		1.50 <|y|< 2.00	
	χ^2/ndf	Prob.	χ^2/ndf	Prob.	χ^2/ndf	Prob.
10 - 10.1	0.938	0.998	0.967	0.912	0.967	0.917
10.1 - 10.2	0.922	1	0.909	1	0.961	0.955
10.2 - 10.3	0.949	0.99	0.93	1	1.014	0.168
10.3 - 10.4	0.973	0.868	0.993	0.534	0.974	0.851
10.4 - 10.5	0.959	0.964	0.923	1	0.975	0.837
10.5 - 10.6	0.921	1	0.951	0.986	0.949	0.99
10.6 - 10.7	0.972	0.873	0.921	1	0.923	1
10.7 - 10.8	0.912	1	0.928	1	0.992	0.559
10.8 - 10.9	1	0.383	0.926	1	0.972	0.868
10.9 - 11	0.933	0.999	0.942	0.996	0.959	0.964
11 - 11.1	0.937	0.998	0.939	0.998	0.952	0.985
11.1 - 11.2	0.955	0.979	0.931	0.999	0.951	0.987
11.2 - 11.3	0.952	0.985	0.939	0.997	0.938	0.998
11.3 - 11.4	0.937	0.998	0.934	0.999	0.937	0.998
11.4 - 11.5	0.936	0.999	0.929	1	0.947	0.992
11.5 - 11.6	0.986	0.668	0.916	1	0.941	0.997
11.6 - 11.7	1.001	0.371	0.924	1	0.909	1
11.7 - 11.8	0.939	0.998	0.951	0.986	0.982	0.739
11.8 - 11.9	0.914	1	0.913	1	0.957	0.971
11.9 - 12	0.949	0.988	0.934	0.999	0.98	0.765
12 - 12.1	0.957	0.968	0.861	1	0.931	0.999
12.1 - 12.2	0.931	0.999	0.94	0.997	0.963	0.942
12.2 - 12.3	0.964	0.936	0.928	1	0.92	1
12.3 - 12.4	0.921	1	0.934	0.999	0.924	1
12.4 - 12.5	0.938	0.998	0.897	1	0.95	0.986
12.5 - 12.6	0.935	0.998	0.911	1	0.933	0.999
12.6 - 12.7	0.931	0.999	0.928	1	0.956	0.968
12.7 - 12.8	0.882	1	0.875	1	0.892	1
12.8 - 12.9	0.899	1	0.912	1	0.882	1
12.9 - 13	0.915	1	0.891	1	0.915	1

p_T [GeV]	0.00 <|y|< 0.75		0.75 <|y|< 1.50		1.50 <|y|< 2.00	
	χ^2/ndf	Prob.	χ^2/ndf	Prob.	χ^2/ndf	Prob.
13 - 13.2	0.975	0.87	1.001	0.38	0.999	0.427
13.2 - 13.4	0.961	0.969	0.985	0.716	1.015	0.148
13.4 - 13.6	0.974	0.869	0.972	0.902	0.961	0.966
13.6 - 13.8	0.988	0.654	0.962	0.963	0.962	0.959
13.8 - 14	0.99	0.601	0.95	0.992	0.966	0.94
14 - 14.2	0.986	0.675	0.953	0.988	0.977	0.826
14.2 - 14.4	0.981	0.763	0.999	0.419	0.939	0.998
14.4 - 14.6	0.967	0.931	0.966	0.938	0.932	1
14.6 - 14.8	0.932	1	0.946	0.996	0.993	0.539
14.8 - 15	0.914	1	0.963	0.953	0.942	0.997
15 - 15.2	0.925	1	0.939	0.998	0.938	0.998
15.2 - 15.4	0.998	0.438	0.953	0.985	0.957	0.973
15.4 - 15.6	0.932	0.999	0.956	0.977	0.923	1
15.6 - 15.8	0.949	0.99	0.926	1	0.91	1
15.8 - 16	0.927	1	0.958	0.969	0.879	1
16 - 16.2	0.914	1	0.966	0.928	0.958	0.962
16.2 - 16.4	0.934	0.999	0.968	0.914	0.92	1
16.4 - 16.6	0.918	1	0.901	1	0.896	1
16.6 - 16.8	0.892	1	0.955	0.974	0.954	0.972
16.8 - 17	0.944	0.993	0.911	1	0.953	0.976
17 - 17.2	0.879	1	0.905	1	0.904	1
17.2 - 17.4	0.887	1	0.88	1	0.929	0.999
17.4 - 17.6	0.879	1	0.918	1	0.919	1
17.6 - 17.8	0.873	1	0.9	1	0.903	1
17.8 - 18	0.883	1	0.919	1	0.925	0.999
18 - 18.2	0.839	1	0.883	1	0.898	1
18.2 - 18.4	0.903	1	0.94	0.995	0.888	1
18.4 - 18.6	0.861	1	0.906	1	0.906	1
18.6 - 18.8	0.859	1	0.859	1	0.862	1
18.8 - 19	0.817	1	0.876	1	0.825	1

2 p_T [GeV]	0.00 <|y|< 0.75		0.75 <|y|< 1.50		1.50 <|y|< 2.00	
	χ^2/ndf	Prob.	χ^2/ndf	Prob.	χ^2/ndf	Prob.
19 - 19.2	0.821	1	0.849	1	0.889	1
19.2 - 19.4	0.883	1	0.839	1	0.84	1
19.4 - 19.6	0.832	1	0.87	1	0.88	1
19.6 - 19.8	0.82	1	0.901	1	0.822	1
19.8 - 20	0.851	1	0.853	1	0.854	1
20 - 20.4	0.928	1	0.937	0.998	0.986	0.652
20.4 - 20.8	0.91	1	0.913	1	0.909	1
20.8 - 21.2	0.927	0.999	0.94	0.996	0.893	1
21.2 - 21.6	0.863	1	0.914	1	0.849	1
21.6 - 22	0.864	1	0.924	1	0.915	1
22 - 22.4	0.848	1	0.899	1	0.855	1
22.4 - 22.8	0.85	1	0.895	1	0.85	1
22.8 - 23.2	0.909	1	0.874	1	0.863	1
23.2 - 23.6	0.833	1	0.891	1	0.834	1
23.6 - 24	0.844	1	0.859	1	0.82	1
24 - 24.4	0.857	1	0.887	1	0.795	1
24.4 - 24.8	0.832	1	0.875	1	0.905	1
24.8 - 25.2	0.803	1	0.806	1	0.846	1
25.2 - 25.6	0.853	1	0.872	1	0.854	1
25.6 - 26	0.777	1	0.88	1	0.772	1
26 - 26.4	0.796	1	0.789	1	0.839	1
26.4 - 26.8	0.841	1	0.816	1	0.772	1
26.8 - 27.2	0.804	1	0.811	1	0.82	1
27.2 - 27.6	0.842	1	0.851	1	0.793	1
27.6 - 28	0.792	1	0.828	1	0.814	1
28 - 28.4	0.799	1	0.865	1	0.823	1
28.4 - 28.8	0.765	1	0.796	1	0.769	1
28.8 - 29.2	0.802	1	0.775	1	0.816	1
29.2 - 29.6	0.781	1	0.824	1	0.834	1
29.6 - 30	0.777	1	0.797	1	0.823	1

p_T [GeV]	0.00 <|y|< 0.75		0.75 <|y|< 1.50		1.50 <|y|< 2.00	
	χ^2/ndf	Prob.	χ^2/ndf	Prob.	χ^2/ndf	Prob.
30 - 31	0.826	1	0.816	1	0.855	1
31 - 32	0.83	1	0.832	1	0.85	1
32 - 33	0.818	1	0.842	1	0.879	1
33 - 34	0.781	1	0.859	1	0.806	1
34 - 35	0.825	1	0.875	1	0.839	1
35 - 40	0.883	1	0.917	1	0.887	1
40 - 45	0.811	1	0.839	1	0.832	1
45 - 50	0.822	1	0.808	1	0.793	1
50 - 55	0.812	1	0.794	1	0.78	1
55 - 60	0.815	1	0.778	1	0.77	1
60 - 70	1.086	3.8e-07	1.018	0.103	0.916	1
70 - 80	1.037	0.012	1	0.399	0.901	1
80 - 90	1.015	0.147	0.992	0.561	0.95	0.983
90 - 100	0.991	0.567	0.946	0.992	0.876	1
100 - 120	0.95	0.987	1.024	0.077	0.918	0.999
120 - 140	0.916	0.999	0.915	0.999	0.883	1
140 - 160	0.776	1	0.867	1	0.798	1
160 - 180	0.821	1	0.814	1	0.719	1
180 - 200	0.741	1	0.713	1	0.733	1
200 - 250	0.727	1	0.786	1	0.864	0.839
250 - 300	0.669	1	0.775	0.994	0.77	0.849
300 - 360	0.716	0.95	0.62	0.986	0.623	0.494

Table B.1: Two dimensional χ^2 / ndf and Probability values.

Appendix C

Fit systematics

There are 14 different variations of the fit model. They are obtained by releasing parameters that were fixed for the nominal variation, one at-a-time.

In this section the results of various fit variations are shown, relative to the nominal fit result at zero. Each figure corresponds to one rapidity slice and one (of eight) measured quantity.

There are 14 fit variations overall, in addition to the nominal fit, which corresponds to zero on vertical axis. The variations are:

1. **CB**α. The value of the Crystal Ball parameter α was released.
2. **CB**n. The value of the Crystal Ball parameter n was released.
3. **CB scale factor**. The value of the Crystal Ball scale factor was released.
4. **Tau resolution** σ. The value σ of the narrowest Gaussian in lifetime resolution was changed from 0.004 to 0.003.
5. **Tau resolution** μ. The common centre of the three Gaussian in lifetime resolution was released.
6. $\psi(2S)$ **NP fraction**. The fixed value of $\psi(2S)$ non-prompt fraction in the p_{T} bins above 140 GeV is changed from 0.7 to 0.6.
7. $\psi(2S)$ **to** J/ψ σ **scale**. The value of width scale factor between J/ψ and $\psi(2S)$, fixed to their mass ratio, was released.
8. $\psi(2S)$ **to** J/ψ μ **scale**. The value of mass scale factor between J/ψ and $\psi(2S)$, fixed to their mass ratio, was released.

9. $\psi(2S)$ **scale factor at high** $p_{\mathbf{T}}$. The fixed value of $\psi(2S)$ to J/ψ cross section ratio in the p_{T} bins above 140 GeV is changed from 0.07 to 0.06.

10. **Correlation** $\rho = 0$. The value of the correlation factor between the narrowest Gaussians in mass and lifetime was changed from nominal 0.3 to zero.

11. **Tau resolution scale factors**. The values of scale factors between the widths of the three Gaussians in lifetime resolution was changed from 2 and 4 to 3 and 5.

12. **Mass bkg Model 1**. The background model for non-prompt background was changed from the Bernstein polynomials to an exponential.

13. **Mass bkg Model 2**. The background model for prompt background was changed from an exponential to Bernstein polynomials.

14. $\psi(2S)$ **2nd exp.**. A second exponential was added to the lifetime distribution of $\psi(2S)$.

In each analysis bin, the maximum deviation from nominal yield was established among the 14 deviations, and that maximum deviation was divided by $\sqrt{3}$ and used as an effective symmetric "sigma" for the fit variation systematics. This is a more conservative (and explicitly symmetric) estimate compared to the r.m.s. value between the variations.

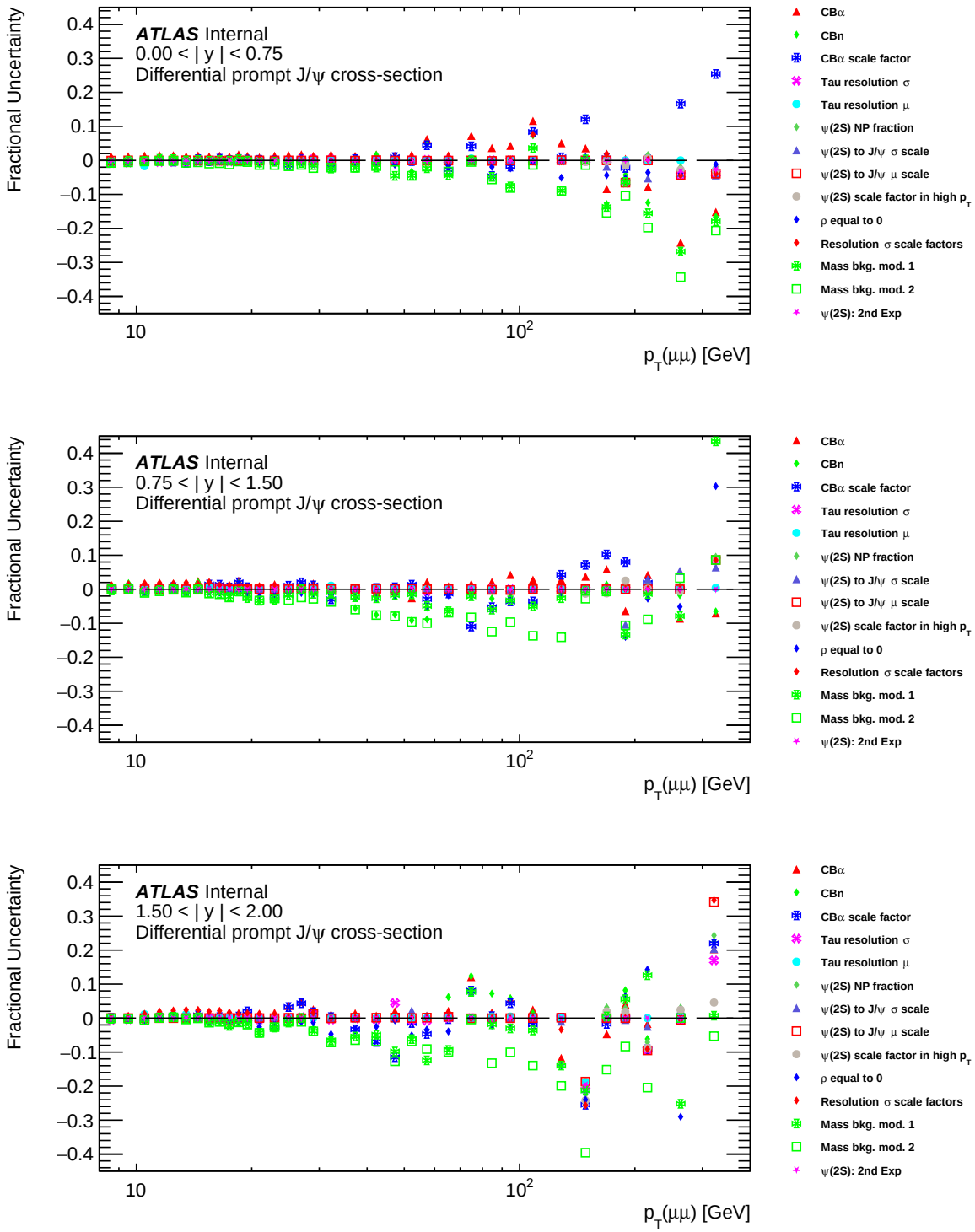

Figure C.1: The differential prompt J/ψ cross-section in rapidity slices

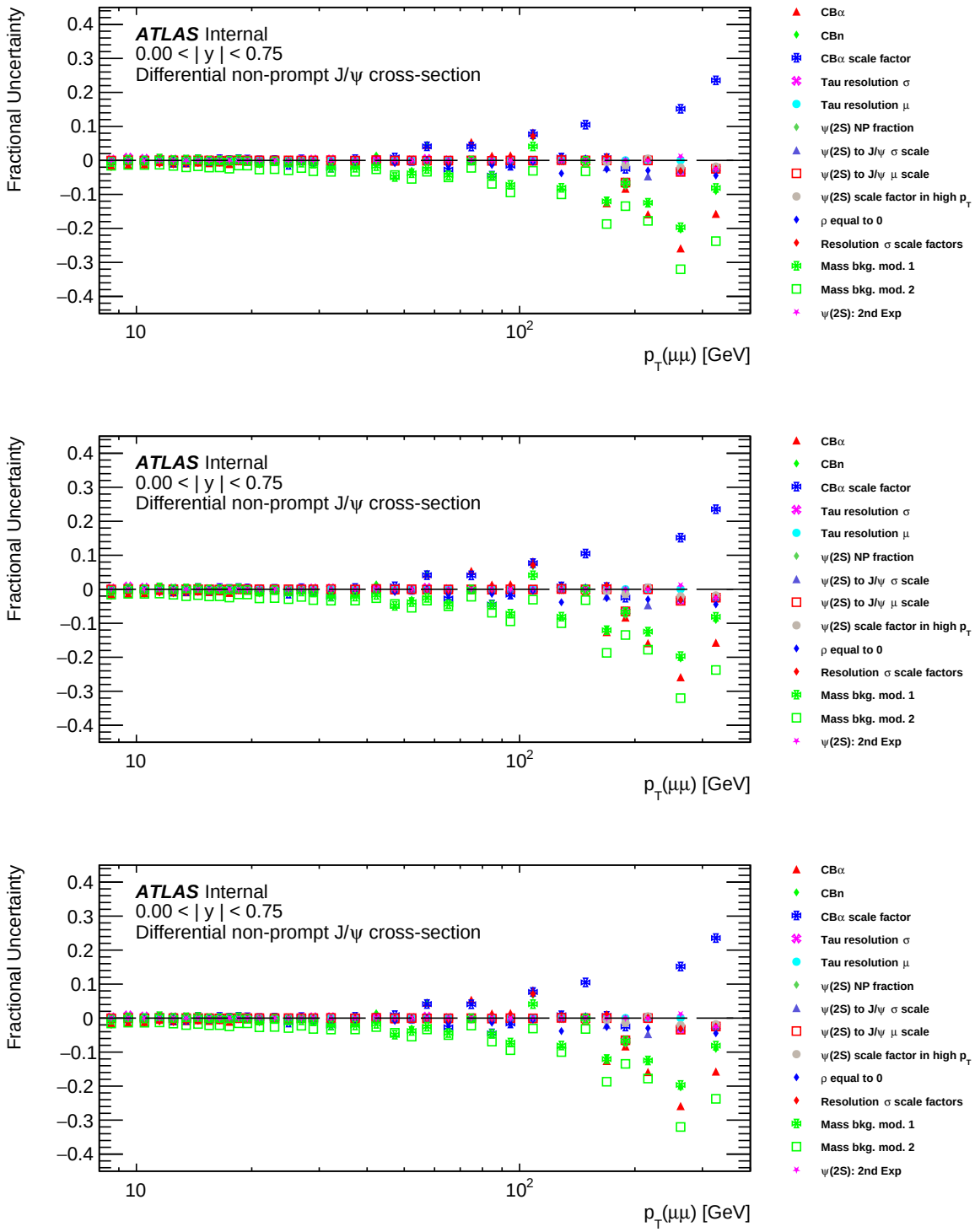

Figure C.2: The differential non-prompt J/ψ cross-section in rapidity slices

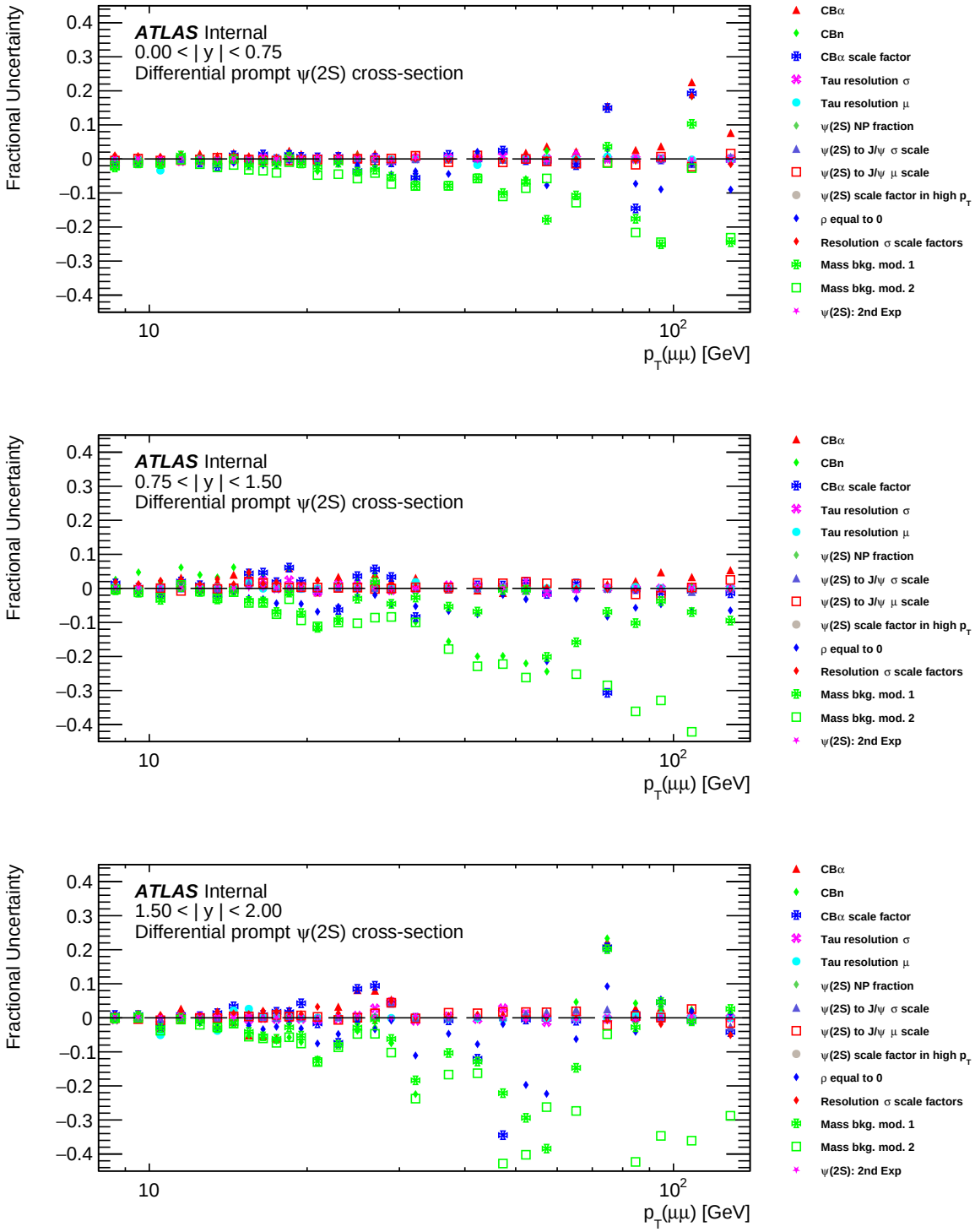

Figure C.3: The differential prompt $\psi(2S)$ cross-section in rapidity slices

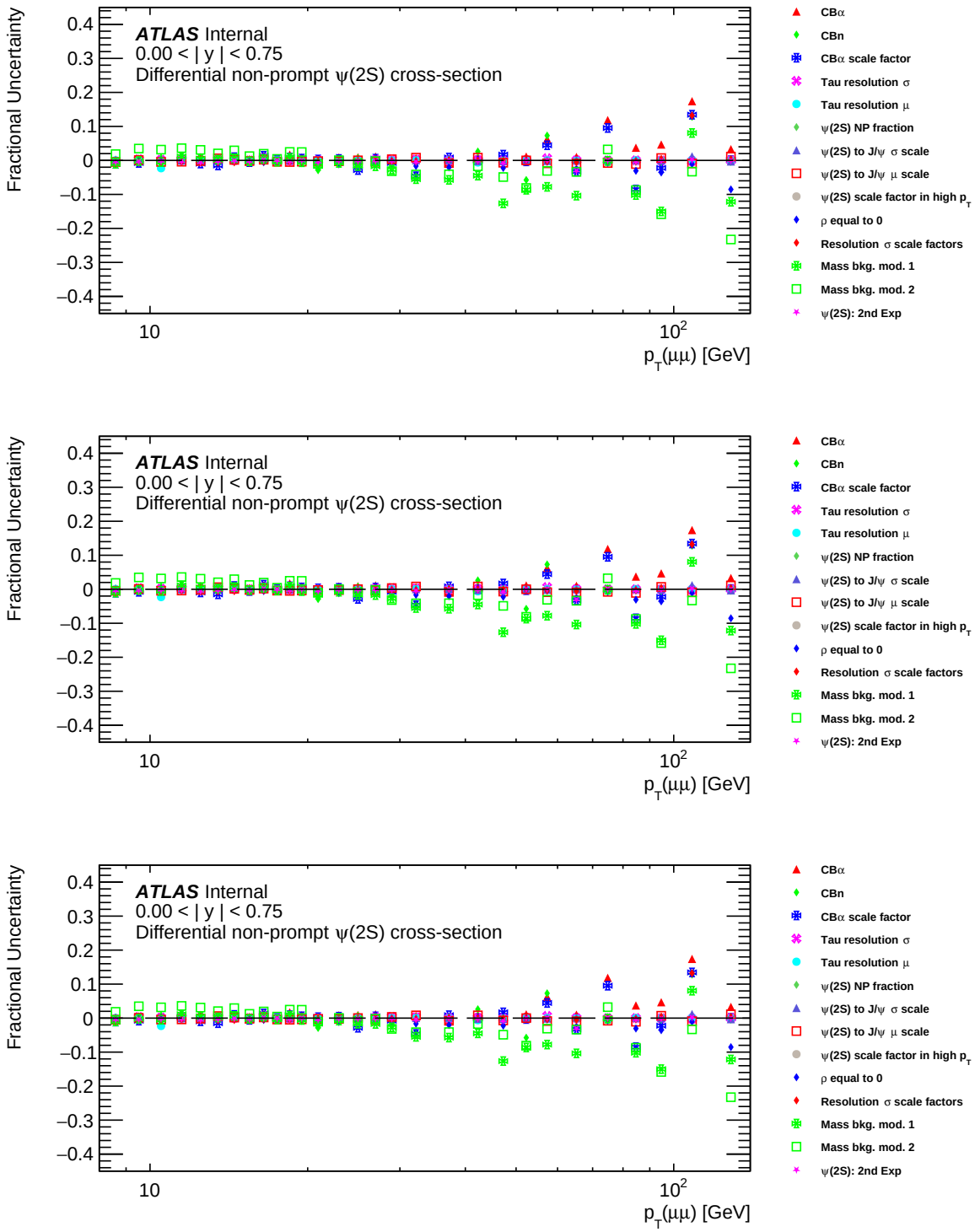

Figure C.4: The differential non-prompt $\psi(2S)$ cross-section in rapidity slices

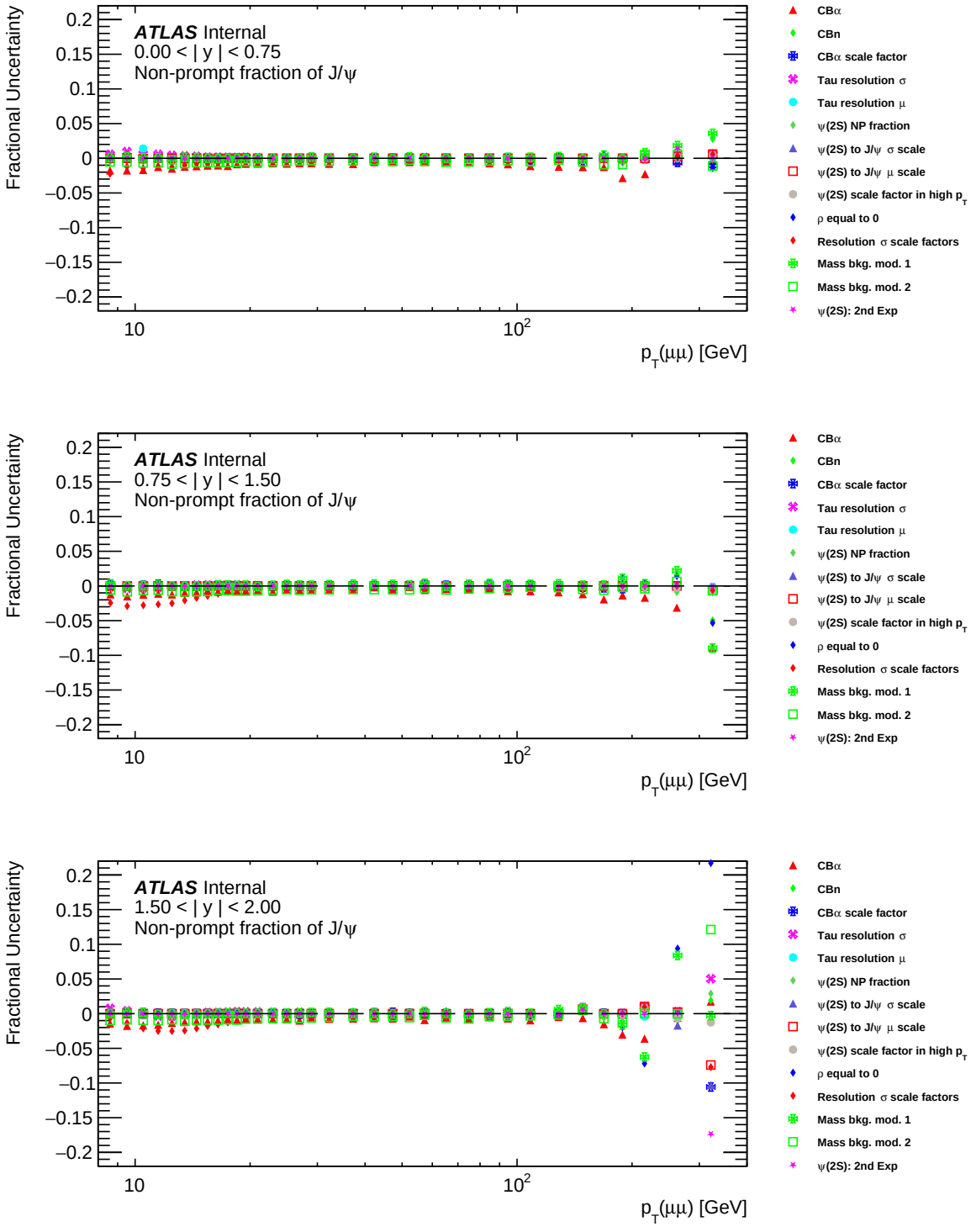

Figure C.5: The non-prompt fraction J/ψ in rapidity slices

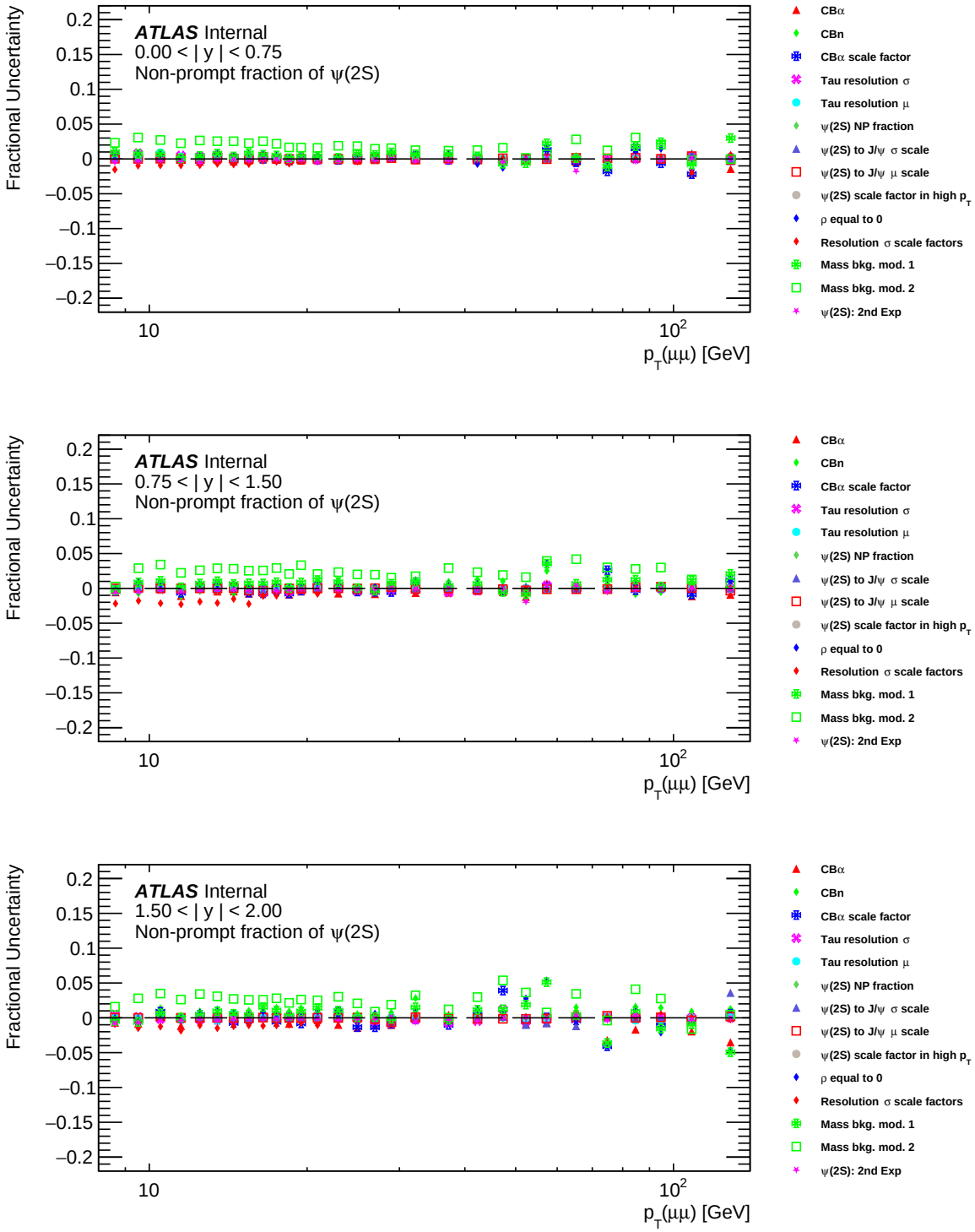

Figure C.6: The non-prompt fraction $\psi(2S)$ in rapidity slices

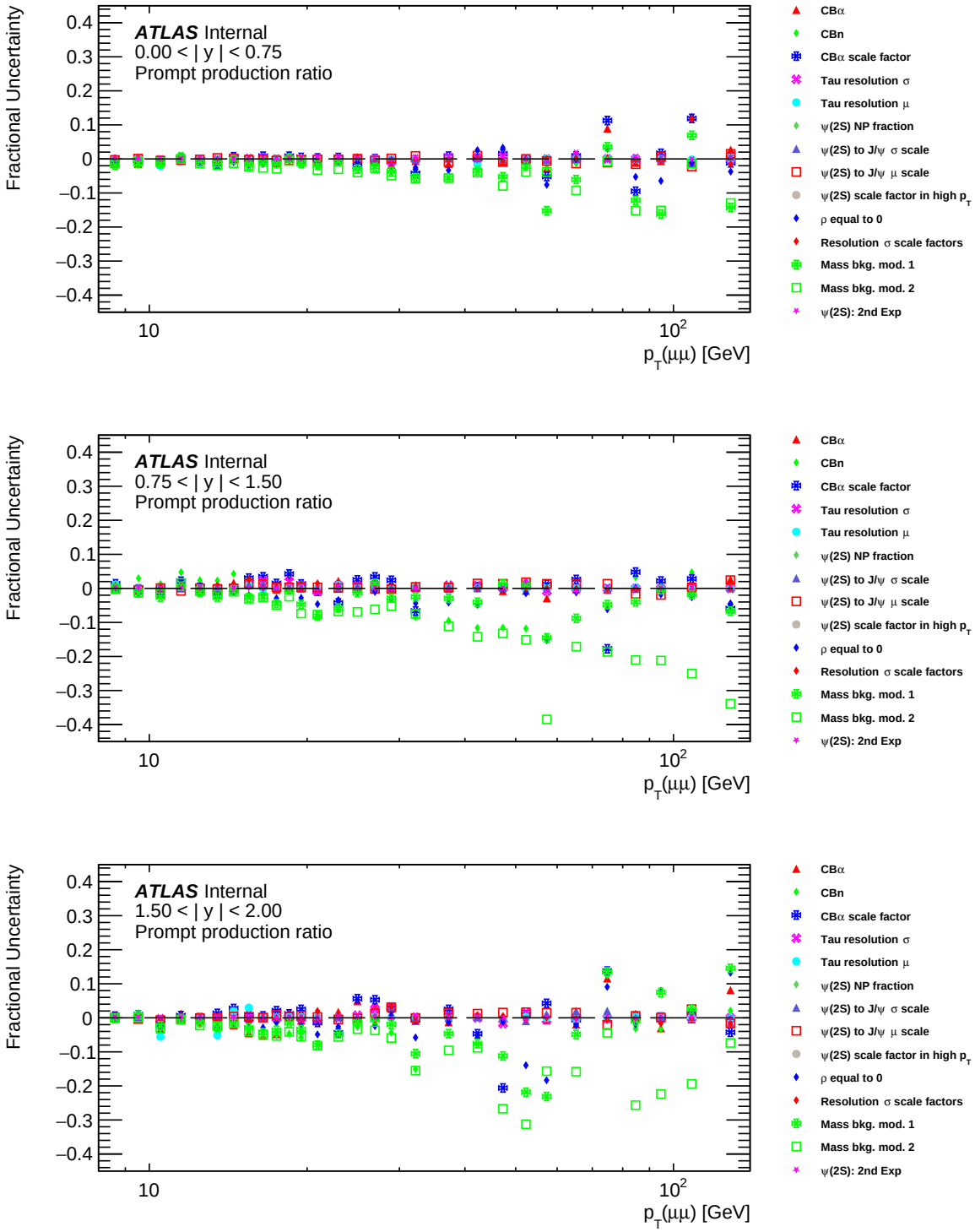

Figure C.7: Prompt production ratio

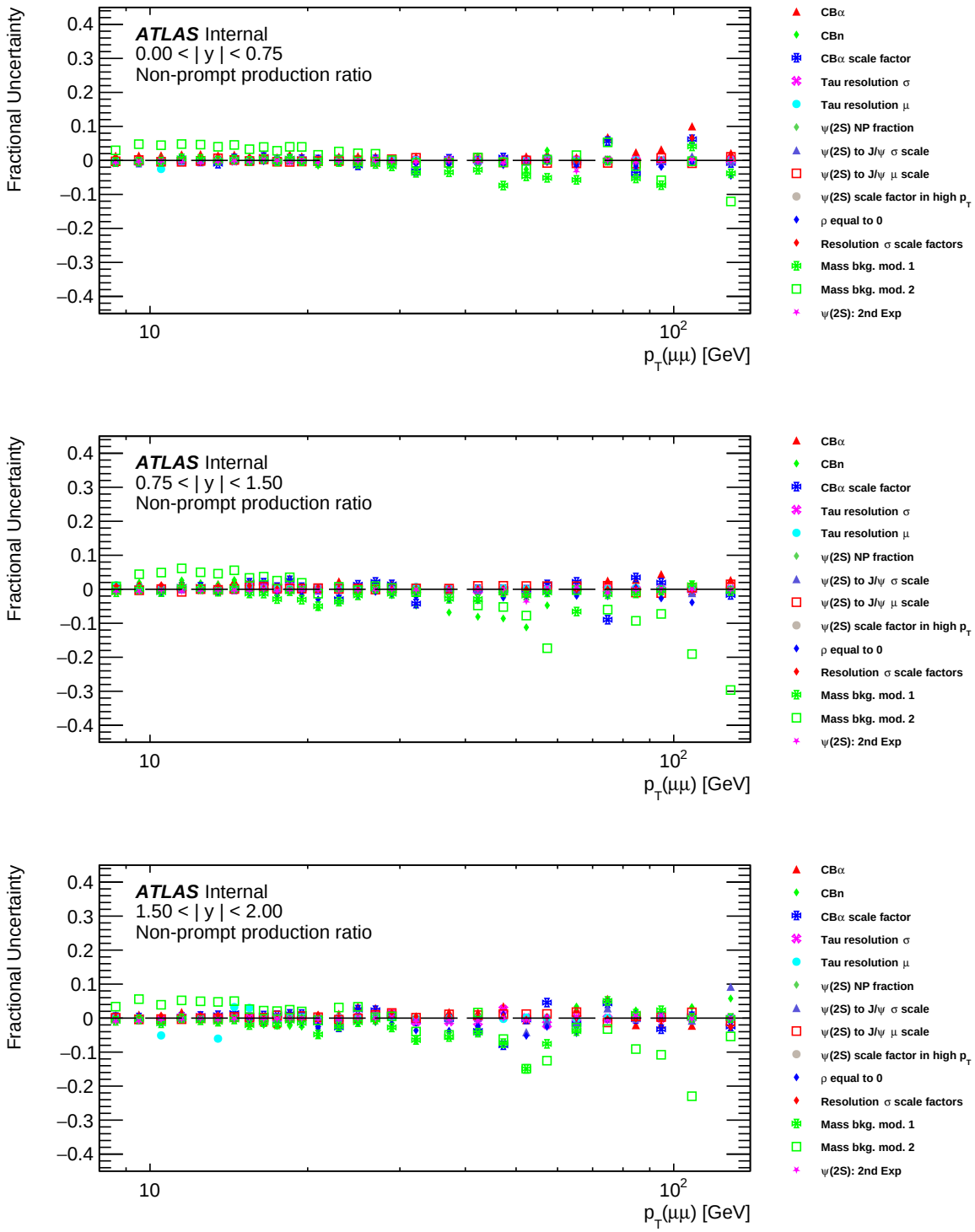

Figure C.8: Non-prompt production ratio

Appendix D

Spin alignment corrections

p_T	0.00 <|y|< 0.75	0.75 <|y|< 1.50	1.50 <|y|< 2.00
8 - 9 [GeV]	0.671	0.69	0.707
9 - 10 [GeV]	0.676	0.692	0.703
10 - 11 [GeV]	0.686	0.698	0.703
11 - 12 [GeV]	0.695	0.703	0.707
12 - 13 [GeV]	0.703	0.71	0.715
13 - 14 [GeV]	0.71	0.718	0.721
14 - 15 [GeV]	0.719	0.725	0.728
15 - 16 [GeV]	0.727	0.733	0.735
16 - 17 [GeV]	0.734	0.739	0.744
17 - 18 [GeV]	0.742	0.746	0.748
18 - 19 [GeV]	0.748	0.753	0.755
19 - 20 [GeV]	0.756	0.76	0.761
20 - 22 [GeV]	0.766	0.769	0.771
22 - 24 [GeV]	0.779	0.782	0.782
24 - 26 [GeV]	0.79	0.792	0.793
26 - 28 [GeV]	0.8	0.801	0.802
28 - 30 [GeV]	0.809	0.81	0.811
30 - 35 [GeV]	0.823	0.824	0.824
35 - 40 [GeV]	0.84	0.841	0.841
40 - 45 [GeV]	0.855	0.855	0.856
45 - 50 [GeV]	0.867	0.867	0.868
50 - 55 [GeV]	0.878	0.878	0.878
55 - 60 [GeV]	0.886	0.887	0.887
60 - 70 [GeV]	1.487	1.482	1.481
70 - 80 [GeV]	1.191	1.193	1.192
80 - 90 [GeV]	1.052	1.053	1.055
90 - 100 [GeV]	0.976	0.978	0.979
100 - 120 [GeV]	0.939	0.939	0.939
120 - 140 [GeV]	0.945	0.945	0.945
140 - 160 [GeV]	0.952	0.952	0.952
160 - 180 [GeV]	0.958	0.958	0.958
180 - 200 [GeV]	0.962	0.962	0.961
200 - 240 [GeV]	0.967	0.968	0.968
240 - 300 [GeV]	0.974	0.973	0.973
300 - 360 [GeV]	0.977	0.979	0.977

Table D.1: Mean weight correction factor for J/ψ under the "longitudinal" spin-alignement hypothesis.

p_T	0.00 <|y|< 0.75	0.75 <|y|< 1.50	1.50 <|y|< 2.00
8 - 9 [GeV]	1.32	1.287	1.283
9 - 10 [GeV]	1.301	1.277	1.267
10 - 11 [GeV]	1.298	1.272	1.264
11 - 12 [GeV]	1.287	1.262	1.254
12 - 13 [GeV]	1.269	1.254	1.249
13 - 14 [GeV]	1.259	1.244	1.242
14 - 15 [GeV]	1.245	1.236	1.231
15 - 16 [GeV]	1.235	1.225	1.222
16 - 17 [GeV]	1.222	1.214	1.214
17 - 18 [GeV]	1.21	1.203	1.202
18 - 19 [GeV]	1.201	1.195	1.193
19 - 20 [GeV]	1.191	1.189	1.186
20 - 22 [GeV]	1.18	1.177	1.175
22 - 24 [GeV]	1.167	1.165	1.163
24 - 26 [GeV]	1.154	1.152	1.15
26 - 28 [GeV]	1.143	1.141	1.142
28 - 30 [GeV]	1.133	1.131	1.131
30 - 35 [GeV]	1.121	1.12	1.119
35 - 40 [GeV]	1.105	1.104	1.103
40 - 45 [GeV]	1.092	1.092	1.092
45 - 50 [GeV]	1.082	1.083	1.083
50 - 55 [GeV]	1.075	1.075	1.074
55 - 60 [GeV]	1.068	1.068	1.068
60 - 70 [GeV]	0.86	0.86	0.861
70 - 80 [GeV]	0.926	0.925	0.926
80 - 90 [GeV]	0.976	0.976	0.975
90 - 100 [GeV]	1.012	1.011	1.011
100 - 120 [GeV]	1.034	1.034	1.034
120 - 140 [GeV]	1.03	1.03	1.03
140 - 160 [GeV]	1.026	1.026	1.026
160 - 180 [GeV]	1.023	1.023	1.022
180 - 200 [GeV]	1.02	1.02	1.02
200 - 240 [GeV]	1.018	1.017	1.017
240 - 300 [GeV]	1.013	1.015	1.014
300 - 360 [GeV]	1.012	1.011	0.011

Table D.2: Mean weight correction factor for J/ψ under the "transverse zero" spin-alignement hypothesis.

p_T	0.00 <|y|< 0.75	0.75 <|y|< 1.50	1.50 <|y|< 2.00
8 - 9 [GeV]	1.553	1.568	1.595
9 - 10 [GeV]	1.395	1.42	1.424
10 - 11 [GeV]	1.346	1.358	1.36
11 - 12 [GeV]	1.317	1.322	1.318
12 - 13 [GeV]	1.299	1.295	1.294
13 - 14 [GeV]	1.277	1.275	1.277
14 - 15 [GeV]	1.261	1.26	1.258
15 - 16 [GeV]	1.247	1.249	1.246
16 - 17 [GeV]	1.233	1.234	1.237
17 - 18 [GeV]	1.221	1.22	1.22
18 - 19 [GeV]	1.208	1.209	1.21
19 - 20 [GeV]	1.199	1.199	1.198
20 - 22 [GeV]	1.187	1.187	1.186
22 - 24 [GeV]	1.171	1.171	1.17
24 - 26 [GeV]	1.158	1.157	1.159
26 - 28 [GeV]	1.146	1.146	1.148
28 - 30 [GeV]	1.136	1.136	1.135
30 - 35 [GeV]	1.124	1.123	1.124
35 - 40 [GeV]	1.106	1.107	1.106
40 - 45 [GeV]	1.094	1.094	1.094
45 - 50 [GeV]	1.084	1.084	1.084
50 - 55 [GeV]	1.076	1.076	1.076
55 - 60 [GeV]	1.068	1.069	1.069
60 - 70 [GeV]	0.86	0.861	0.861
70 - 80 [GeV]	0.928	0.927	0.928
80 - 90 [GeV]	0.978	0.978	0.977
90 - 100 [GeV]	1.014	1.012	1.012
100 - 120 [GeV]	1.034	1.034	1.034
120 - 140 [GeV]	1.03	1.03	1.03
140 - 160 [GeV]	1.026	1.026	1.026
160 - 180 [GeV]	1.023	1.023	1.023
180 - 200 [GeV]	1.02	1.02	1.02
200 - 240 [GeV]	1.018	1.017	1.017
240 - 300 [GeV]	1.014	1.013	1.014
300 - 360 [GeV]	1.011	1.011	1.011

Table D.3: Mean weight correction factor for J/ψ under the "transverse positive" spin-alignement hypothesis.

p_T	0.00 <|y|< 0.75	0.75 <|y|< 1.50	1.50 <|y|< 2.00
8 - 9 [GeV]	1.13	1.087	1.064
9 - 10 [GeV]	1.219	1.168	1.142
10 - 11 [GeV]	1.253	1.206	1.177
11 - 12 [GeV]	1.268	1.208	1.191
12 - 13 [GeV]	1.25	1.212	1.203
13 - 14 [GeV]	1.238	1.215	1.205
14 - 15 [GeV]	1.233	1.212	1.204
15 - 16 [GeV]	1.223	1.204	1.197
16 - 17 [GeV]	1.209	1.197	1.193
17 - 18 [GeV]	1.201	1.187	1.182
18 - 19 [GeV]	1.192	1.182	1.179
19 - 20 [GeV]	1.183	1.176	1.173
20 - 22 [GeV]	1.174	1.168	1.165
22 - 24 [GeV]	1.162	1.157	1.153
24 - 26 [GeV]	1.15	1.146	1.144
26 - 28 [GeV]	1.14	1.136	1.136
28 - 30 [GeV]	1.131	1.127	1.126
30 - 35 [GeV]	1.119	1.117	1.116
35 - 40 [GeV]	1.103	1.102	1.102
40 - 45 [GeV]	1.091	1.09	1.09
45 - 50 [GeV]	1.082	1.081	1.081
50 - 55 [GeV]	1.074	1.074	1.074
55 - 60 [GeV]	1.067	1.067	1.067
60 - 70 [GeV]	0.859	0.861	0.861
70 - 80 [GeV]	0.925	0.924	0.925
80 - 90 [GeV]	0.975	0.974	0.973
90 - 100 [GeV]	1.011	1.011	1.01
100 - 120 [GeV]	1.034	1.033	1.034
120 - 140 [GeV]	1.03	1.03	1.03
140 - 160 [GeV]	1.026	1.026	1.026
160 - 180 [GeV]	1.023	1.023	1.022
180 - 200 [GeV]	1.02	1.02	1.02
200 - 240 [GeV]	1.018	1.017	1.017
240 - 300 [GeV]	1.014	1.014	1.014
300 - 360 [GeV]	1.012	1.012	1.012

Table D.4: Mean weight correction factor for J/ψ under the "transverse negative" spin-alignement hypothesis.

p_{T}	0.00 <|y|< 0.75	0.75 <|y|< 1.50	1.50 <|y|< 2.00
8 - 9 [GeV]	1.046	1.116	1.152
9 - 10 [GeV]	1.045	1.118	1.144
10 - 11 [GeV]	1.046	1.11	1.123
11 - 12 [GeV]	1.045	1.094	1.108
12 - 13 [GeV]	1.039	1.084	1.101
13 - 14 [GeV]	1.034	1.076	1.088
14 - 15 [GeV]	1.032	1.066	1.08
15 - 16 [GeV]	1.027	1.062	1.072
16 - 17 [GeV]	1.025	1.056	1.066
17 - 18 [GeV]	1.023	1.05	1.058
18 - 19 [GeV]	1.019	1.045	1.054
19 - 20 [GeV]	1.017	1.042	1.049
20 - 22 [GeV]	1.017	1.038	1.043
22 - 24 [GeV]	1.015	1.032	1.036
24 - 26 [GeV]	1.013	1.027	1.031
26 - 28 [GeV]	1.01	1.023	1.029
28 - 30 [GeV]	1.01	1.02	1.024
30 - 35 [GeV]	1.008	1.017	1.019
35 - 40 [GeV]	1.006	1.013	1.014
40 - 45 [GeV]	1.004	1.01	1.012
45 - 50 [GeV]	1.003	1.008	1.009
50 - 55 [GeV]	1.003	1.006	1.008
55 - 60 [GeV]	1.002	1.005	1.006
60 - 70 [GeV]	0.995	0.989	0.986
70 - 80 [GeV]	0.998	0.995	0.994
80 - 90 [GeV]	0.999	0.999	0.998
90 - 100 [GeV]	1	1.001	1.001
100 - 120 [GeV]	1.001	1.002	1.002
120 - 140 [GeV]	1	1.001	1.001
140 - 160 [GeV]	1	1.001	1.001
160 - 180 [GeV]	1	1.001	1.001
180 - 200 [GeV]	1	1	1
200 - 240 [GeV]	1	1	1
240 - 300 [GeV]	1	1	1
300 - 360 [GeV]	1	1	1

Table D.5: Mean weight correction factor for J/ψ under the "off-$(\lambda_\theta - \lambda_\phi)$-plane positive" spin-alignement hypothesis.

p_T	0.00 <|y|< 0.75	0.75 <|y|< 1.50	1.50 <|y|< 2.00
8 - 9 [GeV]	0.944	0.897	0.891
9 - 10 [GeV]	0.946	0.897	0.886
10 - 11 [GeV]	0.955	0.907	0.893
11 - 12 [GeV]	0.962	0.914	0.903
12 - 13 [GeV]	0.964	0.924	0.915
13 - 14 [GeV]	0.969	0.932	0.924
14 - 15 [GeV]	0.973	0.94	0.931
15 - 16 [GeV]	0.976	0.947	0.937
16 - 17 [GeV]	0.977	0.949	0.945
17 - 18 [GeV]	0.978	0.954	0.946
18 - 19 [GeV]	0.979	0.958	0.951
19 - 20 [GeV]	0.982	0.963	0.955
20 - 22 [GeV]	0.984	0.966	0.96
22 - 24 [GeV]	0.987	0.971	0.965
24 - 26 [GeV]	0.988	0.975	0.971
26 - 28 [GeV]	0.989	0.978	0.974
28 - 30 [GeV]	0.991	0.98	0.976
30 - 35 [GeV]	0.993	0.983	0.981
35 - 40 [GeV]	0.994	0.987	0.985
40 - 45 [GeV]	0.995	0.99	0.989
45 - 50 [GeV]	0.996	0.992	0.991
50 - 55 [GeV]	0.997	0.993	0.992
55 - 60 [GeV]	0.997	0.994	0.994
60 - 70 [GeV]	1.006	1.013	1.015
70 - 80 [GeV]	1.003	1.005	1.006
80 - 90 [GeV]	1.001	1.002	1.002
90 - 100 [GeV]	1	0.999	0.999
100 - 120 [GeV]	0.999	0.999	0.998
120 - 140 [GeV]	1	0.999	0.999
140 - 160 [GeV]	1	0.999	0.999
160 - 180 [GeV]	1	0.999	0.999
180 - 200 [GeV]	1	1	0.999
200 - 240 [GeV]	1	1	0.999
240 - 300 [GeV]	1	1	0.999
300 - 360 [GeV]	1	1	0.999

Table D.6: Mean weight correction factor for J/ψ under the "off-$(\lambda_\theta - \lambda_\phi)$-plane negative" spin-alignement hypothesis.

p_T	0.00 <|y|< 0.75	0.75 <|y|< 1.50	1.50 <|y|< 2.00
8 - 9 [GeV]	0.683	0.706	0.706
9 - 10 [GeV]	0.682	0.705	0.716
10 - 11 [GeV]	0.688	0.702	0.704
11 - 12 [GeV]	0.695	0.711	0.706
12 - 13 [GeV]	0.702	0.716	0.718
13 - 14 [GeV]	0.712	0.722	0.727
14 - 15 [GeV]	0.72	0.728	0.732
15 - 16 [GeV]	0.728	0.735	0.739
16 - 17 [GeV]	0.735	0.743	0.745
17 - 18 [GeV]	0.744	0.75	0.751
18 - 19 [GeV]	0.75	0.755	0.758
19 - 20 [GeV]	0.757	0.762	0.764
20 - 22 [GeV]	0.767	0.771	0.772
22 - 24 [GeV]	0.778	0.782	0.784
24 - 26 [GeV]	0.79	0.793	0.794
26 - 28 [GeV]	0.8	0.802	0.803
28 - 30 [GeV]	0.809	0.811	0.812
30 - 35 [GeV]	0.822	0.824	0.825
35 - 40 [GeV]	0.84	0.841	0.841
40 - 45 [GeV]	0.854	0.855	0.856
45 - 50 [GeV]	0.867	0.867	0.867
50 - 55 [GeV]	0.877	0.878	0.878
55 - 60 [GeV]	0.886	0.887	0.887
60 - 70 [GeV]	1.487	1.482	1.481
70 - 80 [GeV]	1.191	1.193	1.192
80 - 90 [GeV]	1.052	1.053	1.055
90 - 100 [GeV]	0.976	0.978	0.979
100 - 120 [GeV]	0.939	0.939	0.939
120 - 140 [GeV]	0.945	0.945	0.945
140 - 160 [GeV]	0.952	0.952	0.952
160 - 180 [GeV]	0.958	0.958	0.958
180 - 200 [GeV]	0.962	0.962	0.961
200 - 240 [GeV]	0.967	0.968	0.968
240 - 300 [GeV]	0.974	0.973	0.973
300 - 360 [GeV]	0.977	0.979	0.978

Table D.7: Mean weight correction factor for $\psi(2S)$ under the "longitudinal" spin-alignement hypothesis.

p_T	0.00 <|y|< 0.75	0.75 <|y|< 1.50	1.50 <|y|< 2.00
8 - 9 [GeV]	1.318	1.273	1.282
9 - 10 [GeV]	1.307	1.268	1.261
10 - 11 [GeV]	1.296	1.263	1.238
11 - 12 [GeV]	1.282	1.254	1.23
12 - 13 [GeV]	1.266	1.246	1.238
13 - 14 [GeV]	1.256	1.241	1.236
14 - 15 [GeV]	1.244	1.229	1.221
15 - 16 [GeV]	1.229	1.218	1.214
16 - 17 [GeV]	1.221	1.212	1.208
17 - 18 [GeV]	1.21	1.203	1.197
18 - 19 [GeV]	1.197	1.191	1.189
19 - 20 [GeV]	1.19	1.186	1.183
20 - 22 [GeV]	1.179	1.176	1.171
22 - 24 [GeV]	1.164	1.161	1.16
24 - 26 [GeV]	1.153	1.149	1.148
26 - 28 [GeV]	1.144	1.14	1.141
28 - 30 [GeV]	1.134	1.133	1.132
30 - 35 [GeV]	1.121	1.12	1.12
35 - 40 [GeV]	1.105	1.104	1.104
40 - 45 [GeV]	1.092	1.092	1.092
45 - 50 [GeV]	1.083	1.083	1.083
50 - 55 [GeV]	1.075	1.075	1.075
55 - 60 [GeV]	1.069	1.068	1.068
60 - 70 [GeV]	0.86	0.86	0.861
70 - 80 [GeV]	0.926	0.925	0.926
80 - 90 [GeV]	0.976	0.976	0.975
90 - 100 [GeV]	1.012	1.011	1.011
100 - 120 [GeV]	1.034	1.034	1.034
120 - 140 [GeV]	1.03	1.03	1.03
140 - 160 [GeV]	1.026	1.026	1.026
160 - 180 [GeV]	1.023	1.023	1.022
180 - 200 [GeV]	1.02	1.02	1.02
200 - 240 [GeV]	1.018	1.017	1.017
240 - 300 [GeV]	1.013	1.015	1.014
300 - 360 [GeV]	1.012	1.011	1.011

Table D.8: Mean weight correction factor for $\psi(2S)$ under the "transverse zero" spin-alignement hypothesis.

p_T	0.00 <|y|< 0.75	0.75 <|y|< 1.50	1.50 <|y|< 2.00
8 - 9 [GeV]	1.665	1.659	1.697
9 - 10 [GeV]	1.449	1.461	1.475
10 - 11 [GeV]	1.373	1.38	1.37
11 - 12 [GeV]	1.332	1.336	1.317
12 - 13 [GeV]	1.302	1.302	1.301
13 - 14 [GeV]	1.286	1.284	1.28
14 - 15 [GeV]	1.267	1.268	1.266
15 - 16 [GeV]	1.248	1.251	1.249
16 - 17 [GeV]	1.234	1.237	1.239
17 - 18 [GeV]	1.222	1.225	1.223
18 - 19 [GeV]	1.21	1.211	1.214
19 - 20 [GeV]	1.202	1.202	1.201
20 - 22 [GeV]	1.187	1.189	1.188
22 - 24 [GeV]	1.172	1.172	1.173
24 - 26 [GeV]	1.159	1.16	1.159
26 - 28 [GeV]	1.148	1.146	1.147
28 - 30 [GeV]	1.137	1.137	1.137
30 - 35 [GeV]	1.124	1.123	1.124
35 - 40 [GeV]	1.107	1.108	1.107
40 - 45 [GeV]	1.094	1.094	1.094
45 - 50 [GeV]	1.084	1.084	1.084
50 - 55 [GeV]	1.076	1.076	1.076
55 - 60 [GeV]	1.069	1.069	1.07
60 - 70 [GeV]	0.86	0.861	0.861
70 - 80 [GeV]	0.928	0.927	0.928
80 - 90 [GeV]	0.978	0.978	0.977
90 - 100 [GeV]	1.014	1.012	1.012
100 - 120 [GeV]	1.034	1.034	1.034
120 - 140 [GeV]	1.03	1.03	1.03
140 - 160 [GeV]	1.026	1.026	1.026
160 - 180 [GeV]	1.023	1.023	1.023
180 - 200 [GeV]	1.02	1.02	1.02
200 - 240 [GeV]	1.018	1.017	1.017
240 - 300 [GeV]	1.014	1.013	1.014
300 - 360 [GeV]	1.011	1.011	1.011

Table D.9: Mean weight correction factor for ψ(2S) under the "transverse positive" spin-alignement hypothesis.

p_T	0.00 <|y|< 0.75	0.75 <|y|< 1.50	1.50 <|y|< 2.00
8 - 9 [GeV]	1.098	1.033	0.995
9 - 10 [GeV]	1.206	1.123	1.096
10 - 11 [GeV]	1.226	1.157	1.121
11 - 12 [GeV]	1.23	1.182	1.148
12 - 13 [GeV]	1.229	1.19	1.181
13 - 14 [GeV]	1.228	1.198	1.19
14 - 15 [GeV]	1.225	1.194	1.183
15 - 16 [GeV]	1.208	1.189	1.179
16 - 17 [GeV]	1.203	1.184	1.177
17 - 18 [GeV]	1.196	1.181	1.173
18 - 19 [GeV]	1.186	1.173	1.169
19 - 20 [GeV]	1.18	1.17	1.164
20 - 22 [GeV]	1.172	1.161	1.159
22 - 24 [GeV]	1.157	1.15	1.149
24 - 26 [GeV]	1.147	1.14	1.139
26 - 28 [GeV]	1.138	1.133	1.132
28 - 30 [GeV]	1.13	1.127	1.125
30 - 35 [GeV]	1.118	1.115	1.114
35 - 40 [GeV]	1.102	1.101	1.099
40 - 45 [GeV]	1.091	1.09	1.089
45 - 50 [GeV]	1.082	1.081	1.081
50 - 55 [GeV]	1.074	1.074	1.073
55 - 60 [GeV]	1.068	1.067	1.067
60 - 70 [GeV]	0.859	0.861	0.861
70 - 80 [GeV]	0.925	0.924	0.925
80 - 90 [GeV]	0.975	0.974	0.973
90 - 100 [GeV]	1.011	1.011	1.01
100 - 120 [GeV]	1.034	1.033	1.034
120 - 140 [GeV]	1.03	1.03	1.03
140 - 160 [GeV]	1.026	1.026	1.026
160 - 180 [GeV]	1.023	1.023	1.022
180 - 200 [GeV]	1.02	1.02	1.02
200 - 240 [GeV]	1.018	1.017	1.017
240 - 300 [GeV]	1.014	1.014	1.014
300 - 360 [GeV]	1.012	1.012	1.012

Table D.10: Mean weight correction factor for ψ(2S) under the "transverse negative" spin-alignement hypothesis.

p_{T}	0.00 <|y|< 0.75	0.75 <|y|< 1.50	1.50 <|y|< 2.00
8 - 9 [GeV]	1.069	1.129	1.15
9 - 10 [GeV]	1.067	1.14	1.165
10 - 11 [GeV]	1.055	1.126	1.135
11 - 12 [GeV]	1.049	1.124	1.116
12 - 13 [GeV]	1.041	1.1	1.114
13 - 14 [GeV]	1.038	1.089	1.104
14 - 15 [GeV]	1.035	1.08	1.091
15 - 16 [GeV]	1.031	1.072	1.084
16 - 17 [GeV]	1.027	1.061	1.074
17 - 18 [GeV]	1.028	1.06	1.067
18 - 19 [GeV]	1.023	1.053	1.064
19 - 20 [GeV]	1.021	1.05	1.056
20 - 22 [GeV]	1.02	1.044	1.051
22 - 24 [GeV]	1.015	1.037	1.044
24 - 26 [GeV]	1.014	1.032	1.036
26 - 28 [GeV]	1.012	1.027	1.033
28 - 30 [GeV]	1.011	1.025	1.028
30 - 35 [GeV]	1.009	1.02	1.024
35 - 40 [GeV]	1.006	1.015	1.017
40 - 45 [GeV]	1.005	1.012	1.014
45 - 50 [GeV]	1.005	1.01	1.011
50 - 55 [GeV]	1.003	1.008	1.009
55 - 60 [GeV]	1.003	1.007	1.008
60 - 70 [GeV]	0.995	0.989	0.986
70 - 80 [GeV]	0.998	0.995	0.994
80 - 90 [GeV]	0.999	0.999	0.998
90 - 100 [GeV]	1	1.001	1.001
100 - 120 [GeV]	1.001	1.002	1.002
120 - 140 [GeV]	1	1.001	1.001
140 - 160 [GeV]	1	1.001	1.001
160 - 180 [GeV]	1	1.001	1.001
180 - 200 [GeV]	1	1	1
200 - 240 [GeV]	1	1	1
240 - 300 [GeV]	1	1	1
300 - 360 [GeV]	1	1	1

Table D.11: Mean weight correction factor for $\psi(2S)$ under the "off-$(\lambda_\theta - \lambda_\phi)$-plane positive" spin-alignement hypothesis.

p_T	0.00 <|y|< 0.75	0.75 <|y|< 1.50	1.50 <|y|< 2.00
8 - 9 [GeV]	0.956	0.89	0.881
9 - 10 [GeV]	0.945	0.891	0.881
10 - 11 [GeV]	0.95	0.898	0.885
11 - 12 [GeV]	0.956	0.907	0.89
12 - 13 [GeV]	0.958	0.916	0.899
13 - 14 [GeV]	0.965	0.926	0.915
14 - 15 [GeV]	0.967	0.93	0.921
15 - 16 [GeV]	0.969	0.937	0.928
16 - 17 [GeV]	0.972	0.943	0.935
17 - 18 [GeV]	0.975	0.949	0.939
18 - 19 [GeV]	0.977	0.951	0.945
19 - 20 [GeV]	0.98	0.957	0.949
20 - 22 [GeV]	0.982	0.962	0.955
22 - 24 [GeV]	0.983	0.966	0.961
24 - 26 [GeV]	0.986	0.97	0.965
26 - 28 [GeV]	0.988	0.974	0.97
28 - 30 [GeV]	0.989	0.977	0.973
30 - 35 [GeV]	0.991	0.981	0.978
35 - 40 [GeV]	0.993	0.985	0.982
40 - 45 [GeV]	0.994	0.988	0.987
45 - 50 [GeV]	0.996	0.99	0.989
50 - 55 [GeV]	0.996	0.992	0.991
55 - 60 [GeV]	0.997	0.993	0.992
60 - 70 [GeV]	1.006	1.013	1.015
70 - 80 [GeV]	1.003	1.005	1.006
80 - 90 [GeV]	1.001	1.002	1.002
90 - 100 [GeV]	1	0.999	0.999
100 - 120 [GeV]	0.999	0.999	0.998
120 - 140 [GeV]	1	0.999	0.999
140 - 160 [GeV]	1	0.999	0.999
160 - 180 [GeV]	1	0.999	0.999
180 - 200 [GeV]	1	1	0.999
200 - 240 [GeV]	1	1	0.999
240 - 300 [GeV]	1	1	0.999
300 - 360 [GeV]	1	1	0.999

Table D.12: Mean weight correction factor for ψ(2S) under the "off-$(\lambda_\theta - \lambda_\phi)$-plane negative" spin-alignement hypothesis.